

INFORMATION TO USERS

This manuscript has been reproduced from the microfilm master. UMI films the text directly from the original or copy submitted. Thus, some thesis and dissertation copies are in typewriter face, while others may be from any type of computer printer.

The quality of this reproduction is dependent upon the quality of the copy submitted. Broken or indistinct print, colored or poor quality illustrations and photographs, print bleedthrough, substandard margins, and improper alignment can adversely affect reproduction.

In the unlikely event that the author did not send UMI a complete manuscript and there are missing pages, these will be noted. Also, if unauthorized copyright material had to be removed, a note will indicate the deletion.

Oversize materials (e.g., maps, drawings, charts) are reproduced by sectioning the original, beginning at the upper left-hand corner and continuing from left to right in equal sections with small overlaps.

Photographs included in the original manuscript have been reproduced xerographically in this copy. Higher quality 6" x 9" black and white photographic prints are available for any photographs or illustrations appearing in this copy for an additional charge. Contact UMI directly to order.

**ProQuest Information and Learning
300 North Zeeb Road, Ann Arbor, MI 48106-1346 USA
800-521-0600**

UMI[®]

University of Alberta

Corrosion Behavior of GaAs

by

Gengsheng Weng



**A thesis submitted to the Faculty of Graduate Studies and Research in partial fulfillment
of the requirements for the degree of *Master of Science***

in

Materials Engineering

Department of Chemical and Materials Engineering

Edmonton, Alberta, Canada

Spring, 2002



**National Library
of Canada**

**Acquisitions and
Bibliographic Services**

**395 Wellington Street
Ottawa ON K1A 0N4
Canada**

**Bibliothèque nationale
du Canada**

**Acquisitions et
services bibliographiques**

**395, rue Wellington
Ottawa ON K1A 0N4
Canada**

Your file Votre référence

Our file Notre référence

The author has granted a non-exclusive licence allowing the National Library of Canada to reproduce, loan, distribute or sell copies of this thesis in microform, paper or electronic formats.

The author retains ownership of the copyright in this thesis. Neither the thesis nor substantial extracts from it may be printed or otherwise reproduced without the author's permission.

L'auteur a accordé une licence non exclusive permettant à la Bibliothèque nationale du Canada de reproduire, prêter, distribuer ou vendre des copies de cette thèse sous la forme de microfiche/film, de reproduction sur papier ou sur format électronique.

L'auteur conserve la propriété du droit d'auteur qui protège cette thèse. Ni la thèse ni des extraits substantiels de celle-ci ne doivent être imprimés ou autrement reproduits sans son autorisation.

0-612-69818-1

University of Alberta

Library Release Form

Name of Author: Gengsheng Weng

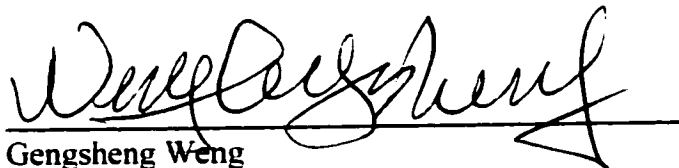
Title of Thesis: Corrosion Behavior of GaAs

Degree: Master of Science

Year this Degree Granted: 2002

Permission is hereby granted to the University of Alberta Library to reproduce single copies of this thesis and to lend or sell such copies for private, scholarly or scientific research purposes only.

The author reserves all other publication and other rights in association with the copyright in the thesis, and except as herein before provided, neither the thesis nor any substantial portion thereof may be printed or otherwise reproduced in any material form whatever without the author's prior written permission.

A handwritten signature in black ink, appearing to read 'Weng Gengsheng', is written over a horizontal line.

Gengsheng Weng

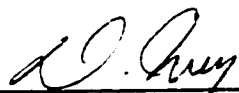
Department of chemical and materials Engineering
University of Alberta
Edmonton, AB, Canada, T6G 2G6

Jan. 31, 2002

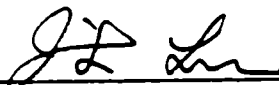
University of Alberta

Faculty of Graduate Studies and Research

The undersigned certify that they have read, and recommend to the Faculty of Graduate Studies and Research for acceptance, a thesis entitled ***Corrosion Behavior of GaAs*** submitted by ***Gengsheng Weng*** in partial fulfillment of the requirements for the degree of ***Master of Science*** in Materials Engineering.



Dr. Douglas Ivey, Supervisor



Dr. Jingli Luo, Co-Supervisor



Dr. Qi Liu, Examining Committee Member



Dr. John-Bruce Green, Examining Committee Member

Date:

Jan. 25/02

ABSTRACT

The corrosion behavior of GaAs in acid solutions and deionized water was studied. The influence of semiconductor type, doping density and illumination was considered. Anodic polarization in acid at lower potentials resulted in an As-rich layer at the surface. The surface As oxidized on subsequent exposure to air leaving As_2O_3 particles on the surface. Polarization at higher potentials resulted in a porous surface. Polarization in water did not remove the surface oxide film; instead, the oxide layer thickened. The galvanic corrosion behavior was examined using the (direct measurement), as well as the method of superposition of polarization curves (indirect measurement). Flat band potentials were also determined by the measurement of the capacity of the electric double layer. Additionally, the corrosion mechanisms were discussed.

ACKNOWLEDGEMENTS

I wish to express my deep gratitude to Dr. D.G. Ivey and Dr. J.L. Luo, for their generous support, encouragement, discussion and suggestions.

I must acknowledge my indebtedness to Ms. C.A. Steer, for her primary work and support.

I am grateful to Dr. Q. Yang, Dr. N. Cui, Dr. Y.F. Chen, Dr. H.Y. Ma, Mr. J.G. Yu and Mr. Y. Huang for their encouragement, discussion and suggestions.

Ms. B. Tina, Mr. J. Chen, Dr. S. Akhlaghi, Mr. M. Shariz and Dr. A.Q. He also deserve my appreciation for providing assistance on samples analysis and preparation.

I would like to express my sincere thanks to Dr. Z. Xu and Dr. D.Y. Li for giving me permission to use their AFM. I received great support from Ms. P.G. Wu, Dr. X.Y. Wang and Mr. H.Z. Ye, who provided AFM analysis.

My thanks are due to Dr. B.T. Lu, Mr. C. Yang and Mr. Y.M. Zen, for their encouragement and discussions.

I am grateful to the Natural Sciences and Engineering Research Council (NSERC) of Canada and Nortel Networks for providing funding. I would also like to thank S. Eicher and D. Clark of Nortel Networks for providing metallized GaAs samples.

My special thanks must be to my parents and my wife for their patience and encouragement, without whom none of this would have been possible.

TABLE OF CONTENTS

CHAPTER 1. INTRODUCTION.....	1
CHAPTER 2. LITERATURE REVIEW.....	4
2.1. INTRODUCTION.....	4
2.1.1. <i>Semiconductors physics</i>	4
2.1.1.1. Energy band	4
2.1.1.2. Doping.....	5
2.1.1.3. Carrier densities and Fermi level	7
2.1.1.4. Generation and recombination of carriers.....	9
2.1.2. <i>Basic principles of corrosion of semiconductors</i>	10
2.2. ELECTROCHEMISTRY OF SEMICONDUCTORS	12
2.2.1. <i>Structure of the electrical double layer</i>	12
2.2.1.1. The Gouy layer	13
2.2.1.2. The Helmholtz double layer.....	14
2.2.1.3. The space charge double layer in the semiconductor	15
2.2.2. <i>Differential capacitance</i>	16
2.2.3. <i>Flat band potential</i>	17
2.3. APPLICATION	19
2.3.1. <i>Photoelectrochemical etching</i>	19
2.3.2. <i>Wet chemical etching</i>	21
2.3.2.1. Anodic etching	22
2.3.2.2. Electroless etching	23
2.3.2.3. Chemical etching	24
2.3.3. <i>The formation of porous GaAs and its properties</i>	24
2.3.4. <i>Oxide layers on III-V compound semiconductors</i>	28

2.4. MEASUREMENT TECHNIQUES	30
2.4.1. <i>Electrochemical methods for corrosion testing</i>	30
2.4.1.1. Polarization techniques for estimating corrosion current of uniform corrosion	31
2.4.1.1.1. Corrosion potential	31
2.4.1.1.2. Polarization resistance	32
2.4.1.2. Electrochemical methods for studying galvanic corrosion.....	33
2.4.2. <i>Measurement of flat band potential</i>	36
 CHAPTER 3. EXPERIMENTAL	46
3.1. ELECTROCHEMICAL TESTS	46
3.1.1. <i>Samples</i>	46
3.1.2. <i>Electrolyte solutions</i>	47
3.1.3. <i>Specimens</i>	47
3.1.4. <i>Potentiostatic polarization</i>	47
3.1.5. <i>Potentiodynamic polarization</i>	48
3.1.6. <i>Impedance</i>	48
3.1.7. <i>Galvanic corrosion</i>	48
3.2. OPTICAL MICROSCOPY	49
3.3. ELECTRON MICROSCOPY	49
3.3.1. <i>Scanning electron microscopy (SEM)</i>	49
3.3.2. <i>Transmission electron microscopy (TEM)</i>	50
3.4. ATOMIC FORCE MICROSCOPY (AFM).....	52
3.5. X-RAY PHOTO ELECTRON SPECTROSCOPY (XPS).....	52
3.6. INDUCTIVELY COUPLED PLASMA (ICP).....	52
3.7. X-RAY DIFFRACTION (XRD)	53
 CHAPTER 4: RESULTS.....	56
4.1. POTENTIODYNAMIC POLARIZATION	56

4.1.1. Polarization curves generated for GaAs in acid	56
4.1.2. Polarization curves generated for GaAs in deionized water	59
4.2. POTENTIOSTATIC POLARIZATION	61
4.2.1. n-type GaAs.....	61
4.2.2. p-type GaAs.....	66
4.3. GALVANIC CORROSION MEASUREMENTS	68
4.3.1. Direct galvanic corrosion measurements	69
4.3.2. Indirect galvanic corrosion measurements	69
4.3.3. Comparison.....	71
4.3.4. Galvanic corrosion rates	72
4.4. IMPEDANCE MEASUREMENTS	75
4.4.1. n-type GaAs.....	77
4.4.2. p-type GaAs.....	77
 CHAPTER 5. DISCUSSION.....	 109
5.1. FORMATION OF ARSENIC OXIDE	109
5.2. LOCALIZED CORROSION	115
5.3. CORROSION IN DEIONIZED WATER	119
5.4. CORROSION MECHANISMS.....	120
5.5. MEASUREMENT OF FLAT BAND POTENTIAL	121
 CHAPTER 6. CONCLUSIONS AND FUTURE WORK	 127
6.1. CONCLUSIONS	127
6.2. FUTURE WORK.....	128
 REFERENCES	 130

LIST OF TABLES

CHAPTER 3.

Table 3.1.	GaAs used in the tests	46
------------	------------------------------	----

CHAPTER 4.

Table 4.1.	Surface morphology of GaAs samples 7 days after polarization.....	62
Table 4.2.	Composition (at%) at surface of n-GaAs polarized in H ₃ PO ₄ analyzed by XPS	64
Table 4.3.	Composition (at%) at surface of n-GaAs polarized in deionized water analyzed by XPS	66
Table 4.4.	Surface Morphology of p-GaAs Samples 7 Days After Polarization.....	67
Table 4.5.	Galvanic corrosion rate in phosphoric acid	74
Table 4.6.	Flat band potentials and surface doping densities for GaAs electrodes	78

CHAPTER 5.

Table 5.1.	XRD results for surface layers at polarized n-GaAs (10 ¹⁸ cm ⁻³)	114
------------	---	-----

LIST OF FIGURES

CHAPTER 2.

Figure 2.1.	Energy-band model of a semiconductor.....	39
Figure 2.2.	Energy-band model of an intrinsic semiconductor.....	39
Figure 2.3.	Energy-band representation of an n-type extrinsic semiconductor	40
Figure 2.4.	Energy-band representation of a p-type extrinsic semiconductor	40
Figure 2.5.	(a) Generation of an electron-hole pair; (b) Direct recombination of an electron and a hole with the emission of a photon; (c) Recombining via a recombination center	41
Figure 2.6.	The scheme for semiconductor corrosion.....	41
Figure 2.7.	Schematic structure of the electric double layer at the semiconductor and electrolyte interface	42
Figure 2.8.	The band bending and charge distribution near the surface of an n-type semiconductor for various values of the potential drop.....	42
Figure 2.9.	The equivalent circuit describing the differential capacity, C , of the electric double layer	43
Figure 2.10.	Equilibrium E-Ph diagram for GaAs-H ₂ O at 25°C.	43
Figure 2.11.	Illustration of three Tafel extrapolation methods of estimating corrosion rate.....	44
Figure 2.12.	Schematic experimental polarization of an anode and cathode in a galvanic couple	45
Figure 2.13.	Equivalent circuits for impedance analysis of semiconductor electrodes. a) A complex equivalent circuit; b) The simplest equivalent circuit	45

CHAPTER 3.

Figure 3.1.	Schematic specimen for the electrochemical tests	54
Figure 3.2.	Schematic three-electrode cell and potentiostat	54
Figure 3.3.	Schematic gold wafer for galvanic corrosion tests	55

CHAPTER 4.

Figure 4.1.	Polarization curves for GaAs in 1% HF (a and c) and 28.5% H ₃ PO ₄ (b and d) under illumination: a) and b) n-GaAs, 10 ¹⁸ cm ⁻³ ; c) and d) p-GaAs, 10 ¹⁸ cm ⁻³	79
Figure 4.2.	Polarization curves for n-type GaAs with various doping densities in 28.5% H ₃ PO ₄ under illumination: a) 10 ¹⁷ cm ⁻³ ; b) 10 ¹⁸ cm ⁻³ ; c) 2x10 ¹⁸ cm ⁻³ and d) 5x10 ¹⁸ cm ⁻³	79
Figure 4.3.	Breakdown potential for n-GaAs as a function of doping density in phosphoric acid under illumination	80
Figure 4.4.	Polarization curves of p-type GaAs with various doping densities in 28.5% H ₃ PO ₄ under illumination: a) 4x10 ¹⁹ cm ⁻³ and b) 10 ¹⁸ cm ⁻³	80
Figure 4.5.	AFM image from n-GaAs (2x10 ¹⁸ cm ⁻³) sample in phosphoric acid	81
Figure 4.6.	Polarization curves for n-GaAs (10 ¹⁷ cm ⁻³) in 28.5% H ₃ PO ₄ in the dark (a) and daylight (b).....	82
Figure 4.7.	Polarization curves for n- (a and b) and p-GaAs (c and d) (10 ¹⁸ cm ⁻³) tested in 28.5% H ₃ PO ₄ under illumination (b and d) and in the dark (a and c).....	82
Figure 4.8.	Polarization curves for n-GaAs (2x10 ¹⁸ cm ⁻³) in 28.5% H ₃ PO ₄ in the dark (a) and daylight (b)	83
Figure 4.9.	Polarization curves for n-GaAs (5x10 ¹⁸ cm ⁻³) in 28.5% H ₃ PO ₄ in the dark (a) and daylight (b)	83
Figure 4.10.	Polarization curves for p-GaAs (4x10 ¹⁹ cm ⁻³) in 28.5% H ₃ PO ₄ in daylight (a) and dark (b)	84

Figure 4.11.	Polarization curves for n-type GaAs with various doping densities in deionized water under illumination: a) 10^{18}cm^{-3} ; b) 10^{17}cm^{-3} ; c) $2 \times 10^{18}\text{cm}^{-3}$ and d) $5 \times 10^{18}\text{cm}^{-3}$84
Figure 4.12.	Polarization curves for p-type GaAs with various doping densities in deionized water under illumination: a) 10^{18}cm^{-3} and b) $4 \times 10^{19}\text{cm}^{-3}$85
Figure 4.13.	Polarization curves for GaAs (10^{18}cm^{-3}) in deionized water under illumination: a) n-type and b) p-type85
Figure 4.14.	Polarization curves for n-type GaAs with various doping densities in deionized water in the dark: a) 10^{18}cm^{-3} ; b) $2 \times 10^{18}\text{cm}^{-3}$ and c) $5 \times 10^{18}\text{cm}^{-3}$86
Figure 4.15.	Polarization curves for p-type GaAs with various doping densities in deionized water in the dark: a) $4 \times 10^{19}\text{cm}^{-3}$ and b) 10^{18}cm^{-3}86
Figure 4.16.	Polarization curves for n- GaAs (10^{18}cm^{-3}) in deionized water in the dark (a) and daylight (b)87
Figure 4.17.	Polarization curves for p- GaAs (10^{18}cm^{-3}) in deionized water in daylight (a) and dark (b).87
Figure 4.18.	SEM micrographs of the surface morphology of n-GaAs. doping $1 \times 10^{17}\text{cm}^{-3}$: (a) immediately; (b) 4 days; (c) 7 days and (d) 17 days after polarization at 0.75 V vs. SCE for 2 hours in 28.5% H_3PO_488
Figure 4.19.	(a) SEM image of the same sample shown in Fig. 4.17d. along with EDX spectra of substrate (b) and one of the particles (c)89
Figure 4.20.	Ga 3d spectra for an as-received specimen (a), immediately after being polarized at 0.75V vs. SCE for 2 hours in 28.5% H_3PO_4 (b) and after exposure to air for one week (c)90
Figure 4.21.	As 3d spectra for an as-received specimen (a), immediately after being polarized at 0.75V vs. SCE for 2 hours in 28.5% H_3PO_4 (b) and after exposure to air for one week (c).91
Figure 4.22.	(a) TEM bright field image from n-GaAs ($2 \times 10^{18}\text{cm}^{-3}$) sample polarized at -0.15V in daylight; (b) EDX spectrum from bulk GaAs (point A) in (a); (c) EDX spectrum from surface region (point B) in (a)92

Figure 4.23.	(a) TEM bright field image from an n-GaAs ($2 \times 10^{18} \text{cm}^{-3}$) sample polarized at 0.4V in daylight; (b) EDX spectrum from bulk GaAs (point A) in (a); (c) EDX spectrum from surface region in (a).....	93
Figure 4.24.	(a) TEM bright field image from an n-GaAs ($2 \times 10^{18} \text{cm}^{-3}$) sample polarized at 0.75V in daylight; (b) EDX spectrum from bulk region in (a); (c) EDX spectrum from surface region in (a).....	94
Figure 4.25.	Ga 3d spectra for an as-received specimen (a), immediately after being polarized at 0.75V vs. SCE for 2 hours in deionized water (b) and after exposure to air for one week (c)	95
Figure 4.26.	As 3d spectra for an as-received specimen (a), immediately after being polarized at 0.75V vs. SCE for 2 hours in deionized water (b) and after exposure to air for one week (c).	96
Figure 4.27.	a) SEM images (a, b) from n-GaAs polarized at 7V for 2 h in phosphoric acid. Also shown is an EDX spectrum (c) from the faceted particle indicated in (b).	97
Figure 4.28.	(a) TEM bright field image from a p-GaAs ($4 \times 10^{19} \text{cm}^{-3}$) sample polarized at 0.15V in daylight; (b) EDX spectrum from bulk GaAs in (a); (c) EDX spectrum from surface layer in (a).....	98
Figure 4.29.	(a) TEM bright field image from a p-GaAs ($4 \times 10^{19} \text{cm}^{-3}$) sample polarized at 0.4V in daylight; (b) EDX spectrum from bulk GaAs in (a); (c) EDX spectrum from surface layer in (a).....	99
Figure 4.30.	TEM bright field image from a p-GaAs ($4 \times 10^{19} \text{cm}^{-3}$) sample polarized at 0.75V in daylight; (b) EDX spectrum from bulk GaAs in (a); (c) EDX spectrum from surface layer in (a).....	100
Figure 4.31.	Galvanic current density vs C/A area ratio for n- and p-GaAs (● n-GaAs, 10^{18}cm^{-3} ; ■ p-GaAs, 10^{18}cm^{-3} and ▲ p-GaAs, $4 \times 10^{19} \text{cm}^{-3}$). All tests were done in daylight.....	101
Figure 4.32.	Superposition of anodic polarization curves for n-GaAs with cathodic polarization curves for Au: a) 10^{18}cm^{-3} , b) $2 \times 10^{18} \text{cm}^{-3}$ and c) $5 \times 10^{18} \text{cm}^{-3}$	101

Figure 4.33.	Superposition of anodic polarization curves for p-GaAs with cathodic polarization curves for Au: a) 10^{18}cm^{-3} and $4 \times 10^{19}\text{cm}^{-3}$102
Figure 4.34.	Comparison of galvanic current densities, obtained directly (●) and indirectly (○) for n-GaAs (10^{18}cm^{-3}).....102
Figure 4.35.	Comparison of galvanic current densities, obtained directly (■) and indirectly (□) for p-GaAs (10^{18}cm^{-3}).....103
Figure 4.36.	Comparison of galvanic current densities, obtained directly (▲) and indirectly (Δ) for p-GaAs ($4 \times 10^{19}\text{cm}^{-3}$)103
Figure 4.37.	Galvanic current densities measure by superposition of cathodic (Au) and anodic (p-GaAs) polarization curves in 28.5% H_3PO_4 : □) 10^{18}cm^{-3} , daylight; ■) 10^{18}cm^{-3} , dark; ○) $4 \times 10^{19}\text{cm}^{-3}$, daylight and ●) $4 \times 10^{19}\text{cm}^{-3}$, dark104
Figure 4.38.	Galvanic current densities measure by superposition of cathodic (Au) and anodic (n-GaAs) polarization curves in 28.5% H_3PO_4 : Δ) 10^{18}cm^{-3} , daylight; ▲) 10^{18}cm^{-3} , dark; □) $2 \times 10^{18}\text{cm}^{-3}$, daylight; ■) $2 \times 10^{18}\text{cm}^{-3}$, dark; ○) $5 \times 10^{18}\text{cm}^{-3}$, daylight and ●) $5 \times 10^{18}\text{cm}^{-3}$, dark104
Figure 4.39.	Mott-Schottky plots for n-GaAs (10^{18}cm^{-3}) in phosphoric acid in the dark (Δ) and daylight (□)105
Figure 4.40.	Mott-Schottky plots for n-GaAs ($2 \times 10^{18}\text{cm}^{-3}$) in phosphoric acid in the dark (Δ) and daylight (□)105
Figure 4.41.	Mott-Schottky plot for n-GaAs (10^{18}cm^{-3}) in deionized water in the dark (Δ) and daylight (□)106
Figure 4.42.	Mott-Schottky plots for n-GaAs ($2 \times 10^{18}\text{cm}^{-3}$) in deionized water in the dark (Δ) and daylight (□)106
Figure 4.43.	Mott-Schottky plots for p-GaAs (10^{18}cm^{-3}) in phosphoric acid in the dark (Δ) and daylight (□)107
Figure 4.44.	Mott-Schottky plots for P-GaAs ($4 \times 10^{19}\text{cm}^{-3}$) in phosphoric acid in the dark (Δ) and daylight (□)107
Figure 4.45.	Mott-Schottky plots for p-GaAs (10^{18}cm^{-3}) in deionized water in the dark (Δ) and daylight (□)108

Figure 4.46.	Mott-Schottky plots for p-GaAs ($4 \times 10^{19} \text{cm}^{-3}$) in deionized water in the dark (Δ) and daylight (\square)	108
--------------	---	-----

CHAPTER 5.

Figure 5.1.	XRD spectrum for n-GaAs (10^{18}cm^{-3}) exposed to air for 100 days after testing at 0.75 V vs. SCE for 5 hours in phosphoric acid in daylight	124
Figure 5.2.	XRD spectrum for n-GaAs (10^{18}cm^{-3}) polarized at 7V vs. SCE for 2 hours in phosphoric acid in the dark	124
Figure 5.3.	Schematic of the surface change for n-GaAs (a-c) and p-GaAs (d-f) polarized at different anodic potentials in phosphoric acid	125
Figure 5.4.	Band diagrams for the semiconductor/electrolyte interface showing potential corrosion mechanisms of n-GaAs	126

NOTATION

Roman Letters

a.c.	Alternating current
A	Ampere
A	Area
C	Capacity
C	Coulomb (unit of charge), $1C=1A/s$
c	Concentration
CB	Conduction band
C_{el}	Space charge capacitance in the electrolyte
C_H	Helmholtz layer capacitance
C_{sc}	Space charge capacitance in the semiconductor
C_{ss}	Surface state capacitance
d.c.	Direct current
d	Thickness
E	Energy; electric field
E_c	Energy of the conduction band edge
E_{corr}	Corrosion potential
E_{couple}	Galvanic couple potential
E_F	Fermi energy
E_g	Energy gap of the semiconductor (E_c-E_v)
E_v	Energy of valence band edge
e^-	Electron (charge)
F	Faraday constant (96484.5 C/Mole)
h^+	Hole
h	Planck's constant (6.626×10^{-34} J·s)
i	Current density
i_{corr}	Corrosion current density

k	Boltzmann constant (86.5×10^{-6} eV/K)
m^*	Effective mass
N	Density (usually density of electronic energy levels)
N_A	Acceptor density
N_C	Effective density of states in the conduction band
N_V	Effective density of states in the valence band
N_D	Donor density
N_{sc}	Density of immobile charge in the semiconductor space charge region
N_s	Density of charges at the surface
n	Density of electrons in the conduction band
n_i	Concentration of carriers in an intrinsic semiconductor
Ox	Oxidant
p	Density of holes in the valence band
Q	Charge, Q/A charge per unit area
R	Resistance
R_{ss}	Surface state resistance
R_u	Uncompensated resistance
Red	Reductant
SC	Semiconductor
T	Absolute temperature ($t + 273.15$) in Kelvin (K)
t	Time; temperature in °C
V	Voltage, potential difference
V	Molar volume, cm^3/mole
V_{fb}	Flat band potential (electrode potential when $V_s=0$)
VB	Valence band

Greek Letters

δ	Phase shift
ϵ	Dielectric constant

ϵ_0	Permittivity of vacuum
ω	Angular frequency
ρ	Density
III, V, etc.	Valency of atom in compound

Subscripts and Superscripts

<i>A</i>	Acceptor
<i>a</i>	Anodic
<i>b</i>	Bulk
<i>c</i>	Cathodic
<i>corr</i>	Corrosion
<i>D</i>	Donor
<i>el</i>	Electrolyte solution
<i>fb</i>	Flat band
<i>H</i>	Helmholtz
<i>n</i>	Electron
<i>p</i>	Hole
<i>sc</i>	Space charge region (of semiconductor)
<i>ss</i>	Surface state

CHAPTER 1

INTRODUCTION

Over the last five decades, semiconductors have come to be used in a wide range of electronic devices, such as transistors, switching devices, voltage regulators, photocells and photodetectors. Because of their unique properties and capabilities, III/V compound semiconductors, such as GaAs, are widely used for optoelectronics and microelectronics, e.g. GaAs transistors in satellite dishes, GaAs transistors in cellular phones and GaAs/AlGaAs laser diodes in CD players.

Wet chemical etching is commonly used for III-V based semiconductors, both for cleaning and etching specific features in wafers [Kelly et al. 1988]. Wet chemical etching is attractive because the materials are generally single crystal and the etch rate depends on crystal orientation. The etch rate can be altered significantly, however, due to galvanic effects. Optoelectronic devices with metallized ridge structures, such as lasers and wave guides, for example, may be susceptible to such galvanic effects [Ivey et al. 1998].

It has been found that wet chemical etching is mainly due to the anodic dissolution, which consumes holes. This can be achieved in three ways: electrochemical oxidation with an external voltage source, electrochemical etching with an oxidizing agent but no external voltage source [Kelly, et al, 1988] and illumination effects.

Illumination plays an important role in the photoelectrochemical etching, which is an electrochemical procedure, intended to improve the surface chemistry or morphology of semiconducting samples for various applications. However, uncontrollable etching results in photocorrosion, an interfacial phenomenon, which is responsible for most of the failures in photoelectrochemical cells for solar energy conversion [Decker et al, 1993].

Further corrosion caused by high current densities can result in localized dissolution of the semiconductor, which has attracted much interest because of its application on light emitting. As an example, anodic etching of GaAs has been performed in HCl solutions at fairly high voltage (6-7 V) to produce porous features for visible light emission applications [Li and Bohn, 2000].

Since GaAs has gained increasing importance in recent years in many applications, corrosion behavior of GaAs has gained considerable interest. The purpose of this work is to study the corrosion behavior of GaAs semiconductor electrodes in acid solutions and deionized water. The influence of the type of semiconductor, doping density and illumination on the electrochemical behavior of GaAs are investigated. Optical microscopy, scanning electron microscopy (SEM), energy dispersive x-ray (EDX) spectroscopy in the SEM, transmission electron microscopy (TEM) equipped with EDX, atomic force microscopy (AFM), photoelectron spectroscopy (XPS) and x-ray diffraction (XRD) are used to characterize the surfaces prior to and after electrochemical tests. Moreover, the effect of the cathode to anode area ratio was investigated with the ultimate goal of forming galvanic cells and predicting the galvanic rate. Two methods were used to determine galvanic corrosion: (1) direct galvanic measurements and (2) superposition of the individual anodic and cathodic polarization curves to indirectly predict galvanic corrosion.

Flat band potential is an important characteristic of the semiconductor/electrolyte system. Its magnitude is used in determining band edges at the interface between

semiconductor and electrolyte. Several methods are available for studying flat band potential, the predominant one being impedance. In this work, flat band potential was determined by the measurement of the capacity of the space charge layer.

Chapter 2 is devoted to the fundamental physical processes involved in semiconducting materials and the essential elements of electrochemical corrosion, as well as comprehensive review of corrosion behavior and application of GaAs. Then follows a short chapter (3) on the sample preparation, the set up of experiments and the methods of surface examination. Chapter 4 provides the results in this work, including polarization curves, surface determinations and analysis. All the results are discussed in Chapter 5. The last chapter concludes the present work and recommends the future work.

CHAPTER 2

LITERATURE REVIEW

2.1. Introduction

2.1.1. Semiconductors physics

2.1.1.1. Energy band

A semiconductor is usually defined rather loosely as a material with an electrical resistivity lying in the range of 10^{-2} - $10^9 \Omega\text{cm}$. Alternatively, it can be defined as a material whose energy gap for electronic excitations lies between zero and about 3 electron volts (eV). Materials with zero bandgap are metals or semimetals, while those with an energy gap larger than 3 eV are more frequently known as insulators [Yu and Cardona, 1999].

The energy band is a significant concept in the theory of semiconductors and is derived from the quantum theory of solids. It is generally used to explain many of the properties of semiconductors. In fact, the explanation of the electrical behavior of semiconductor materials is a great success of quantum theory [Calister, 2000].

A crystal consists of many atoms, which are bonded to form the ordered atomic arrangement. When atoms are close together, the atomic charges cause interatomic forces which bind the atoms together. Since atoms are made up of negative electrons and

positive nuclei, electrons are acted upon or perturbed. Thus an electron energy band is formed by this effect, which may cause each distinct atomic state to split into a series of closely spaced electron states in the solid. The band can be considered as a continuous range of energies, in which the difference between the individual energy levels is very small ($\approx 10^{-8}$ eV). Energy gaps are spacings which exist between energy bands. Within the energy gaps, there are no electron states.

Energy band diagrams in a semiconductor consist of two bands, a conduction band (CB) and a valence band (VB) separated by an energy gap (forbidden gap) (Fig. 2.1). The valence band is the lower band and the conduction band is the upper band. The former one is completely filled with electrons while the conduction band is nearly empty. At temperatures above absolute zero (0K, -273°C) some electrons obtain energy from the surroundings so as to break free from their parent atoms and move through the crystal, that is, to take part in conduction. In terms of the band model this means that some electrons taking part in bonding the atoms together (valence band, VB, electrons) attain energies corresponding to levels in the conduction band, CB. Thus, depending on the degree of excitation, a number of electrons acquire sufficient additional energy to jump the forbidden gap to the conduction band to take part in conduction.

2.1.1.2. Doping

For semiconductors, which are different from metals where free electrons are the only charge carriers, conduction is achieved by electrons and holes. When electrons (charge $-e$) are excited from the VB, some positively charged 'holes' are left in the VB (Fig. 2.2). Some electrons in the valence band may be moved to refill these empty states, hence conduction also takes place in the valence band because of the availability of a few 'holes' [Navon, 1975]. As the excitation of each electron from the VB to CB leaves a hole in the VB, the number of holes in the VB equals the number of electrons in the CB. The process therefore results in the thermal creation of electron-hole pairs [Wang, 1989]. Conduction is therefore via electrons in the CB and holes in the VB. The above has

described intrinsic semiconductors, which are pure semiconductor materials with the same number of electrons and holes.

A semiconductor can also become conductive by doping, impurity atoms are introduced into intrinsic semiconductor. The element introduced is called a dopant and thus an extrinsic semiconductor is formed. For example, if atoms of phosphorus (P) that has five VB electrons/atom are introduced into pure silicon (Si) that has only four VB electrons per atom, the phosphorus atoms take up positions in the crystal structure. Four of the five electrons form bonds with neighboring silicon atoms. The fifth electron from each P atom is surplus to the bonding requirements and being an electron in the outer shell it is only loosely bound to its parent atom. The binding energy of this electron is very small, and so even at low temperature it becomes free and takes part in conduction, increasing the conductivity of the crystal. Because the density of free electrons in P-doped Si is greater than holes, this extrinsic semiconductor is called an n-type semiconductor, and electrons are referred to as majority carriers and holes as minority carriers. Fig. 2.3 shows the energy-band model of an n-type semiconductor. Donor levels, which are just below the CB, represent energy levels introduced by each dopant atom. As the number of electrons supplied by the donor atoms is much greater than that generated from the valence band, the number of thermally generated electrons is negligible. Therefore the density of CB electrons, n_n , can be thought to equal the donor density, N_D :

$$n_n \cong N_D \quad (2.1)$$

If silicon is doped with a group III element that has only three valence electrons, such as gallium or indium, this type of dopant increases the hole density in the crystal without increasing the electron density. Since there is a majority of holes (positive charge), p-type semiconductors are formed. In this case, holes are the majority carriers and electrons are the minority carriers (Fig. 2.4). The number of thermally generated holes is negligible under normal conditions compared to the number from the dopant. The density of VB holes for a semiconductor, p_p , is almost the same as the density of the acceptor-dopant, N_A :

$$p_p \cong N_A \quad (2.2)$$

where p_p is the hole density in the p-type semiconductor.

For III-V semiconductors, such as GaAs, covalent bonding is dominant. When a Group VI element, such as Se is introduced in an As site, it acts as a donor. When a Group II element, such as Zn is introduced on a Ga site, it acts as an acceptor. For a Group IV element, such as Si, it can act both as a donor on a Ga site and an acceptor on an As site.

2.1.1.3. Carrier densities and Fermi level

The concentrations of free carriers, n_n and p_p , are the principal quantities that determine the conductivity of a semiconductor. These quantities depend not only on the concentration of donors N_D and acceptors N_A , but also on the temperature, which determines the degree of thermal excitation of carrier from covalent bonds and impurities.

At absolute zero temperature ($T=0$ K), the occupation probability of an electron state of energy E is given by Fermi-Dirac function

$$f(E) = \frac{1}{1 + \exp(\frac{E - E_F}{kT})} \quad (2.3)$$

Thus, the probability of occupation by a hole is

$$f_h(E) = 1 - f(E) = \frac{1}{1 + \exp(\frac{E_F - E}{kT})} \quad (2.4)$$

where k is the Boltzman constant, E_F is Fermi level, the level of energy in a continuous range that is occupied by an electron for half of the time.

The carrier densities in a non-degenerate semiconductor are given by the Boltzmann approximation of the Fermi-Dirac function [Mayer, 1990]:

$$n = N_C \exp\left(-\frac{E_C - E_F}{kT}\right) \quad (2.5)$$

$$p = N_V \exp\left(-\frac{E_F - E_V}{kT}\right) \quad (2.6)$$

where N_C and N_V are the effective volume densities of electron and hole states in the conduction and valence bands, and the Fermi level in a non-degenerate sample lies between the lowest conduction band energy (E_C) and the highest valence band energy (E_V).

The effective mass is used to define the effective densities of states:

$$N_C, N_V = 2\left(\frac{2\pi m^* kT}{h^2}\right) \quad (2.7)$$

where m^* is the carrier effective mass and h is Planck's constant, 6.626×10^{-34} J.s.

In the intrinsic case, thermal generation across the gap (and recombination to balance it) creates equal numbers of electrons and holes, so that

$$n = p = n_i \quad (2.8a)$$

where n_i is the number of intrinsic charge carriers. Under equilibrium conditions, the relationship between n_i , n and p is given by the following:

$$np = n_i^2 = N_C N_V \exp(-E_g / kT) \quad (2.8b)$$

where E_g is the energy gap ($E_C - E_V$). Eq. (2.8b) is valid for both intrinsic and extrinsic semiconductors. For extrinsic semiconductors, it is clear that $n \gg p$ for n-type material and $p \gg n$ for p-type material.

2.1.1.4. Generation and recombination of carriers

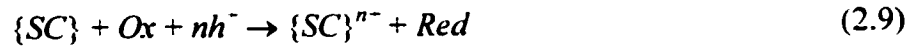
At a fixed level of excitation, electron-hole pairs are continually being created or generated by light energy breaking electrons free from their covalent bonds in the valence band and raising them into the conduction band to take part in conduction through the crystal (Fig. 2.5a). The excitation of VB electrons to CB energy levels leaves holes in the VB that also contribute to conduction. Electron-hole pairs are only produced by light frequency ν such that $h\nu > E_g$. At the same time that free carriers are being generated, the reverse process is taking place for electrons and holes to recombine. Physically, recombination is the process whereby a free electron traveling through the crystal is captured by an atom having an incomplete bonding structure. In the energy band model this can be described by an electron returning to a VB energy level from a CB level with a corresponding loss of energy. This is illustrated in Fig. 2.5b and is generally coupled with the emission of photons with energy equal to that of the semiconductor energy gap.

Practical crystals contain regions of non-uniform structure due to missing or displaced atoms in the lattice and the presence of impurities. In some semiconductors, recombination is generally found to take place via a recombination center introduced by some impurities. These impurities tend to immobilize a hole, which immediately recombines with a conduction electron (Fig. 2.5c) at recombination centers.

2.1.2. Basic principles of corrosion of semiconductors

The spontaneous decomposition (dissolution, oxidation) of a material as a result of physical and chemical interaction with its surrounding medium (in particular, with the electrolyte solution) is called corrosion.

Since there is no current in the outer circuit, the oxidation of the solid must be accompanied by the reduction of other components of the system. For example, simultaneously with the dissolution of semiconductor there may occur the liberation of molecular hydrogen from the solution or the reduction of a dissolved oxidant. The overall equation of the process has the form



where $\{SC\}$ is the semiconductor material, $\{SC\}^{n+}$ is its oxidized form (for example, an ion in solution), Ox is the oxidant, h^+ is a hole, and Red its reduced form.

The dissolution of the semiconductor and the reduction of the oxidant may actually occur in one act so that equation (2.9) reflects the microscopic mechanism of the process. In this case we talk of the chemical mechanism of corrosion or the dissolution of the solid.

However, most often the corrosion has an electrochemical nature. At the solid/liquid interface there are two reactions, anodic and cathodic reactions, proceeding simultaneously and at the same rate:



On samples with a uniform surface the reactions are localized on the same sections of the surface, while in the opposite case the reactions may be separated in space. These reactions are called conjugate reactions. In the electrochemistry of metals they are regarded as completely independent of each other. This means that by changing the external conditions it is possible to change the rate of one of them arbitrarily without affecting the other. Knowing the kinetic parameters of both reactions (the exchange currents and transport coefficients or simply the coefficients a and b of the Tafel relation) we can determine the potential and the corrosion rate from the condition

$$i_a = -i_c = |i_{corr}| \quad (2.12)$$

Where i_a and i_c are the anode and cathode current densities.

A major difference between the corrosion processes on semiconductors and on metals is that the exchange between the solid and the solution proceeds through electrons and holes for semiconductors. Therefore, a condition of the type given in Eq. (2.12) is inadequate. In the dissolution process there must be not only a balance of electric charges, but also a balance of each type of carrier in the semiconductor.

As an example, a simple case is used. In this case, a reaction with the participation of the semiconductor material proceeds through the valence band, while the reaction with the participation of the redox couple from solution occurs through the conduction band (Fig. 2.6a). Although the conjugated reactions occur through different semiconductor bands, the processes of recombination and generation of electrons and holes connect them with each other. However, if the rate of recombination or generation is so small compared with the rates of the conjugated reactions, we can ignore this connection and consider the reactions in Fig. 2.6a as independent.

When the two conjugated reactions occur in the same band, such as the valence band (Fig. 2.6b), a different result can be obtained. In this situation, the cathodic reaction of oxidant reduction occurs by consuming the valence band electrons, which causes holes

to be injected into the semiconductor and are used in the anodic reaction of semiconductor oxidation. Therefore, the kinetics of the anodic reaction on an n-type semiconductor can occur without holes from the bulk; holes can be produced at the semiconductor/electrolyte interface.

2.2. Electrochemistry of Semiconductors

2.2.1. Structure of the electrical double layer

Because of the existence of a Galvanic potential, charged planes or space charge layers are almost always formed at any interface, including the solid/liquid interface. They lead to electrical double layers, consisting of two “plates” containing charges of opposite sign, each “plate” being located in one of the contacting phases [Morrison, 1980]. The charge in the double layer may be concentrated directly on the surface of the phase, that is, in a sheet whose thickness is of the order of atomic dimensions. In the semiconductor, electrons and holes are redistributed resulting from the formation of the diffuse charge near the surface while in the electrolyte there is a redistribution of the ions.

Generally, three double layers at the solid/liquid interface are formed (Fig. 2.7). They are, (1) the Gouy-Chapman double layer in the solution, (2) an intermediate layer called the Helmholtz double layer and (3) the space charge double layer in the semiconductor. These are described in detail in the following sections.

The first one is the space charge region in the solid. In this region the charges are generally uncompensated impurities, trapped holes or electrons, or mobile holes or electrons which are very near the surface. Secondly, there are charged planes on the two sides of the Helmholtz region that form the Helmholtz double layer. One plane is at the solid surface whose charge is in surface states or at the location of adsorbed ions. The other plane is referred as the “outer Helmholtz plane” (ohp), where the charge arises from

ions that drift up to the surface, attracted by the excess charge in or on the semiconductor. Finally, there is an extended region of excess space charge in the Gouy region of the solution, associated with mobile ions. At this region the positive ions are separated from the negative ions.

Other double layers should be considered when a third phase is present, e.g., an oxide covering on a metal or a semiconductor electrode. Charge can be stored (a planar configuration) at “interface states” between the oxide and the substrate, especially if the substrate is a semiconductor; and charge can be stored in the form of space charge in the oxide.

Electrical capacitance in double layers determines the possibility of storing charge in these various space charge regions and Helmholtz planes. Each of the regions around the semiconductor/electrolyte interface is plane of charge separated by distance, and hence each double layer has an associated capacitance with it. The capacitance C for a “parallel plate” capacitor can be written as

$$C = dQ / dV = A\epsilon\epsilon_0 / d \quad (2.13)$$

where dQ is a differential increase in stored charge in the layers, dV the differential voltage change across the double layer, A is the area, ϵ is the dielectric constant, ϵ_0 is permittivity of vacuum, and d is the distance separating the charge being stored.

2.2.1.1. The Gouy layer

The Gouy double layer is a region in the solution near the electrode. A space charge is formed because of an excess of free ions of one sign in this double layer. The charges on the electrode cannot be compensated completely by the ions attracted to the outer Helmholtz plane, so a charged Gouy layer forms resulting from the residual electric field which is directed normal to the surface. Because the Gouy layer is very thin for

concentrated solutions, it can be considered to have melded into the outer Helmholtz plane. That means Gouy layer is dependent on whether the solution is dilute or not. In the study of semiconductors, the Gouy layer usually can be ignored since highly concentrated electrolytes are commonly used.

2.2.1.2. The Helmholtz double layer

The Helmholtz double layer, formed between two planar sheets of charge, is a very important double layer in both semiconductor and metal electrochemistry. The formation of one charged sheet occurs because of ions in solution, particularly at the distance of closest approach (at the outer Helmholtz plane, ohp) attracted by the charged surface. The other one occurs because of charges at the surface of the solid.

In the study of semiconductor, we can ignore other charged layers except the charged surface and outer Helmholtz plane since the charge density (per unit area) is much higher than the charge densities of any other charged layers.

The charge on the planes is in different forms. On the solution side at the ohp the charge is in the form of accumulation. On the solid side of the Helmholtz double layer, the charge is generally considered in three forms: an accumulation of free charge, free charge trapped from the solid onto surface states, or adsorbed ions. The dominant form is dependent on the solid.

If the solid is a semiconductor, it is possible for the Helmholtz potential to be controlled by either adsorption/desorption or electron transfer. There are redox reactions at semiconductor electrodes. In the reactions, electrons transfer from the bulk semiconductor to ions in solution with appropriate energy levels. However, the amount of charge stored in the semiconductor associated with this transfer is not high. There are usually of the order of 10^{16} to 10^{17} electronic charges per square meter or less.

2.2.1.3. The space charge double layer in the semiconductor

The space charge double layer in the semiconductor results from charged regions caused by electron transfer in or out of the semiconductor surface. The space charge can be of several forms such as immobile charged impurities, immobile-trapped carriers near the surface of the semiconductor or mobile electrons or holes in the conduction or valence bands of the semiconductor.

The formation of a space charge leads to electric potential drop close to the semiconductor surface, which causes the potential energy of the electrons to change with distance, i.e., band bending (Fig. 2.8). For n-type semiconductors, if the potential drop at the semiconductor space charge layer $V_{sc} > 0$ the bands are bent downwards. If $V_{sc} < 0$, the bands are bent upwards.

For the special case when $V_{sc} = 0$, the bands run completely horizontal. The potential, V , of the semiconductor electrode (measured against some reference electrode) which corresponds to this special case is referred to as the flat band potential, V_{fb} . At the flat band potential, the potential on the semiconductor surface is equal to the value of the potential in the semiconductor bulk.

The amount of charge in the space charge region of the semiconductor depends on several processes. Because surface states will capture some of the bulk carriers near the surface, a space charge near the surface can be formed in vacuum. When the semiconductor is dipped into a solution, a change in the charge in the space charge region may occur for various reasons:

- (a) the surface states will be influenced by their interaction with the solution, so that the charge in the surface states will change;
- (b) at an open circuit condition, electrons will be injected or extracted from the semiconductor by ions in solution with appropriate energy levels;
- (c) a second electrode is added to the solution and an external voltage, different from the open circuit voltage, is produced between the two electrodes.

The assumption that a voltage is always applied to change the voltage in the semiconductor space charge region — changing it by an amount equal to the change of the imposed external voltage — is one of the key characteristics used in semiconductor electrochemistry. It should be noted that some of the change in voltage can appear across the other double layers in the circuit, so the amount of voltage change across the space charge will not always equal the change in external voltage.

When the bands are bent downwards, electrons tend to move to the surface from the bulk, and holes to the bulk (Fig. 2.8a). When the bands are bent upwards, holes move to the surface and electrons to the bulk (Fig. 2.8b,c). An n-type semiconductor, as a specific example, can be induced when the bands are bent downwards. A depletion layer (Fig. 2.8b) forms if the bands are not bent upwards very much. The surface region is depleted of electrons, yet the number of holes will still be insignificant. In this case the surface region is exhausted of both forms of mobile carriers. An inversion layer (Fig. 2.8c) forms when the bands are significantly bent upwards: the charge created by minority carriers (holes) become dominant. So the n-type semiconductor has actually been “inverted” to p-type at the surface. An accumulation layer forms in a p-type semiconductor when the bands are bent upwards ($V_{sc} < 0$), whilst depletion and inversion layers occur when the bands are bent downwards ($V_{sc} > 0$).

2.2.2. Differential capacitance

The differential capacity, C , of the electric double layer is defined by Eq. (2.13). When a voltage change dV_H is applied across the Helmholtz double layer, we find that

$$C_H = dQ/dV_H \quad (2.14)$$

Similarly, we obtain

$$C_{el} = dQ/dV_{el} \quad (2.15)$$

and

$$C_{sc} = dQ/dV_{sc} \quad (2.16)$$

for the space charge layer in the electrolyte and semiconductor, respectively.

From the above equations, the total capacitance is given as

$$C^{-1} = C_{sc}^{-1} + C_H^{-1} + C_{el}^{-1} \quad (2.17)$$

Thus, the resultant differential capacity of the semiconductor/electrolyte interface is made up of three capacities: C_{sc} , C_H , and C_{el} connected in series (Fig. 2.9).

It should be noted that the calculations made above are based on the assumption that the space charge region of both the semiconductor and the electrolyte are in equilibrium. The potential, which is distributed to the double layers, can be distorted when a current flows across the double layers and the equilibrium is perturbed. However, the influence in the Gouy layer is very small.

2.2.3. Flat band potential

In semiconductor electrochemistry, the flat band potential is one of the most important parameters, because it determines the position of the energy band edges at the semiconductor surface and the charge transfer mechanism, which reveal electrochemical reactivity. The flat band potential can be obtained by capacitance-voltage measurements based on the Mott-Schottky relationship at the semiconductor/electrolyte interface. The technique for the measurements will be discussed later.

For convenience of calculation, when the external potential is employed and varied, it is assumed the potential does not change across the Helmholtz layer, only across the semiconductor space charge layer. For any given semiconductor and electrolyte, when the applied potential is negative compared with the flat band potential,

the electrical potential is lower at the surface than in the bulk for the semiconductor. The energy bands are bent downwards and electrons fall down to the surface with holes moving to the bulk. When the potential is positive with respect to the flat band potential, the energy bands are bent upwards. Electrons fall down to the bulk semiconductor and holes move to the surface. At a potential equal to the flat band potential, there is no potential drop between the surface and the bulk of the semiconductor; the energy band are horizontal and the carrier concentration is the same at the surface as in the bulk.

For n-type semiconductors, the flat band potential is lower than that for p-type semiconductors. This is because flat band potential is a measure of the position of the Fermi level in the flat-band situation. The Fermi level is close to the conduction band for n-type semiconductors and close to the valence band for p-type semiconductors.

For GaAs, the most detailed study was given by La Flere et al [Laflere. et al. 1976, 1980], who investigated the frequency dependence of the impedance on n- and p-GaAs and found that p-GaAs is more frequency dependent than n-GaAs.

The flat band potential is pH dependent and it increases as pH decreases. For the GaAs (100) in buffered KCl electrolyte, the flat band potential change is 15 mV/pH [Rajeshwar and Marz, 1983]. For (111) faces, it is 55 mV/pH [Lafler et al, 1974].

2.3. Application

2.3.1. Photoelectrochemical etching

Single crystalline wafers are usually cut from a larger crystal by means of a diamond saw and then mechanically polished until a mirror-like finish is obtained. Such a procedure destroys the ordered crystal structure near the surface and creates a surface layer that is very damaged and therefore needs to be removed by means of an etching reaction.

Photocorrosion is the interfacial phenomenon that is responsible for most of the failures in photoelectrochemical cells for solar energy conversion. Photoelectrochemical etching, by contrast, is an electrochemical procedure intended to improve the surface chemistry or morphology of semiconducting samples for various applications.

Photoetching is a technique that has been applied for a long time to reveal selective dislocated pits [Uhnerfeld, 1972; Takahashi, 1979] and to generate microstructures on the surface of semiconductors. In fact, photoelectrochemical etching with a holographic set-up was reported in the 1970s [Tyagay et al, 1977]. Since then, this technique has been applied to produce gratings on several compound semiconductors such as GaAs [Podlesnik et al, 1983; Lum et al, 1985] and InP [Matz and Zirrgiebel, 1988; Lulm et al, 1985]. Photoetching with a holographic set-up allows the rapid formation of submicrometer gratings without an intermediate photoresist step and it also allows the growth of the grating to be monitored in situ during the fabrication process. Selective photoetching of III-V compounds, a powerful method for the characterization of these materials, was discovered two decades ago. This method is very useful because, not only can it determine the conductivity type of very small surface areas, but it can also reveal and decorate layers of different diffusion lengths, striations, precipitates and dislocation lines [Hollan et al, 1979]. It now appears that the field of photoelectrochemical etching is rapidly growing and will develop even further with the expanding electro-optical devices based on III-V compound semiconductors.

Photoetching of semiconductors is usually an anodic electrochemical process associated with holes in the valence band: because n-type semiconductors have no such charges, they need to be generated by light. The presence of a hole in a surface bond means that one of the electrons in a bonding orbital has been removed and that the positively charged surface atom can react more easily with the solution.

In anodic corrosion processes with semiconductors, we may consider two cases: the ions from the semiconductor are soluble in the electrolyte; or the ions from the semiconductor are insoluble in the electrolyte, and a new phase can form (generally an oxide). The corrosion reaction occurs, however, only if it is thermodynamically favorable. In order to increase the rate of an etching reaction, the electrode potential can be shifted in the anodic direction. To keep the dissolution reaction going, the corrosion products have to be soluble and must diffuse rapidly into the electrolyte. The rate of the photoanodic dissolution reaction depends in many cases on the pH of the electrolyte, which has been described before, because in the intermediate pH range the oxide films formed during the reaction tend to be more passive. Such etching reactions can also proceed without an anodic current applied externally, when two separate reactions (reduction of the oxidizing agent in the electrolyte and oxidation of the semiconductor atoms) take place simultaneously on the same surface (electroless dissolution).

The influence of light on the rate of the electrochemical process is primarily determined by the change in the surface concentration of current carriers in a semiconductor/electrolyte system. The processes of light-sensitive etching of the semiconductor (both photoanodic and photochemical) can be described as follows:

- (1) light is absorbed in the semiconductor,
- (2) the photogenerated carriers diffuse from the semiconductor bulk to the surface,
- (3) the surface atoms of the semiconductor, and reagents from the solution, react with these carriers.

Although photoelectrochemical etching reactions are usually most effective for n-type semiconductors, many p-type semiconductors cannot be selectively etched. This is

because holes are the majority carriers in p-type semiconductors; the amount does not change significantly with illumination. On the other hand, photogenerated minority carriers, holes in n-type semiconductors, lead to the oxidative decomposition of the lattice. It is possible to photoetch a p-type semiconductor on the basis of an electroless dissolution reaction or a two-step reaction (cathodic photoreduction followed by an anodic dark oxidation of the reduction products). Since the photogeneration of holes is limited to the illuminated regions of the electrode, a spatial resolution of the order of the wavelength of the light can be obtained. Moreover, photoetching proceeds preferentially in the direction of the light beam and deep structures can be produced by this method [Osgood et al, 1982; Carabba et al, 1987].

W. J. Plieth et al [1989] studied the photoetching behavior on (100) n-GaAs and p-GaAs in sulfuric acid. In n-GaAs, a redox system similar to that for others in a certain potential range was observed. The charging and discharging of surface states explained this phenomenon. If the potential is cathodic relative to the surface states, the surface states are charged and serve as electron donors to fill up photoholes generated by electron-hole pair excitation. If the potential is moved anodic relative to the surface states, they become unoccupied and the recombination mechanism is blocked.

Different from n-GaAs, passivation occurs on p-GaAs electrodes. Reduction of the H_2O_2 below the flat band potential was observed under illumination and resulted in the reduction current increasing linearly with the H_2O_2 concentration.

2.3.2. Wet chemical etching

Wet chemical etching plays an important role in various steps of III-V compound semiconductor device fabrication. It is commonly used to obtain samples with perfectly smooth surfaces, to reveal crystallographic imperfections, sample regions and layers with different doping density, or to define and separate accurately active regions from the bulk of an integrated electronic device. Different from photoelectrochemical etching, in which

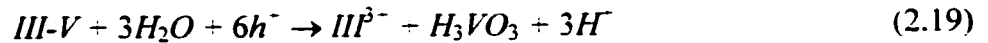
illumination does play a great role, wet chemical etching applies external power or an oxidizing agent.

2.3.2.1. Anodic etching

Anodic etching of a III-V semiconductor is oxidation of the semiconductor in an electrolyte to form a circuit with an external direct-voltage power source [Kelly et al. 1988]. In the circuit, the semiconductor is connected to the positive terminal and an inert counter-electrode is connected to the negative terminal. When the potential of the anode is positive and high enough, a current forms, and the surface of the semiconductor is oxidized. The ions formed in this process dissolve. For this process, electrons are moving toward the positive terminal of the power supply, leaving holes in the valence band to take part in the dissolution. Generally, the overall anodic corrosion of III-V semiconductors requires six holes (h^+) per formula unit and can be written in the form:



The nature of the reaction products is determined by the value of pH and composition of the electrolyte. The dissolution of III-V semiconductor in acid solutions is typically given by:



Since the oxidation process is due to consumption of holes at the surface, semiconductors need to have a sufficient number of holes in the valence band. This will be the case for the highly doped p-type semiconductors because there are large numbers of holes in their valence bands.

Undoped or n-doped semiconductors cannot be etched except in light. This is because holes are minority carriers and there are few holes in the valence band. Under

illumination, electrons, absorb sufficient energy from photons, are excited from the valence band into the conduction band, leaving holes in the valence band. Thus, at appropriate band bending, holes can move to the surface of semiconductor and anodic dissolution occurs.

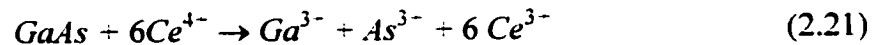
Anodic etching is not a convenient method for semiconductor technology because it requires an external power supply and a counter-electrode, with various electrical contacts. Electrical contact to a semiconductor material during the fabrication process is also required, although anodic etching achieves success in some ways.

2.3.2.2. Electroless etching

Different from anodic etching, electroless etching is one method of wet chemical etching where the etchant contains an oxidizing agent but no external power source. The oxidizing agent annihilates electrons in valence band and thus in fact supplies holes to the valence band. For GaAs, Ce^{4+} is a suitable oxidizing agent:



where the total reaction can be written as:



The above process cannot be developed unless the equilibrium potential of the redox couple (in this case Ce^{4+}/Ce^{3+}), is higher than the potential of the solid (GaAs) in equilibrium with its ions (Ga^{3+} , As^{3+}) in the solution. The location of the energy bands of the semiconductor in relation to the energy levels of the redox couple in the solution determines the reaction rate.

Since the transfer of electrons from the valence band to the oxidizing agent in the solution determines electroless etching, both p-type and n-type semiconductors can be dissolved with the same etchants.

2.3.2.3. Chemical etching

As with electroless etching, there is no application of an external potential in chemical etching. The difference relative to electroless etching is that there are no free charge carriers involved in chemical etching. Chemical etching is caused by the surface of the semiconductor being attacked through the action of reactive molecules (e.g., HCl). This action breaks the bonds between the surface atoms and creates new bonds with the atoms of the reactive molecules. The newly formed compound can be dissolved in the etchant or escape as gases.

2.3.3. The formation of porous GaAs and its properties

The concepts of wet etching of semiconductor include both isotropic and anisotropic etching. Isotropic etching is independent of the direction of crystallographic direction, whereas anisotropic etching depends on the crystallographic direction. An extreme case of anisotropic etching is the formation of porous layers.

In general, porous structures can be formed if the etch rate is dependent on the crystallographic orientation, the transport of reactants (and/or products) is not rate limiting, and the etching process does not lead to the formation of a passivation layer whose dissolution is rate limiting. These considerations illustrate that controlled anisotropic etching can be obtained in semiconductors. It was found that a porous layer was formed with tunnels of diameters ranging from 0.5 μm to 5 μm and a pore areal density of about 10^8cm^{-2} during the electrochemical etching of n-type GaAs in the dark in

KOH and H₂SO₄ solutions. The tunnels propagate only in the <111> direction from gallium to arsenic [Holt, 1988].

In order to determine the relation between the fabrication parameters and the resulting structure of the porous layers, the electrochemical aspects of the pore formation process were studied. During the initial stages of pore formation many nuclei may be created at the surface although only some of them will propagate. The selection process is controlled by the screening effect caused by the characteristic pore spacing, which is related to the depletion layer width [Searson et al, 1992]. Once the pores depth reaches several pore spacing lengths, the selection process is complete and stable pores begin to propagate. The propagation is determined by the etching process itself and not by transport of products or reactants in the pores. Under these conditions, a constant pore size and pore front velocity, and hence pore density and porosity result from stable pore propagation [Oskam et al, 1997].

Although, the mechanism of pore formation in semiconductors has not yet been understood completely, pore propagation in n-type GaAs in the dark is considered to be due to holes in the valence band generated through a breakdown mechanism.

It has been mentioned before that the electrochemical etching of GaAs requires six charges to dissolve one molecule. The dissolution reaction is complicated with various intermediates of different electronic structure and electrical properties. Etching usually proceeds through trapping of valence band holes in surface bonds. Although the equilibrium density of holes in n-type GaAs in the dark is very low, significant etching can occur at relatively high voltages where a number of holes can be generated by a breakdown mechanism. The mechanism of the etching reaction is complicated since local electric fields may vary on different parts of the surface.

The potential required for etching is a function of the donor density; the higher the donor density, the lower the potential. From the measured potentials and the measured flat band potentials, the band bending during pore formation can be estimated.

The rate of hole generation is determined by the field at the surface and is spatially dependent because the three dimensional structure of the porous layer is complex. Due to the small radius of the pore tip, the electric field at the tip can be larger than that at the pore walls [Searson et al, 1992]. As a consequence, the generation rate of holes at the pore tip is higher than at the pore walls. The depletion layer provides a screening effect so that the field at the pore walls becomes even smaller than that at the tips.

Since the rate of hole capture (etching) is generally much slower than the generation rate, the holes at the pore tip can be considered to be in quasi-equilibrium with the bulk. In this case, as the donor density increases, the field at the surface also increases thereby confining the holes closer to the surface. In addition, the hole diffusion length is expected to decrease with increasing donor density [Soltz and Cescato, 1996]; the combination of these two effects will lead to localization of the holes closer to the pore tip and decrease pore size.

Since the majority of the holes are generated at the pore tips, the holes have to diffuse along the perimeter of the pores over relatively long distances in order to attain equilibrium. At locations on the microscopic surface where the concentration of weakly bonded sites is large, the hole capture probability is larger which leads to a decrease in the surface diffusion length of free holes. As the porous layer becomes thicker, depletion of holes at the pore walls stops pore widening. Thus the pore diameter is constant over the thickness of the porous layer.

The electrochemical etch rate of semiconductors is often limited by the first hole captured at a surface site and this initial step is expected to occur preferentially at weakly coordinated sites. Subsequent reaction steps are expected to be faster than the first step and they should have no influence on the resultant pore structure. Consequently, the etch rate will be larger at the pore tips where the concentration of weakly coordinated surface sites and the density of holes is expected to be higher, which leads to a highly directional etching process resulting in pore propagation.

It was reported that pit growth could be electrochemically initiated on both conduction types in chloride-containing solutions and leads to the formation of a porous GaAs structure over a long time [Schmuki et al, 1996]. Exposure of the sample for longer times above the pitting potential leads to complete conversion of the surface to a porous structure. Preferential attack occurs perpendicular to the $[100]$ direction, i.e. along $\langle 011 \rangle$ directions. This is in agreement with work on photoelectrochemical etching of n-InP (100), which also shows preferential etching along the $\langle 011 \rangle$ axis. Different reactivity of the different planes is the most likely reason for the preferential attack leading to the formation of the porous structure.

In acidic aqueous solutions, an arsenic layer forms upon the gallium arsenide electrode surface within the porous features and the composition and morphology change with time [Finnie and Bohn, 1999; Lingier and Gomes, 1991].

Optical properties of porous GaAs formed electrochemically on n- and p-type GaAs in HCl electrolyte were reported [Lockwood et al, 1999]. The porous regions were comprised of GaAs crystallites from microns to nanometers in size and under certain chemical condition other transparent crystallites of As_2O_3 and Ga_2O_3 form. It was found in this work that porous GaAs formed electrochemically in HCl solution, and exhibited both a green and an infrared photoluminescence. The size distribution of the porous material was related to the intensities and the positions of the two photoluminescence peaks.

Porous GaAs can be electrochemically formed on predefined surface areas. Before the electrochemical experiment, focused ion beam implantation was used to sensitize the areas [Schmuki et al, 1999]. Visible photoluminescence was seen from these locally confined sites of GaAs. The effect of focused ion beam implantation of Si^{2+} into GaAs was to create initiation sites, which led to pore formation at anodic potentials below the pore formation potential of an intact GaAs surface. Implantation of Si in GaAs led to the creation of defects and an increased donor concentration in the substrate. Both effects shifted the breakdown potential to lower anodic values.

In HF solutions, the uniformity of the porous layer was observed to decrease with decreasing doping density. The layers formed in n-GaAs ($4 \times 10^{18} \text{cm}^{-3}$) samples were uniform both laterally and in thickness. The porous layers in the n-GaAs ($4 \times 10^{17} \text{cm}^{-3}$) samples were relatively uniform although their thickness fluctuated by as much as 20% on different parts of the wafer. Porous layers formed in n-GaAs ($2 \times 10^{16} \text{cm}^{-3}$) were characterized by a rectangular surface where pores were initiated, while other parts of the surface remained unetched [Oskam et al, 1997].

2.3.4. Oxide layers on III-V compound semiconductors

Oxide formation, during anodic etching of semiconductors, has been widely studied in order to understand and improve the ability to passivate the surface. In addition, oxide insulating properties are utilized in the fabrication of electronic devices. The need for the unique electrical and optical properties of III-V compound semiconductors has led to a search for a compatible insulator for these semiconducting materials [Wilmsen, 1976; Wilmsen and Kee, 1978; Spricer et al, 1979; Sixt et al. 1979; Weimann, 1979; Landgren et al. 1984; Lenczycki and Burrows, 1990; Besland et al. 1993; Hechner et al, 1995; Schmuki et al. 1996; Finnie and Bohn, 1999; Finnie et al. 1999; Li and Bohn, 2000].

When a fresh surface of a III-V semiconductor is exposed to an oxidizing atmosphere, both III-O and V-O oxides are formed locally after initial chemisorption and nucleation. Usually one of the elements has a higher oxidation rate than the other element. The oxides grow outward and laterally along the surface. This leads to an initial oxide which has an outer layer and an inner layer.

The bulk thermal oxide of GaAs is almost entirely Ga_2O_3 with free As at the oxide/GaAs interface. The anodic oxide/GaAs interface is not as well understood as that of the thermal oxide. In order to explain the formation of the interfaces, the initial growth

morphology of thermal and anodic oxides of GaAs and proposed models were investigated [Wilmsen et al, 1979].

Thermal oxides are primarily Ga_2O_3 with As-O bonding appearing only at the outer surface. Excess As at the oxide/GaAs interface has been observed to increase progressively as the oxide thickens. The anodic oxide shows that there is an inner layer of Ga_2O_3 and the thickness is constant. The outer oxide layer is composed of a mixture of Ga_2O_3 and As_2O_3 . The thickness of this mixed layer increases with total oxide thickness.

Thin anodic oxides on p-GaAs grown in aqueous solutions of $\text{NH}_4\text{H}_2\text{PO}_4$ and borate buffer has been reported [Besland et al, 1993]. The electrolyte composition has a strong influence on the oxide growth-determining step and the composition of the oxide. In $\text{NH}_4\text{H}_2\text{PO}_4$, due to the formation of a Ga-phosphate precursor layer, films grow under field control. The oxide thickness is dependent on the time and the composition through the depth is fairly uniform with a significant enrichment of Ga_2O_3 . In borate buffer, oxide growth results in a two-layer structure with an outer As_2O_3 rich layer and ion transfer is mainly diffusion controlled.

The quality of the oxide films in terms of their charge and ion-transfer resistance is related to the composition. The Ga-rich films formed in $\text{NH}_4\text{H}_2\text{PO}_4$ show significantly lower steady state currents and a much higher specific charge transfer resistance than films grown in borate buffer.

Results from studying the gallium arsenide surface during oxidation in 0.05 N methanolic potassium hydroxide show that both anodic and chemically grown native oxides on GaAs are not simple mixtures of Ga_2O_3 and As_2O_3 . The oxides appear to be built up of AsO_3 and GaO_4 units containing both bridging and terminal oxygen atoms [Lenczycki and Burrows, 1990].

In concentrated HCl, many anodic As_2O_3 microcrystals are produced on the GaAs substrate [Schmuki et al, 1996]. The crystals are oriented randomly, with no preferred

relationship to the GaAs substrate. It was pointed out that HCl facilitates As_2O_3 growth, which is sustained by the fact that As_2O_3 microcrystals are much more abundant and larger in size when produced at higher HCl concentration. This is consistent with the fact that the solubility of As_2O_3 decreases and that of Ga_2O_3 increases at lower pH [Greenwood and Earnshaw, 1997].

Tromans et al [1993] calculated the GaAs- H_2O equilibrium diagram (Fig. 2.10), predicted the polarization behavior of GaAs, indicating GaAs is stable only in region *A* and oxides of both Ga and As are stable only in a small region *B*.

2.4. Measurement techniques

2.4.1. Electrochemical methods for corrosion testing

Electrochemical methods are extremely useful in the study of aqueous corrosion phenomena, particularly when utilized in conjunction with other techniques. Electrochemical processes require anodes and cathodes in electrical contact and an ionic conduction path through an electrolyte. The electrochemical process includes electron flow between the anodic and cathodic areas, to quantify the rates of the oxidation and reduction reactions that occur at the surfaces. Monitoring this electron flow provides the capability of assessing the kinetics of the corrosion process [Baboian and Dean, 1990].

2.4.1.1. Polarization techniques for estimating corrosion current of uniform corrosion

2.4.1.1.1. Corrosion potential

The cathodic and anodic reaction rates usually both follow Tafel behavior

$$V = a + b \log i \quad (2.22)$$

where V is the electrode potential of the specimen, i is the current density of the electrochemical reaction, and a and b are constants.

The a constant is related to the physics of specimen. b in this equation is often referred to as the Tafel slope and is usually expressed in mV per decade. The corrosion current can be estimated if the electrochemical corrosion processes follow this Tafel behavior. The measured current density on the specimen is related to the current densities of the electrochemical reactions occurring on the specimen surface by the following equation:

$$i_{\text{measured}} = i_{\text{anode}} - i_{\text{cathode}} \quad (2.23)$$

The exponential behavior of current density with potential means that the anodic contribution to the net current density can generally be ignored if the specimen potential is 50 mV negative than the open circuit value, while the cathodic contribution is usually negligible at potentials 50 mV more positive than the open circuit value.

Three different techniques can be used to estimate corrosion currents. The specimen can be polarized to potentials at least 50 mV more negative than the open circuit corrosion potential, and then sufficient data points are recorded to obtain a reliable Tafel line. A semi logarithmic plot is used to extrapolate the current density data back to corrosion potential. From this, the corrosion current density value can be obtained. The second technique is almost the same as the first one except the specimen is polarized anodically to potentials greater than 50 mV more positive than the corrosion potential. The third technique requires that both cathodic and anodic polarizations be carried out as described above, and the corrosion current is obtained at the intersection of the anodic and cathodic extrapolated lines [Dean, 1976]. These techniques are illustrated in Fig. 2.11.

2.4.1.1.2. Polarization resistance

Polarization resistance is essentially the reciprocal of the linear slope of the polarization curves close to the corrosion potential. Stern developed this 'linear polarization' method, that corrosion is frequently controlled by activation overpotential.

A small potential difference is applied to the specimen and the current this type of change produces is measured. The potential-current density plot is approximately linear in the region within 10 mV of the corrosion potential. The slope of this plot in terms of potential divided by current density has the units of resistance times area and is often called the polarization resistance. This polarization resistance is related to the corrosion current density by the relationship

$$\frac{i_{measured}}{E} = \frac{1}{R_p} = 2.3i_{corr} \left(\frac{b_a + b_c}{b_a b_c} \right) \quad (2.24)$$

where $i_{measured}/E$ is the change in specimen current density per unit change in potential, i_{corr} is the corrosion current density, R_p is the polarization resistance (Ωm^2), and b_a and b_c are the magnitudes of the Tafel slopes of the anodic and cathodic Tafel lines, respectively.

In order to use this technique, it is of course necessary to know the Tafel slopes independently. However, in many cases, reasonable estimates can be made as to what these Tafel slopes should be.

This method is very attractive in many applications because it allows the corrosion rate to be measured directly and instantaneously by relatively simple electronic instruments. However, there are problems with the method. The corrosion rate determined is only an average, and the method does not indicate pitting or other forms of localized attack. The assumption that the potential versus current density plot is linear within the 10mV range is also a source of error. In cases where the anodic and cathodic Tafel slopes are substantially different, errors from the linearity assumption can be significant.

2.4.1.2. Electrochemical methods for studying galvanic corrosion

Galvanic corrosion can be explained by mixed-potential theory. In the case where two or more materials are electrically in contact, there is in theory a minimum of two cathodic and two anodic reactions. One of each of these reactions is occurring on each material. In this case, the more noble of the two materials is cathodically polarized and its anodic reaction rate will thus be suppressed. Conversely, the less noble or anodic material is anodically polarized and the anodic reaction rate is accelerated. In other words, one of them is preferentially corroded while the other is protected from corrosion. The mixed potential (the galvanic couple potential, E_{couple}) of the galvanic couple and the resulting galvanic current can be uniquely determined from the sums of all of the individual anodic

and cathodic currents. In this case, the sum of total anodic currents equals the sum of total cathodic currents, so we have:

$$\sum i_a \times A_a = \sum i_c \times A_c \quad (2.25)$$

where $\sum i_a \times A_a$ is the sum of the anodic currents, and $\sum i_c \times A_c$ the sum of the cathodic currents for all the materials coupled.

It should be noted that the area ratios of the anode and cathode play important role in the galvanic corrosion. Since the corrosion current is mainly dependent on anodic current, i_a , according to Eq. 2.25, the ratio of A_a/A_c must increase in order to decrease i_a .

Many authors have reported on the galvanic corrosion behavior of metals and alloys. From their results, the mechanisms and driving force for corrosion were discussed. Some papers used the anodic and cathodic polarization behavior of the alloys to predict galvanic corrosion [Mansfeld and Kenkel, 1975; Rebul, 1979; Jones, 1984; Scully and Hack, 1984; Davis et al, 1986]. However, few papers have been published considering the problems associated with semiconductors. Actually, galvanic corrosion can occur in semiconductor technology. This can happen with metallized semiconductors while being polished and cleaned in an acid solution or deionized water [Ivey et al, 1998], or with the semiconductor p/n structures during etching processes in electroless and chemical etchants [Ven and Kelly, 2001]. In the former case, voids in the metallization layer, can lead to seepage of the acid into the voids to form a galvanic corrosion environment. As an example, optoelectronic devices with metallized ridge structures have been found to be susceptible to galvanic corrosion [Gerischer, 1977]. For InP-based laser structures, a Ti/Pt/Au ohmic contact on a p-type InGaAs capping layer is generally used. The topography associated with the ridge structure can result in the uneven coverage of the metal, which could lead to the formation of breaks or gaps in the

metallization layer. Therefore, some small exposed regions of InGaAs can form. When the ridge is cleaned in an acid solution, galvanic corrosion occurs between the metallization layer and exposed InGaAs. The outer metal (Au) acts as a cathode, and the InGaAs as an anode. The larger area ratio of metal to semiconductor causes a high corrosion current density, resulting in quick dissolution of InGaAs. In the latter case, a galvanic cell forms between p/n junctions when n- and p-type semiconductors are in contact with the solution. The cell can be controlled for etching p/n junctions.

Electrochemical techniques for predicting galvanic corrosion are based on two types of measurements. They are polarization and galvanic current measurements.

When two different corroding materials are coupled electrically in the same electrolyte, both materials are polarized so that each corrodes at a new rate. The solid lines in Fig. 2.12 show schematic experimental polarization curves in a galvanic couple. The polarization curves for the half-cell reactions are shown by the dashed lines [Jones, 1996]. The corrosion potentials and corrosion currents are $E_{corr,A}$, $I_{corr,A}$ and $E_{corr,C}$, $I_{corr,C}$ for the anode and cathode, respectively. The couple potential, E_{couple} , is established where the anode and cathode are polarized to equal potentials by the same current, I_{couple} , the galvanic corrosion current.

A zero resistance ammeter (ZRA) is generally used to measure galvanic currents between galvanically coupled materials. This technique is based on the fact that anode and cathode potentials are equal in a shorted galvanic couple with no intermediate instrumentation. Therefore, I_{couple} is the current in a shorted galvanic couple.

2.4.2. Measurement of flat band potential

The flat band potential is an important parameter in the study of the semiconductor/electrolyte system. If the flat band potential, V_{fb} , is known, one can determine the position of the band edges on the electrochemical scale and the direction and magnitude of the band bending [Finklea, 1988].

Several methods have been applied for determining the flatband potential and one of the most common methods is the measurement of the differential capacity of the electric double layer.

This method is based on the validity of the Mott-Schottky relationship for the semiconductor/electrolyte barrier [Cardon and Gomes, 1978]. In the case of an n-type semiconductor, we can obtain the relationship between the differential capacity, C_{sc} , and the potential drop in the semiconductor, V_{sc} :

$$C_{sc}^{-2} = 2/\epsilon\epsilon_0eN(|V_{sc}| - kT/e) \quad (2.26)$$

where ϵ is the dielectric constant of the semiconductor, ϵ_0 is permittivity of vacuum, N is the density of donor states, and $V_{sc} = V - V_{fb}$, with V being the applied potential. C_{sc}^{-2} is plotted vs. V ; a straight line should be obtained and the flat band potential is determined by extrapolation of the plot to $C_{sc}^{-2} = 0$.

C_{sc} can be measured by a number of impedance techniques. An a.c. voltammetry is very popular because of the advent of modern instrumentation (potentiostats and lock-in analyzers). An a.c. potential, which has small amplitude (10mV peak-to-peak), with a fixed frequency is added to a d.c. potential, and the combined potential is applied to the semiconductor electrode. A phase shift occurs between a.c. current and a.c. voltage. The phase shift and the impedance are measured as a function of frequency. The impedance decreases with increasing frequency and the phase shift changes with frequency. It has been observed that above a certain frequency the phase shift is almost equal to zero

[Memming, 1964]. At high frequency the phase shift is proportional to the reciprocal frequency:

$$\tan \delta = -\frac{1}{\omega RC} \quad (2.27)$$

where δ is donated as the phase shift, ω is the angular frequency, R is the ohmic resistance and C is the capacitance.

The above indicates that in the low-frequency range, the equivalent circuit for the double layer is rather complicated, but in the high-frequency range, a very simple equivalent circuit can be used.

As shown in Fig. 2.13a, the space charge capacity C_{sc} , the Helmholtz capacity C_H , and an uncompensated resistance R_u (representing the bulk resistances of the electrolyte and the semiconductor) are connected in series. When a d.c. voltage is employed, a current thus flows across the interface. The space charge and Helmholtz capacities are shunted by a faradaic resistance R_f and an surface impedance $(R_{ss} + R_{ss} + C_{ss} + C_{ss})$, which is also dependent on the frequency. At higher frequency, the resistance of impedance and faradaic resistance are much higher than the parallel space charge and Helmholtz capacities, so the former two resistances can be neglected. Furthermore, the Helmholtz capacity C_H is large compared to the space charge capacity C_{sc} , so C_H also can be neglected. In this way, the equivalent circuit is reduced to space charge capacity C_{sc} and uncompensated resistance R_u connected in series, which is the simplest equivalent circuit (Fig. 2.13b).

In fact, there must be some assumptions made for Eq. 2.26 to be applied to calculate flat band potential. Firstly, space charge capacity determines the measured capacity of the electrode and electrolyte. Secondly, the potential drop only occurs in the semiconductor; in the Helmholtz layer the drop is constant. Thus

$$C_{sc} \ll C_H \quad |\Delta V_{sc}| \gg |\Delta V_H| \quad (2.28)$$

The Mott-Schottky plot should remain linear as long as the space charge layer is a depletion layer. When an inversion layer forms, a downward deviation from linearity occurs.

The great advantage of the Mott-Schottky method is that flat band potential can be measured in the absence of light. This is important when photo-generated minority carriers can change the chemical nature of the surface via photo-corrosion reactions.

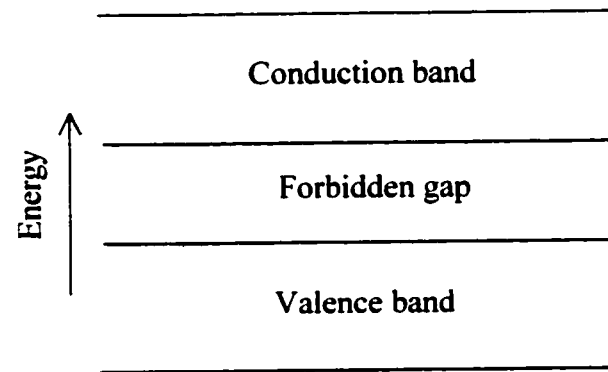


Figure 2.1. Energy-band model of a semiconductor.

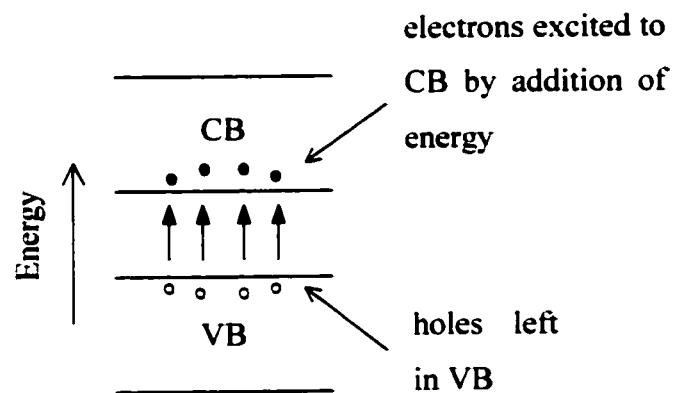


Figure 2.2. Energy-band model of an intrinsic semiconductor [Goodge, 1983].

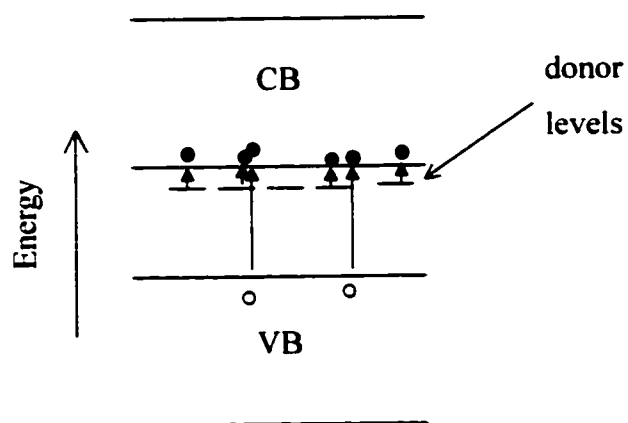


Figure 2.3. Energy-band representation of an n-type extrinsic semiconductor [Goodge, 1983].

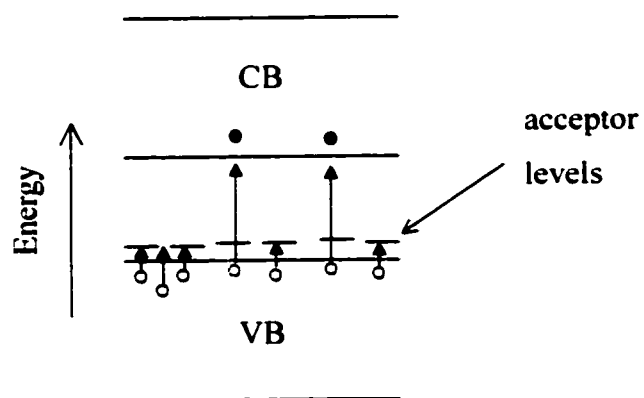


Figure 2.4. Energy-band representation of a p-type extrinsic semiconductor [Goodge, 1983].

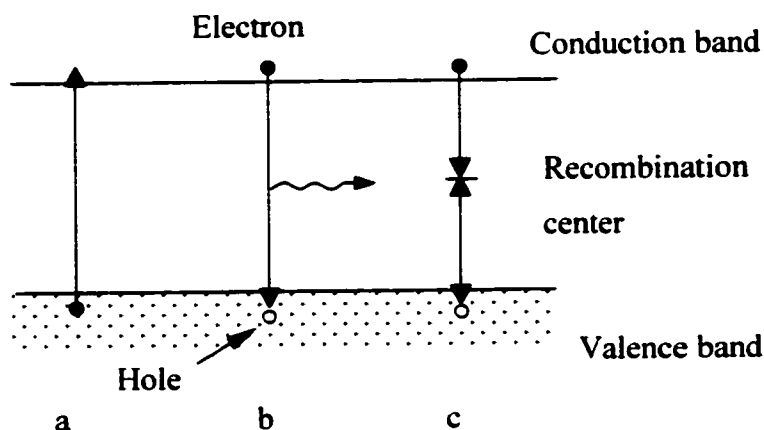


Figure 2.5. (a) Generation of an electron-hole pair; (b) Direct recombination of an electron and a hole with the emission of a photon; (c) Recombining via a recombination center [Navon, 1975].

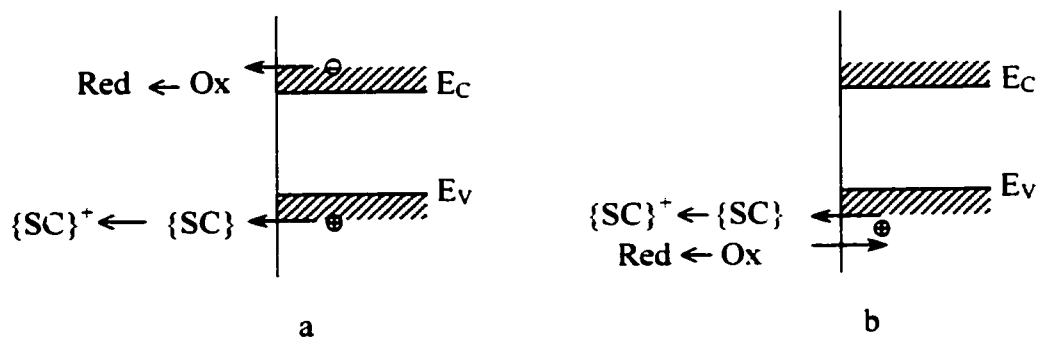


Figure 2.6. The scheme for semiconductor corrosion: a) via different bands; b) via one band (recombination/generation processes are not shown) [Pleskov and Gurevich, 1986].

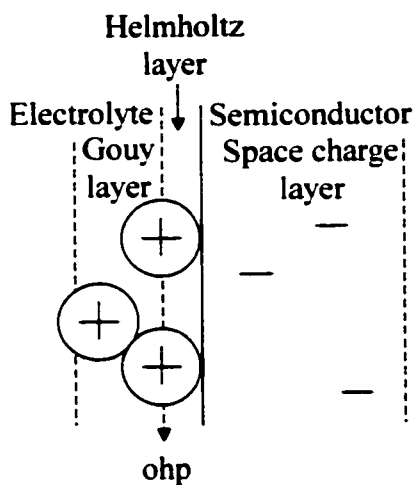


Figure 2.7. Schematic structure of the electric double layer at the semiconductor/electrolyte interface [Pleskov and Gurevich, 1986].

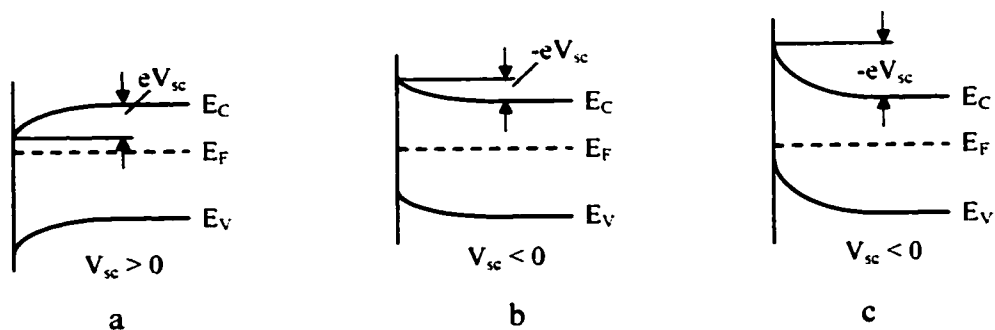


Figure 2.8. The band bending and charge distribution near the surface of an n-type semiconductor for various values of the potential drop, V_{sc} : a) accumulation layer; b) depletion layer; c) inversion layer [Pleskov and Gurevich, 1986].

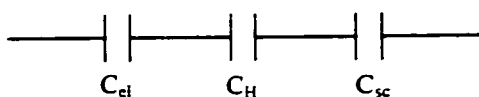


Figure. 2.9. The equivalent circuit describing the differential capacity, C , of the electric double layer.

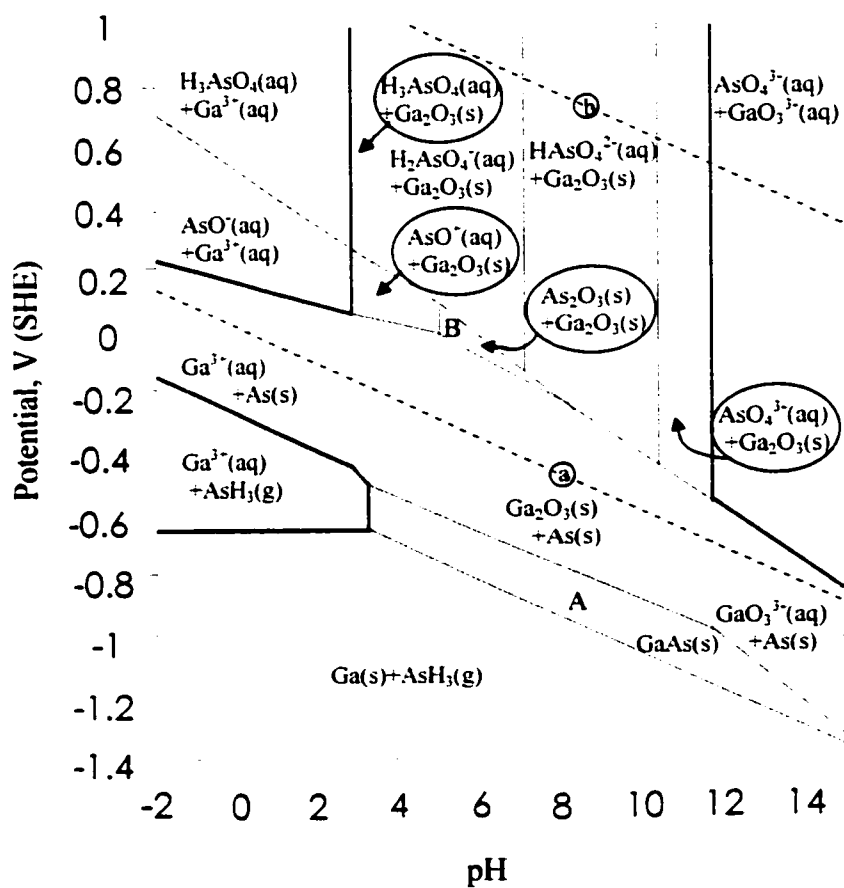


Figure 2.10. Equilibrium E-pH diagram for GaAs-H₂O at 25°C. The dashed “a” and “b” lines are the hydrogen and oxygen electrode potentials, respectively [Tromans et al, 1993].

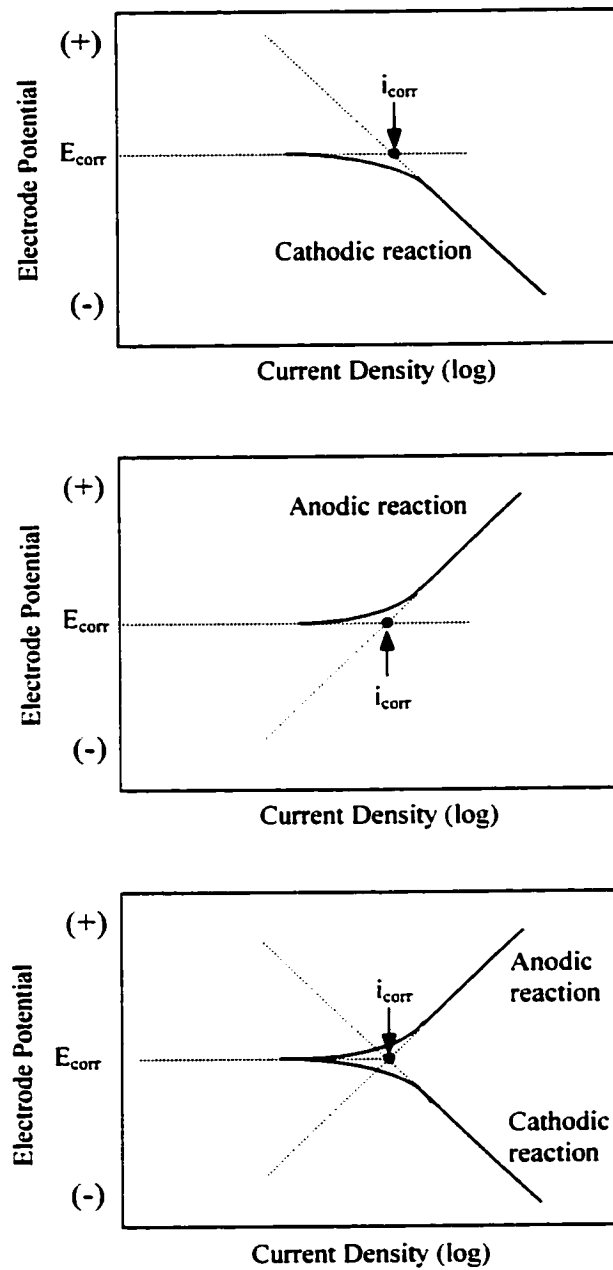


Figure 2.11. Illustration of three Tafel extrapolation methods of estimating corrosion rate [Dean, 1976].

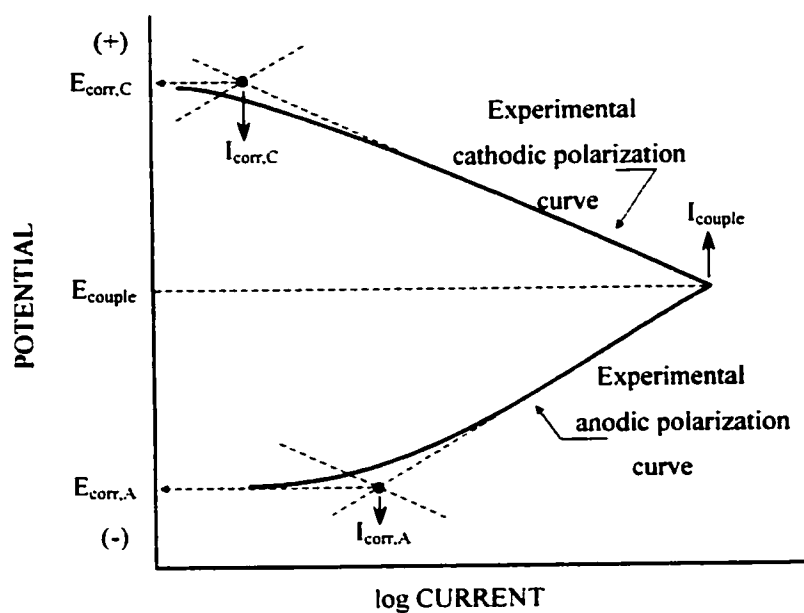


Figure 2.12. Schematic experimental polarization of an anode and cathode in a galvanic couple [Jones, 1996].

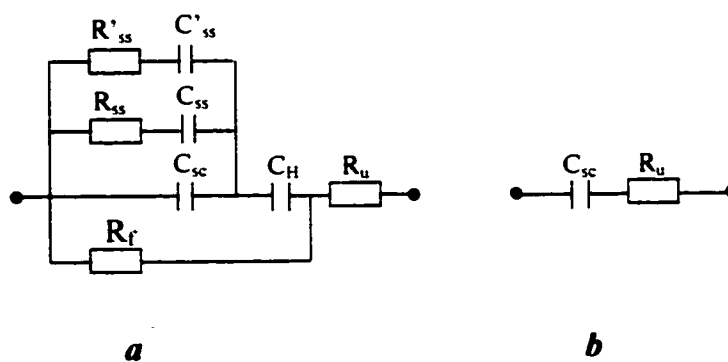


Figure 2.13. Equivalent circuits for impedance analysis of semiconductor electrodes.
a) A complex equivalent circuit; b) The simplest equivalent circuit [Finklea, 1988].

CHAPTER 3

EXPERIMENTAL

3.1. Electrochemical tests

3.1.1. Samples

The gallium arsenide wafers used in our electrochemical tests were n-type and p-type with different dopants and doping densities. The details are listed in Table 3.1.

Table 3.1. GaAs used in the tests

Material Type	Doping Density (cm^{-3})	Doping Element	Thickness of Doped Layer
n-GaAs	1×10^{17}	Silicon	Entire wafer
	1×10^{18}	Silicon	Entire wafer
	2×10^{18}	Silicon	500 nm
	5×10^{18}	Silicon	200 nm
p-GaAs	1×10^{18}	Carbon	500 nm
	4×10^{19}	Carbon	500 nm

3.1.2. Electrolyte solutions

The electrolyte solutions used in this work were 28.5% phosphoric acid ($\text{pH}=0.5$) made from 85% phosphoric acid, 1% hydrofluoric acid ($\text{pH}=3.3$) made from 48% hydrofluoric acid and deionized water ($\text{pH}\approx 6.5$), respectively. Semiconductor wafers are often cleaned in acid solutions and deionized water.

3.1.3. Specimens

The specimens strips were sectioned from wafers, with half the area covered with a standard Ti/Pt/Au (p-type) or Pd/Ge/Au (n-type) ohmic metallization layer. The backs and edges of the specimens were covered with lacquer, leaving a window of exposed semiconductor (Fig. 3.1). The metallization provided electrical contact, with only the exposed semiconductor submerged in the electrolyte during the electrochemical tests. Prior to the tests, the specimens were cleaned in a 1% HF solution for 2 minutes, to remove the air-formed oxide layer, and then rinsed with deionized water.

3.1.4. Potentiostatic polarization

Electrochemical measurements were done in a conventional three-electrode cell. A specimen was employed as the working electrode. A saturated calomel electrode (SCE) and a platinum mesh were used as the reference electrode and the counter electrode, respectively (Fig. 3.2). The potentiostat was an EG&G 273 model. All potentials used in this work were taken with reference to the SCE electrode. The specimen was first polarized at open circuit potential for about 40 minutes and then the proposed potential was applied.

3.1.5. Potentiodynamic polarization

The instrument used was the same as that for the potentiostatic polarization tests. Unlike potentiostatic polarization, a constant potential was applied and the variation in current with respect to time was measured, for potentiodynamic measurements, the initial and final potentials were set, the potential was increased at a set rate, and the change in potential with respect to current was recorded. A potential scanning rate of 1 mV/s was used. This test yielded a polarization curve.

3.1.6. Impedance

In the impedance tests, a small a.c. voltage (10 mV) was superimposed on the applied d.c. voltage with a frequency of 1000 Hz. Instead of the EG&G273 system, a Solartron 1255 B system was used. The semiconductor samples acted as the working electrode in a conventional three-electrode cell. A saturated calomel electrode (SCE) was connected to the cell through a salt bridge. A platinum mesh was used as the counter electrode as described in other electrochemical measurements. The capacitance was determined by performing a potential scan in the anodic direction.

3.1.7. Galvanic corrosion

The exposed specimen areas were varied, from 0.014 cm² to 2 cm². A conventional three-electrode cell, with a semiconductor specimen and a Si wafer covered with Au as the galvanic couple, with a saturated calomel electrode (SCE) as the reference electrode, was used to determine galvanic potential in direct galvanic measurements. The Au specimens also had different sizes to provide different area ratios relative to the semiconductors. Four pieces of Au samples were used in this work. The largest one was a 10.16 cm-diameter Au coated wafer embedded in a polymer, edge sealed with epoxy and lacquer to prevent contact of the backside of wafer with the solution during the tests (Fig.

3.3). Actually, the diameter of exposed wafer was 7.6 cm. Another three Au covered samples were directly cleaved from a Au coated wafer, with areas 1.7cm^2 and 1.36cm^2 and 0.24cm^2 , respectively. The galvanic current was measured using a potentiostat (ACM model Auto zero resistance ammeter). In this case, the galvanic current was directly determined as a function of time.

3.2. Optical microscopy

An Olympus PME3-ADL optical microscope was used to observe the morphology of samples before and after testing. Sample were etched in 1% HF to dissolve the oxide on the surface before electrochemical testing and then immediately examined with the optical microscope. The surface was also observed immediately after testing and then at several intervals (from hours to days) after testing.

3.3. Electron microscopy

3.3.1. Scanning electron microscopy (SEM)

SEM micrographs of the sample surfaces and elemental composition were obtained with a Hitachi S-2700 SEM equipped with a PGT Imix energy dispersive x-ray (EDX) analyzer (Ge x-ray detector). All images acquired were secondary electron images. EDX analyses were semi-quantitative and were performed at 20 kV, a difference in peak intensity representing a change in elemental concentration.

3.3.2. Transmission electron microscopy (TEM)

Changes in the semiconductor surface were also monitored with a JEOL 2010 TEM equipped with a Noran EDX detector to characterize elemental composition.

Selected samples were prepared for TEM tests to examine the surface changes and to determine the structure of the products on the surface after electrochemical testing.

There are many ways to prepare specimens for the TEM. The chosen method depends on both the type of material and the information required. Since structural and chemical variations close to the surface were of interest, cross-section specimens were prepared, so that interface could be imaged parallel to the electron beam. The procedure utilized for cross section preparation is as follows:

1. Cutting of the specimen

Since the backs and edges of the specimen tested in electrolyte solutions were covered with lacquer, prior to the cutting, the specimens were rinsed with acetone to remove the lacquer. The sample was then cut into 5mm×1.5mm slices with a diamond saw.

2. Adhesioin

The slices were glued face to face with a low temperature epoxy, which can cure at room temperature. Several silicon spacers were then glued to the specimen slices to produce several layers, rather like a sandwich or raft, with the specimen slices in the middle. A special vise was used to clamp the raft during curing (24-48 hours).

3. Grinding

After curing, the raft was thinned to 300-400 microns. It was first mounted on a polypropylene holder with a thermoplastic glue, then ground with sandpaper to the desired thickness. The sandwich should not be too thin or too thick; otherwise the slices are easily separated while handling, or dimpling times are too long.

4. Cutting the glued sections

The glued sections had to be cut into a 3-mm disk to meet the TEM specimen holder requirements. The sections were glued to an aluminum platen and cut with a Gatan 601 Ultrasonic Disc Cutter.

5. Dimpling

Because the disk is much thicker than that required for TEM, it was dimpled with a Gatan 656 Dimple Grinder. The disk was reglued onto the polypropylene holder and thinned with a bronze wheel using a diamond abrasive. The surface of the disk was polished to mirror finish with a felt pad and 1 μm diamond paste. Both sides were dimpled and polished. The thickness in the center should be as thin as possible to reduce ion milling times. The final central thickness was 0.1 μm .

6. Ion milling

The last step of specimen preparation was ion milling. The delicate thin TEM specimen was bombarded with energetic ions to sputter material from the film until a small hole was produced at the center. The region around the hole was electron transparent. A Gatan 600 Dual Ion Mill was used for sputtering. Before ion-beam thinning, the specimen was cooled in the chamber with liquid- N_2 for 45 minutes. Cooling the specimen can minimize atom migration in or on the specimen and reduce preferential sputtering effects. The specimen was rotated slowly during thinning and the tilt angle of specimen surface relative to the ion guns was 15° .

During ion milling, the voltage and current density of ion beam were 5 kV and 0.5 mA respectively. After perforation the voltage was reduced to a 3.5 kV to reduce the amount of ion damage in the specimen.

3.4. Atomic force microscopy (AFM)

Nanometer-scale morphological images were acquired using a Nanoscope-E III AFM equipped with AS-130 E scanner through direct contact between a sample surface and a probe tip mounted on the end of a cantilever microbeam. The cantilever length is 200 μm and a spring constant is 0.06 Nm^{-1} . Silicon nitride tips, were placed under ultraviolet light in a horizontal laminar flow hood for 3 hours prior to assembly to destroy any organic contaminant that may adhere onto the tips. The scan rate was 4 Hz, and a resolution 256 x 256 pixels per image was selected. All measurements were carried out at room temperature, under ambient atmosphere.

3.5. X-ray photo electron spectroscopy (XPS)

XPS spectra were acquired on a SSX-100 spectrometer with a monochromated AlK_{α} source. The spot size and take-off angle were 600 μm and 37° , respectively. The pass energies of the concentric hemispherical analyzer were maintained at about 100 eV for a broad scan from 1-1000 eV and about 50 eV for narrow scans around the peaks of As 3d, Ga 3d, O 1s and C 1s. The 1s photoelectrons of hydrocarbon contaminant carbon at a binding energy of 284.5 eV were taken as an internal reference for calibration of the surface charge.

3.6. Inductively coupled plasma (ICP) spectroscopy

ICP was employed to compare the dissolution rate of As and Ga by analyzing ion concentrations of the arsenic and gallium in either deionized water or phosphoric acid. All corrosion cell and glass sampling bottles were immersed in 10% HCl for more than 2 hours before being used for electrochemical tests and to collect the solutions.

3.7. X-ray diffraction (XRD)

The structures of sample surface were examined using a Rigaku Rotaflex X-ray diffractometer equipped with a 4.4 kW rotating anode Cu K α X-ray source and a thin film camera. The detector was scanned between 10° and 90°, and diffractometer scanning rate was 3°min⁻¹. The radiation with a wavelength of 0.1541 nm was used.

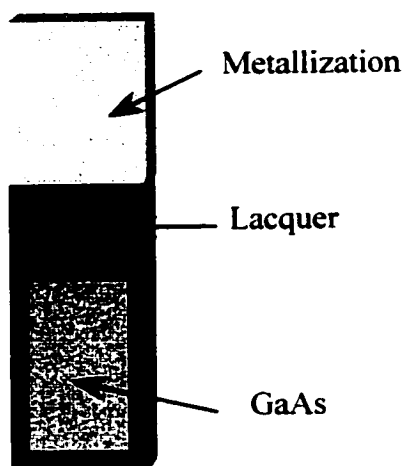


Figure 3.1. Schematic specimen for the electrochemical tests.

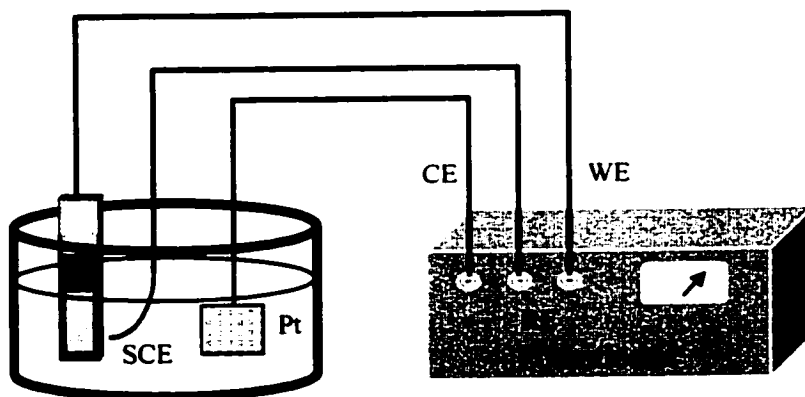


Figure 3.2. Schematic three-electrode cell and potentiostat.

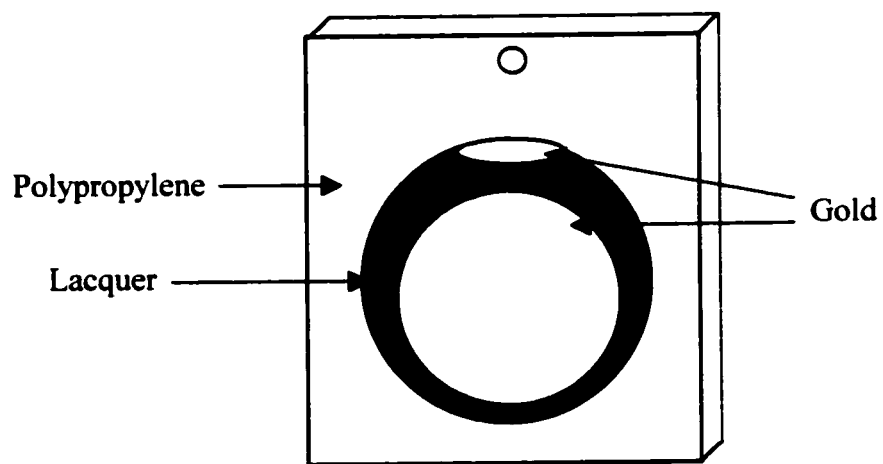


Figure 3.3. Schematic gold wafer for galvanic corrosion tests.

CHAPTER 4

RESULTS

4.1. Potentiodynamic polarization

A potential sweep was applied and the current response was measured. This technique is generally used to produce a qualitative picture of a substance in a given solution. It also detects any tendency of the substance to corrode or passivate. In this work, the sweep rate was 1mV/s.

4.1.1. Polarization curves generated for GaAs in acid

Initial tests were done in both phosphoric acid and hydrofluoric acid. Polarization curves for n-GaAs and p-GaAs, at the same doping level (10^{18}cm^{-3}), in HF and H_3PO_4 in daylight are shown in Fig. 4.1. The anodic current densities for p-GaAs is much larger than n-GaAs. The curves for both solutions are very similar; as such, subsequent tests were done in phosphoric acid only.

Fig. 4.2 shows a group of polarization curves for n-type GaAs with different doping densities, in phosphoric acid in daylight. From the figure, all n-type GaAs samples have the same corrosion tendency. It is clear that there are three main regions for

n-GaAs anodic dissolution in phosphoric acid. At low potential, in the active region, current density increases with increasing potential. When the anodic potential reaches a certain value, the current density becomes constant ($1.5 \times 10^{-5} \text{ A/cm}^2$), and the sample “passivated”. The current density then increases markedly at a critical potential (breakdown potential), as the sample goes into transpassivation region. The potential corresponding to the onset of a fixed current density is about the same (-0.05 V vs. SCE) for n-GaAs doped at 10^{17} cm^{-3} , 10^{18} cm^{-3} and $2 \times 10^{18} \text{ cm}^{-3}$. The potential for the $5 \times 10^{18} \text{ cm}^{-3}$ sample is slightly higher (0.1 V vs. SCE). The breakdown potential depends on doping concentration – breakdown potential decreases as doping concentration increases (Fig. 4.3).

For p-type GaAs, the corrosion tendency and current densities are similar (Fig. 4.4) at low potential ($< 0.2 \text{ V}$). When the polarizing potential is higher than 0.2 V , the current density still increases markedly for the $4 \times 10^{19} \text{ cm}^{-3}$ p-GaAs sample until it reaches just over 10^{-3} A/cm^2 . At this point the current density reverses to a lower value and remains approximately constant when the potential is increased. The current density does not change markedly when the potential is above 0.2 V for the 10^{18} cm^{-3} p-GaAs sample. Above 0.7 V , the two polarization curves are almost vertical with a fairly small difference between the curves (< 1 order of magnitude difference in current density).

To determine the surface change for n-type GaAs when the polarization potential is above the breakdown potential, atomic force microscopy (AFM) was used to characterize the surface of the sample prior to and immediately after testing. Fig. 4.5a shows a typical image of a clean sample (n-GaAs, $2 \times 10^{18} \text{ cm}^{-3}$) before exposure to the electrolyte solution. The surface is very smooth and the root mean square roughness is 0.6 nm . Fig. 4.5b shows the same sample polarized to 1.5 V , which is higher than the breakdown potential ($\sim 0.6 \text{ V}$), in phosphoric acid in daylight. The root mean square roughness is 5.6 nm . Comparing with that before testing, it is clear that the surface is rougher with a few pores penetrating into the substrate, indicating the occurrence of localized corrosion when the potential reaches the breakdown potential. Fig. 4.5d shows

the section analysis corresponding to Fig. 4.5c. The surface is rough and the depth of the pore is ~25nm.

The corrosion behavior of GaAs in 28.5% H_3PO_4 in the dark was also examined and compared with that under illumination. For n-GaAs, the current density is more than an order of magnitude lower in the dark than that in light (Figs. 4.6-4.10). Although there are differences in the current density for p-GaAs in the dark and light, they are much smaller compared with that for n-GaAs.

For lower doped n-GaAs ($1 \times 10^{17} \text{ cm}^{-3}$ and $1 \times 10^{18} \text{ cm}^{-3}$), above the corrosion potential, there is a relatively large potential range within which the corrosion current density in daylight is larger by about an order of magnitude than that for n-GaAs tested in the dark (Figs. 4.6 & 4.7). The difference decreases with increasing potential. The current densities obtained in daylight and dark are approximately superimposed when the potential reaches a certain value (breakdown potential). These potentials are 1.1 V and 1.2 V vs SCE for $1 \times 10^{17} \text{ cm}^{-3}$ and $1 \times 10^{18} \text{ cm}^{-3}$ GaAs samples, respectively. For n-GaAs ($2 \times 10^{18} \text{ cm}^{-3}$), the current densities tested in daylight and dark are almost parallel above the corrosion potentials, with the former one larger by about an order of magnitude (Fig. 4.8). This difference remains constant until the potential reaches 0.6 V (breakdown potential), above which the difference becomes very small, but two lines are still parallel. For higher doped n-GaAs ($5 \times 10^{18} \text{ cm}^{-3}$), although the corrosion current density is larger in daylight than that in the dark above the corrosion potential, the difference decreases quickly with increasing the potential (Fig. 4.9). When the potential reaches a certain value (about 0.8 V), the current density is reduced and remains constant with increasing potential.

The polarization curves for n- and p-GaAs (10^{18} cm^{-3}) tested in phosphoric acid in both the dark and daylight are compared in Fig. 4.7. It is clear that the polarization curves in the dark and daylight are very close for p-GaAs, which indicates that the illumination

has little effect on anodic dissolution of p-GaAs. For n-GaAs polarized in the dark, the anodic current density in the vicinity of 0.75 V is several orders of magnitude lower than that for p-GaAs, in either daylight or the dark, and one order of magnitude lower than n-GaAs tested in daylight. For higher doped p-GaAs ($4 \times 10^{19} \text{ cm}^{-3}$), the polarization curves tested in the dark and daylight are very close except a small difference between the open circuit potentials (Fig. 4.10). Above a critical potential (about 0.4 V), the current density is reduced to the similar values for samples tested in the dark and daylight, then remains constant with increasing potential like n-GaAs ($5 \times 10^{18} \text{ cm}^{-3}$).

4.1.2. Polarization curves generated for GaAs in deionized water

The corrosion behavior of GaAs in deionized water was also studied using polarization curves (Fig. 4.11-4.17).

The polarization curves for n-GaAs are very similar, indicating that the electrochemical processes are very similar in deionized water in daylight (Fig. 4.11). There are differences for higher doped n-GaAs samples ($2 \times 10^{18} \text{ cm}^{-3}$ and $5 \times 10^{18} \text{ cm}^{-3}$); the current density increases with increasing potential above a certain value (0.6 V). For the lower doped n-type GaAs samples (10^{17} cm^{-3} and 10^{18} cm^{-3}) there is very little change with the potential above 0.6 V

For the p-type GaAs samples (10^{18} cm^{-3} and $4 \times 10^{19} \text{ cm}^{-3}$), the polarization curves are very similar with a small difference in magnitude in current densities (slightly higher for $4 \times 10^{19} \text{ cm}^{-3}$ sample), indicating the same corrosion behavior for these two samples (Fig. 4.12).

Comparison of the results from n- and p-type GaAs tested in deionized water under illumination shows that the current density for n-GaAs with lower dopants (10^{17}cm^{-3} and 10^{18}cm^{-3}) remains constant when the potential exceeds 0.5 V, increasing with the potential for those with higher dopants ($2 \times 10^{18}\text{cm}^{-3}$ and $5 \times 10^{18}\text{cm}^{-3}$); for p-GaAs it increases with increasing potential. It is clear that the anodic dissolution rate for p-GaAs is higher than for n-GaAs (10^{18}cm^{-3}) at potentials above 0.5 V (Fig. 4.13).

Fig. 4.14 shows the polarization curves for n-GaAs with different doping densities in deionized water tested in the dark. The anodic dissolution is a function of potential, i.e., the current density increases with increasing potential. For a given anodic potential, current densities increase as the doping level increases. There is a certain potential, above which, the current density decreases with increasing potential for a while for $2 \times 10^{18}\text{cm}^{-3}$ (~ 1 V) and $5 \times 10^{18}\text{cm}^{-3}$ (~ 0.5 V) GaAs, respectively, before increasing again with increasing potential as happened before. This phenomenon was not observed for $1 \times 10^{18}\text{cm}^{-3}$ GaAs in the range tested; however, it was expected to occur at higher potentials.

As with samples tested under illumination, there are no major differences for p-GaAs samples tested in deionized water in the dark (Fig. 4.15). The corrosion current density increases with increasing potential until about 0.5 V, above which, the current density decreases with increasing potential before continually increasing with increasing potential.

Comparing the polarization results in the dark and daylight for n-GaAs (Fig. 4.16) and p-GaAs (Fig. 4.17) with the doping density 10^{18}cm^{-3} , it was found that at lower potential, the current density is larger in daylight than that in the dark for n-GaAs. When the potential reaches about 0.8 V, the results are reversed. The curves for p-GaAs are very close.

4.2. Potentiostatic polarization

Upon routine examination of semiconductor surfaces after potentiodynamic polarization testing, surface features were observed. For some samples tested in this work, the particles were observed after exposure to air for one day and the size and number increased with increasing exposure time. For some samples, this phenomenon was not observed. To investigate the process and mechanism of particle formation, potentiostatic polarization tests were applied in this work.

A constant potential was applied and the current was monitored as a function of time. Generally, constant potential experiments can be used to examine the long-term corrosion behavior at a polarized potential. The anodic current measured during the exposure is a measure of the corrosion rate. Corrosion rates can change because of changes at the electrode surface. Some of these changes include: 1) a corrosion product layer or a passive film continues to grow over a long period of time; 2) preferential dissolution leads to a surface enrichment of one constituent of a compound; 3) localized corrosion occurs.

The applied potentiostatic polarization potentials were chosen based on the potentiodynamic polarization curves. The anodic curves for n-type GaAs had three main regions (active range, “passivated” range and “transpassivated” range) (Fig. 4.2). The p-type GaAs samples had two ranges (active range and “passivated” range) (Fig. 4.4).

4.2.1. *n-type GaAs*

The experiments were first done in the range of passivation for all samples since the current density was constant for a range of potential. In addition, the current density

was very close for n-GaAs samples in this range. The SEM observations specimens polarized at 0.75V (for 10^{17}cm^{-3} and 10^{18}cm^{-3}), 0.4V (for $2 \times 10^{18}\text{cm}^{-3}$) and 0.3V (for $5 \times 10^{18}\text{cm}^{-3}$) for 2 hours, in both phosphoric and hydrofluoric acid in both daylight and dark, are summarized in Table 4.1. Note, that all results are for 7 days after testing. With the exception of n-GaAs tested in the dark, all samples had significant numbers of faceted particles on the surface. The surfaces of n-GaAs tested in the dark were essentially featureless, virtually identical to untested surfaces.

Table 4.1. Surface morphology of GaAs samples 7 days after polarization

Specimen n-GaAs	Phosphoric	Acid	Hydrofluoric	Acid
	light	dark	light	dark
10^{17}cm^{-3}	particles	featureless	particles	featureless
10^{18}cm^{-3}	particles	featureless	particles	featureless
$2 \times 10^{18}\text{cm}^{-3}$	particles	featureless	particles	featureless
$5 \times 10^{18}\text{cm}^{-3}$	particles	featureless	particles	featureless

Crystalline particles began to appear on the specimen surface after exposure to air for about one day, except for samples tested in the dark. As the time of exposure to air increased, the particles grew until to a limiting size was reached.

SEM secondary electron (SE) images for an n-GaAs specimen (10^{17}cm^{-3}) after potentiostatic tests in phosphoric acid in daylight are shown in Fig. 4.18. The surface was relatively smooth when exposed to air for less than 10 minutes (Fig. 4.18a) and there was no apparent change compared with the morphology of the cleaned specimens before the potentiostatic tests. Crystalline particles began to appear on the specimen surface after exposure to air for about 20 hours. Fig. 4.18b shows the specimen surface after exposure to air for 4 days, indicating the presence of particles several microns in size. Figs. 4.18c

and 4.18d clearly show that the number and size of particles increased with increasing air exposure time. Fig. 4.19 shows a SEM image of the same sample shown in Fig. 4.18d along with EDX spectra of the substrate and one of the particles. Fig. 4.19b is an EDX spectrum from the substrate (A) and Fig. 4.19c is an EDX spectrum from a particle (B) shown in Fig. 4.19a. It is clear that the particles are enriched with As relative to the GaAs surface. An oxygen peak is also present in Fig. 14c, indicating at least some oxidation of As.

To investigate whether the formation of the surface particles is independent of potential, similar experiments were performed at the corrosion potential in phosphoric acid. SEM images taken from these samples showed featureless surfaces, even after several days of exposure to air; no As-rich particles were detected.

To investigate compositional changes on the surface after the electrochemical tests in the acid solution, n-GaAs (10^{17} cm^{-3}) specimens were analyzed with XPS prior to testing, immediately after testing and after 7 days of exposure to air. Carbon, O, Ga and As were detected with XPS, while Si (dopant) and P (phosphoric acid) were not. Figs. 4.20a and 4.21a are the Ga 3d and As 3d spectra, respectively, for the as-received specimen. Peak deconvolutions were performed on the spectra. The binding energies for deconvolution are Ga 3d (GaAs)= 18.8-19.2 eV and Ga 3d (Ga_2O_3)= 19.6-21.0 eV, As 3d (GaAs)= 40.7-40.9 eV, As 3d (As_2O_3)= 44.5-45.2 eV and As 3d (As_2O_5)= 45.8-46.3 eV, which were obtained from the literature [Moulder et al, 1995]. The Ga 3d spectrum (Fig. 20a) shows two merged peaks with binding energies at about 18.9 eV and 20.3 eV, respectively. The peak at about 18.9 eV can be identified as GaAs and the one at about 20.3 eV is from Ga_2O_3 . The As 3d spectrum (Fig. 21a) is made up of three peaks: As 3d from GaAs at about 40.9 eV, As 3d from As_2O_3 at about 44.5 eV and As 3d from As_2O_5 at about 45.8 eV. These spectra show that the surface of the as-received specimen was covered with a mixed oxide layer made up of As_2O_3 , As_2O_5 , and Ga_2O_3 . The GaAs peaks observed in Ga 3d and As 3d were from the substrate.

The XPS spectra for Ga 3d and As 3d, obtained for a specimen immediately after polarization in phosphoric acid, are shown in Figs. 4.20b and 4.21b respectively. The prominent Ga₂O₃ peak in Figs. 4.20a was not detected in Fig. 4.20b, indicating that Ga₂O₃ was completely dissolved in the phosphoric acid. Comparing the intensity of the signal in Fig. 4.21b with that in Fig. 21a, it is clear that As₂O₃ was also dissolved in the solution. As₂O₃ was the only oxide remaining on the surface after polarization. The As 3d spectra show that the GaAs peak detected very clearly at about 40.9 eV for the as-received specimen (Fig. 4.21a) became undetectable, while a peak at a binding energy of about 41.7 eV was present after polarization (Fig. 4.21b). This peak can be identified as As [Moulder et al, 1995]. The As peak is so strong that it is difficult to pick out the weak As 3d peak arising from the substrate GaAs without ambiguity. On the other hand, the Ga 3d peak from the GaAs substrate still can be seen clearly in the Ga 3d spectrum (Fig. 4.20b) because the surface is depleted in Ga, and therefore, the Ga 3d photoelectrons from the substrate become the main contributors to this spectrum. This indicates that the outermost surface layer after polarization testing is rich in As with a small amount of As₂O₃. The surface compositions shown in Table 4.2 also confirm this observation. These results are consistent with the Pourbaix diagram (Fig. 2.10) for the GaAs-H₂O system, which suggests that both Ga₂O₃ and As₂O₃ are soluble in acidic solutions [Tromans et al, 1993].

Table 4.2. Composition (at%) at surface of n-GaAs polarized in H₃PO₄ analyzed, by XPS

	As	Ga	O	C	As/Ga
As received	12.2	23.0	37.2	27.6	0.53
Immediately after polarization	29.1	1.2	7.5	62.2	24.3
7 days after polarization	20.5	6.0	15.0	58.5	3.2

The XPS spectra for Ga 3d and As 3d electrons, for specimens exposed to air for 7 days following the electrochemical tests, are shown in Figs. 4.20c and 4.21c. Comparison of the As 3d spectrum obtained from a freshly polarized specimen (Fig. 4.21b) with that obtained for the aged specimen (Fig. 4.21c) indicates that the As₂O₃ peak

intensity has increased after exposure to air. No detectable As_2O_5 was found on the aged surface. The Ga 3d peak (Fig. 4.20c) has a shoulder on the higher binding energy side. Peak synthesis shows that a peak at a binding energy of about 20.3 eV is present. This peak is attributed to Ga_2O_3 , the same as that seen clearly in the Ga 3d spectrum obtained from the as-received specimen (Fig. 4.20a).

As described above the surfaces of n-GaAs were essentially featureless immediately after potentiostatic polarization tests in the “passivation” range in acid solution either in the dark or light. In order to examine the surface change after tests, which might be too small to be observed with SEM, n-GaAs ($2 \times 10^{18} \text{cm}^{-3}$) TEM samples were prepared immediately after potentiostatic polarization at potentials corresponding to the “passivation” region and were compared with samples tested in other two potential ranges (active and transpassivated). Based on the polarization curve in Fig. 4.2, three potentials (-0.15 V, 0.4 V and 0.75 V) were chosen for potentiostatic polarization tests in phosphoric acid in daylight.

The surface of the sample polarized at -0.15V has been roughened slightly, but otherwise there is no other visible change (Fig. 4.22a). EDX analysis of the bulk and surface regions indicates very similar compositions, with the exception of the small oxygen peak in the surface layer (Fig. 4.22b and 4.22c). At 0.4V, a thin layer is visible on the GaAs surface (Fig. 4.23a). The layer is As-rich with a small amount of Ga and O (Fig. 4.23c). At 0.75V, the surface was porous with porosity extending 500 nm into the bulk (Fig. 4.24).

Figs. 4.25b and 4.26b show the Ga 3d and As 3d XPS spectra, respectively, for a specimen (n-GaAs, 10^{17}cm^{-3}) immediately after polarization testing in deionized water. By comparing the spectra for the specimen after the potentiostat test with those for the as-received specimen (Figs. 4.25a and 4.26a), it is obvious that the relative intensities for As_2O_3 , As_2O_5 and Ga_2O_3 have increased significantly during potentiostatic testing. The GaAs peaks in Ga 3d and As 3d spectra arising from the substrate are much weaker in intensity than those obtained from the as-received specimen. These results indicate that

thickening of the oxide film has occurred in the deionized water. From Table 4.3, it is seen that during the polarization in the deionized water, arsenic oxide might partially dissolve resulting in the decrease in the As/Ga ratio in the surface film. XPS spectra for a specimen after exposure to air for 7 days following potentiostatic testing in deionized water are shown in Figs. 4.25c and 4.26c. Comparing the relative intensities for Ga_2O_3 and As_2O_3 after 7 days, with those for the freshly polarized specimen, it is seen that there is very little change in the relative intensities for both Ga_2O_3 and As_2O_3 . The data in Table 4.3 shows that the As/Ga ratio is reduced slightly.

Table 4.3. Composition (at%) at surface of n-GaAs polarized in deionized water analyzed, by XPS

	As	Ga	O	C	As/Ga
As received	12.2	23.0	37.2	27.6	0.53
Immediately after polarization	7.5	18.4	37.8	36.3	0.41
7 days after polarization	7.0	18.7	47.5	26.8	0.37

To test the surface change at high potential, n-GaAs (10^{18}cm^{-3}) samples were potentiostatically polarized in the dark in phosphoric acid at 7 V for 2 h and then examined immediately after testing. SEM images from one such sample are shown in Fig. 4.27. Dendritic, faceted structures are apparent, similar to those reported [Li and Bohn, 2000; Lockwood et al, 1999] and these grew from the specimen edges towards the specimen centre. The structures were, in fact, visible with the unaided eye. EDX analysis clearly shows that the particles are As oxide (Fig. 4.27c).

4.2.2. *p-type GaAs*

In contrast to n-GaAs, there are only two significant potential ranges for p-GaAs, an active range and a “passivation” range (Fig. 4.4). As with n-GaAs tested in daylight, particles were formed after exposure to air for about 1 day; however, particles were found

for samples tested in both the dark and in daylight. Same as for n-GaAs, the SEM observations were also achieved for p-GaAs polarized at 0.75V for 2 hours, in both phosphoric and hydrofluoric acid in both daylight and dark, and are summarized in Table 4.4. Same as n-GaAs tested in daylight, all samples had significant numbers of faceted particles on the surface.

Table 4.4. Surface Morphology of p-GaAs Samples 7 Days After Polarization

Specimen p-GaAs	Phosphoric	Acid	Hydrofluoric	Acid
	light	dark	light	dark
10^{18} cm^{-3}	particles	particles	particles	particles
$4 \times 10^{19} \text{ cm}^{-3}$	particles	particles	particles	particles

To investigate the surface change immediately after testing, TEM micrographs were also obtained for p-GaAs ($4 \times 10^{19} \text{ cm}^{-3}$). All samples were potentiostatic polarized in daylight for two hours in phosphoric acid. The potentials chosen were 0.15V, 0.4V and 0.75V and correspond to anodic dissolution, what appears to be the onset of passivation and the passivated region (Fig. 4.4). In all three cases, an As-rich layer is present on the GaAs surface. The composition of the layer thickness is similar to that formed on n-type GaAs, but is much thicker. In the active range, the layer is about 50 nm thick (Fig. 4.28). At 0.4V, the “passive” potential, the layer thickness increases to 140 nm (Fig. 4.29). The layer at this stage was thick enough to analyze crystallographically and was found to be amorphous. Within the passivation region, the layer is a little thicker (about 150 nm) and is quite uniform (Fig. 4.30).

4.3. Galvanic corrosion measurements

A galvanic cell is formed when two or more dissimilar materials are connected electrically while all are immersed in an electrolyte solution. Any material has a unique corrosion potential, E_{corr} , when immersed in a corrosive electrolyte. When any two different materials are electrically coupled together, the one with the more negative or active E_{corr} has an excess activity of electrons, which are lost to the more positive one, and is corroded preferentially by galvanic corrosion.

After fabrication, metallized semiconductors are often cleaned in acid solutions or deionized water. Defects such as voids on the metallization layer can allow the solution to penetrate making contact with both the metallization and semiconductor, creating a galvanic corrosion environment. The outermost metal is more noble and its corrosion potential is much more positive compared with the semiconductor. In this galvanic cell, the outer metal (typically Au) acts as a cathode, and the underlying semiconductor as an anode. Thus, the semiconductor may be corroded during cleaning.

The extensive application of III-V semiconductors in optoelectronic devices, necessitates that more attention be paid to the galvanic corrosion behavior of them. The purpose of this work was to study the galvanic behavior of III-V semiconductors in contact with gold. Gold was chosen since both n- and p-type semiconductors usually have Au as the outermost metal layer in their respective ohmic contacts. The effect of area ratio was investigated with the ultimate goal of forming galvanic cells and predicting the galvanic corrosion rate. Two methods were used to determine galvanic corrosion: (1) direct galvanic measurements and (2) superposition of the individual anodic and cathodic polarization curves to indirectly predict galvanic corrosion. The experiments were done using GaAs, both n- and p-type, at different doping levels, and 28.5% H_3PO_4 was chosen as the electrolyte since phosphoric acid is commonly used for wafer cleaning.

4.3.1. Direct galvanic corrosion measurements

In the tests, Au with different areas was connected with GaAs samples of varying areas in the electrolyte. The measured galvanic current densities in phosphoric acid for a number of couples with different cathode-to-anode area (C/A) ratios as a function of time were recorded at room temperature in daylight. The anode and cathode polarized until they reached the same potential; at this time current density and potential showed by the ZRA were independent on time.

Direct measurements were performed on three samples, n-GaAs with a doping density of 10^{18}cm^{-3} and p-GaAs with doping densities of 10^{18}cm^{-3} and $4 \times 10^{19}\text{cm}^{-3}$ respectively (Fig. 4.31). The studied range of C/A ratio was 0.1 to 10000. The measured galvanic current density increases with increasing C/A area ratio for both p-GaAs and n-GaAs at low C/A area ratios (<10). For n-GaAs, the galvanic current density becomes approximately constant once the C/A ratio reaches about 5 (Fig. 4.31), indicating that a large C/A area ratio does not have a marked effect on corrosion rate. The corrosion rates are very similar for the two p-type semiconductors at the same area ratios. For both p-GaAs samples, the current density increases continually with increasing C/A area ratio. For n-GaAs, at low area ratio (<100), the current density is larger by about an order of magnitude than that for p-GaAs. However, the reverse is true when the C/A ratio exceeds 100.

4.3.2. Indirect galvanic corrosion measurements

Cathodic polarization curves of noble materials and anodic polarization curves of less noble materials in electrolyte solutions can be superimposed to predict galvanic corrosion rates. Polarization measurements on both n- and p-GaAs with different doping densities, as well as Au were therefore done to predict galvanic corrosion rates of the semiconductors.

Superimposed polarization curves for n-type GaAs and Au in phosphoric acid are shown in Fig. 4.32. The intersection of Au cathodic curves and GaAs anodic curves gives the galvanic corrosion current densities for anodes at different C/A ratios. Three distinct regions can be identified with the Au cathodic curve. It can be concluded that the cathode process consists of oxygen reduction and hydrogen evolution. For hydrogen evolution corrosion, both the cathode and the anode processes are controlled by activation polarization. In the case of oxygen reduction, there is limited solubility of oxygen in solution, so that concentration polarization dominates the process where current density reaches a critical value. As a result, the corrosion rate can be controlled by the diffusion of oxygen. The polarization curve in 28.5% phosphoric acid (Fig. 4.32) can be used as an example. At higher potentials (>-0.14 V), the cathodic process proceeds at a small current density where there is enough oxygen on its surface. The electrode reaction is:



When the current density increases to a critical value ($\sim 7 \times 10^{-6} \text{ A cm}^{-2}$) as the potential is decreased to a certain value (-0.14 V), there is not enough oxygen on the cathode surface for reaction. The slope of the polarization curve increases and the cathodic current density does not increase as fast as before. Thus, the process is controlled by oxygen diffusion. With a further decrease in potential (below -0.35 V), hydrogen reduction occurs.



The cathodic behavior is then due to both hydrogen evolution and oxygen reduction. Since the reaction is in acid solution, there are sufficient hydrogen ions. Therefore, the slope of polarization curve decreases; the current density increases rapidly again. At this time, hydrogen gas is evolved in the reaction.

Although the cathodic behavior can be due to either oxygen reduction or hydrogen evolution, only oxygen reduction is expected for this work based on the portion of the Au cathodic curve that intersects the GaAs anodic curves.

It is apparent from Fig. 4.32 that the galvanic current densities increase with increasing C/A ratio only for lower C/A values, up to $C/A \approx 10$ for 10^{18} cm^{-3} and $2 \times 10^{18} \text{ cm}^{-3}$ and $C/A \approx 100$ for $5 \times 10^{18} \text{ cm}^{-3}$. For the lower C/A ratios (< 100), the galvanic current densities decrease with increasing doping density. The mixed potentials of the galvanic couples are also lower at low C/A ratios. In this range, the galvanic current density is lowest for the $5 \times 10^{18} \text{ cm}^{-3}$ GaAs sample. When the C/A ratio is increased, the galvanic current densities for the various doping densities are closer. Therefore, n-GaAs with higher doping density is lightly corroded when in contact with a noble metal at low C/A ratios. When the C/A ratio is increased above 10 (or 100 for the $5 \times 10^{18} \text{ cm}^{-3}$ sample), which is above a critical potential for each doping level, there is very little change in the galvanic current density.

For p-type GaAs in phosphoric acid, as with n-GaAs, the open circuit potential increases as the doping density increases (Fig. 4.33). Because their anodic polarization curves are very similar, the galvanic current densities for the two doping levels are not much different. In addition, there is also a range of potential, where the current density is almost constant (above about 0.4 V SCE). The galvanic mixed potentials and current densities, for both samples, increase with C/A ratio up to at least 100,000.

4.3.3. Comparison

In order to determine the validity of the galvanic corrosion results from the superposition of polarization curves, galvanic current densities for $1 \times 10^{18} \text{ cm}^{-3}$ (n- and p-type), and $4 \times 10^{19} \text{ cm}^{-3}$ (p-type) GaAs measured directly are compared with predicted or indirect values (from polarization curves). Six points were selected, representing various C/A area ratios from 0.1 to 10,000, by intersection of cathodic (Au) curves with each of

the anodic curves (GaAs). Fig. 4.34 shows the direct and indirect measurement results for n-GaAs (10^{18} cm^{-3}). In both cases, the current densities increase at low area ratios and then become constant when the ratio reaches about 5-10, indicating excellent agreement between measured and predicted results. The p-GaAs comparisons are shown in Figs. 4.35 (10^{18} cm^{-3}) and 4.36 ($4 \times 10^{19} \text{ cm}^{-3}$), respectively. The agreement is quite good in both, with both semiconductors exhibiting an increasing galvanic current density with increasing C/A area ratio.

Galvanic current densities for GaAs in phosphoric acid in the dark were also obtained through the superposition of polarization curves. Polarization curves for n-type and p-type GaAs (10^{18} cm^{-3}) are shown in Fig. 4.7 along with their counterparts in daylight. The polarization curves are similar for p-type GaAs in dark and daylight, whereas they are different for n-type GaAs. The anodic current densities for n-type GaAs are significantly lower for samples tested in the dark relative to daylight.

Galvanic current density plots for the p-GaAs and n-GaAs samples are shown in Figs. 4.37 and 4.38 respectively. The corrosion rates for the p-type samples increase with increasing C/A area ratios both in the dark and daylight (Fig. 4.37). For the 10^{18} cm^{-3} (p-type) GaAs sample, the corrosion rate in daylight is somewhat larger than in dark, but for the $4 \times 10^{19} \text{ cm}^{-3}$ sample, the difference between daylight and dark galvanic current densities is quite small. The n-GaAs samples show a much larger difference between the daylight and dark galvanic current density curves (Fig. 4.38), but the difference decreases as the doping level increases.

4.3.4. Galvanic corrosion rates

Anodic current densities can be converted to corrosion rates expressed in the standard way as millimeter penetration per year (mm/y) from the following equation [Bradford, 2001]:

$$\text{corrosion rate (mm/y)} = 3.27 \times 10^3 i_{\text{corr}} w / (n d) \quad (4.3)$$

where

i = anodic current density, Acm^{-2} ;

w = atomic or molecular weight, g/mole (144.64 g/mole for GaAs);

n = ionic charge associated with the electrode process ($n=8$ for GaAs dissolution);

d = density of the anode, g/cm^3 (5.31 g/cm^3 for GaAs).

Because of the small dimensions and time scales associated with microelectronic/optoelectronic device processing, nanometer penetration per minute is probably a more meaningful unit for corrosion rate. Thus, Eq. 4.3 can be rewritten as

$$\text{corrosion rate (nm/min)} = 6.22 \times 10^3 i_{\text{corr}} w / (n d) \quad (4.4)$$

The galvanic corrosion rates of GaAs in contact with Au in phosphoric acid at various C/A area ratios are summarized in Table 4.5. In general, corrosion rates are higher in daylight compared with in the dark and the rates increase with increasing C/A area ratio. Also of interest, is the relative difference in corrosion rates for p-GaAs vs n-GaAs. Corrosion rates are higher for n-GaAs at low C/A ratios, but the trend is reversed at higher ratios.

Table 4.5. Galvanic corrosion rate in phosphoric acid

Anode	Condition	Cathode/Anode area ratio	Galvanic current density (A/cm ²)	Corrosion rate (nm/min)
10 ¹⁸ (n-type) GaAs	Light	1	7.86E-06	0.17
		100	1.27E-05	0.27
		10000	1.57E-05	0.33
	Dark	1	4.58E-08	0.0010
		100	2.04E-07	0.0043
		10000	2.04E-07	0.0043
2x10 ¹⁸ (n-type) GaAs	Light	1	6.68E-06	0.14
		100	1.55E-05	0.33
		10000	1.59E-05	0.34
	Dark	1	1.08E-06	0.023
		100	1.21E-06	0.026
		10000	1.24E-06	0.026
5x10 ¹⁸ (n-type) GaAs	Light	1	1.50E-06	0.032
		100	1.26E-05	0.27
		10000	1.63E-05	0.35
	Dark	1	1.94E-07	0.0041
		100	2.05E-06	0.043
		10000	3.17E-06	0.067
10 ¹⁸ (p-type) GaAs	Light	1	1.13E-06	0.024
		100	1.35E-05	0.29
		10000	1.08E-04	2.29
	Dark	1	3.21E-07	0.0068
		100	4.60E-06	0.10
		10000	2.31E-05	0.49
4x10 ¹⁹ (p-type) GaAs	Light	1	9.83E-07	0.021
		100	6.38E-06	0.14
		10000	1.50E-04	3.18
	Dark	1	4.03E-07	0.0085
		100	5.81E-06	0.12
		10000	2.92E-04	6.18

4.4. Impedance measurements

As already mentioned, the flat band potential V_{fb} , the position of the band edges at the semiconductor surface, and the free charge carrier concentration at the surface at a given voltage are important quantities in semiconductor electrochemistry. The common method to determine flat band potential is by the measurement of the capacity of the electric double layer. In this work, the Mott-Schottky equation

$$C_{sc}^{-2} = \left(\frac{2}{eN\epsilon\epsilon_0}\right)\left(V - V_{fb} - \frac{kT}{e}\right) \quad \text{for n-type semiconductor} \quad (4.5a)$$

$$C_{sc}^{-2} = -\left(\frac{2}{eN\epsilon\epsilon_0}\right)\left(V - V_{fb} - \frac{kT}{e}\right) \quad \text{for p-type semiconductor} \quad (4.5b)$$

based upon the simplest equivalent circuit was used to obtain the flat band potential. On the basis of this relationship, the value of kT/e is too small to be attributed to the capacitance. It can be neglected and thus the flat band potential, V_{fb} can be determined from V_0 , the point of intersection of a C_{sc}^{-2} with the abscissa

$$V_{fb} = V_0 \quad (4.6)$$

The surface doping density N can be obtained from the slope of the plot

$$N = \frac{2}{\epsilon \cdot \epsilon_0 \cdot e \cdot \text{slope}} \quad (4.7)$$

Impedance techniques were applied to measure capacitance C_{sc} . An a.c. generator/analyzer is used in impedance measurements to provide a voltage signal to analyze current and voltage outputs. A small a.c. voltage of less than kT/e (<0.026) is superimposed on the d.c. input voltage, since the absolute value of the interface impedance can be obtained at a given frequency. The validity of the Mott-Schottky analysis is based on the assumption that the capacitance of the space charge layer is much less than that of the Helmholtz layer. Actually, the equivalent circuit for impedance analysis of semiconductor electrodes is very complex since it consists of a space charge layer inside the semiconductor and one in the electrolyte (Gouy layer) as well as a double layer (Helmholtz layer). This results in an equivalent circuit with several capacitors and resistors [Memming, 1964]. At high frequency, the contribution of Helmholtz and Gouy capacitance can be negligible. Thus one constant resistor and one constant capacitor can be assumed only when impedance measurements are made over a certain frequency range. The equivalent circuit of the interface between the semiconductor and electrolyte can be reduced to a simple one.

The potential for the impedance tests should be chosen in the range where there is no or little product formed on the semiconductor surface. As described before, the thickness of As formed on the surface of p-GaAs increased with increasing potential in the anodic region. Therefore, the potentials selected for p-GaAs impedance tests were in very small ranges just above corrosion potentials to eliminate the effects of products formed on the surface. For n-GaAs this was not a problem. However, the potential ranges for impedance tests were also small and not far from the corrosion potential.

The measured results are presented below and in Figs. 4.39-4.46 and Table 4.6. The well-known linear relationship between C_s^{-2} and the applied voltage V at given frequency f (Mott-Schottky relationship) is evident.

4.4.1. *n*-type GaAs

The Mott-Schottky plots for n-GaAs both in phosphoric acid and deionized water are shown in Figs. 4.39-4.42. All test potentials were taken in the active region based on the polarization curves. Results from samples tested in the dark and daylight were superimposed together for comparison. A trend line was applied and the equation is displayed on the chart. The flat band potentials obtained from the charts and the surface doping densities calculated according to Eq. 4.7 are summarized in Table 4.5. It is clear that all the plots are almost straight lines and slope upwards and to the right with increasing potentials. Trend lines for samples tested in the dark are above those tested in daylight. Since the slopes are close, the absolute value of the flat band potential is larger for samples tested in the dark compared with those tested in daylight.

4.4.2. *p*-type GaAs

These plots were drawn as for n-GaAs and are shown in Figs. 4.43-4.46. The plots slope downwards and to the right with increasing potentials. The plots for samples tested in the dark are also above those in daylight at low potential, however, due to the large differences in slopes, the flat band potential is smaller for samples tested in the dark than in daylight. Unlike n-GaAs, whose flat band potentials were negative, the flat band potentials for p-GaAs are positive. The flat band potentials and surface doping densities are also summarized in Table 4.6.

The measured flat band potentials in the dark are more negative than those in daylight; the values attained in deionized water are also smaller than those in phosphoric acid. The flat band potential for GaAs with a higher doping density is more positive than that with a lower doping density. For measured surface doping densities, all results are in

good agreement with the original value except for p-GaAs ($4 \times 10^{19} \text{cm}^{-3}$) in deionized water; its density is lower than expected.

Table 4.6. Flat band potentials and surface doping densities for GaAs electrodes.

GaAs	Doping Level (cm^{-3})	28.5% H_3PO_4				Deionized Water			
		Light		Dark		Light		Dark	
		$N_{D/A}$ ($\times 10^{18}$)	V_{fb} (V)	$N_{D/A}$ ($\times 10^{18}$)	V_{fb} (V)	$N_{D/A}$ ($\times 10^{18}$)	V_{fb} (V)	$N_{D/A}$ ($\times 10^{18}$)	V_{fb} (V)
n-type	10^{18}	0.92	-1.28	1.02	-1.71	0.94	-1.57	1.04	-2.04
	2×10^{18}	2.46	-1.24	2.25	-1.28	1.95	-1.32	2.64	-1.80
p-type	10^{18}	1.06	1.16	0.72	0.84	1.66	0.98	0.95	0.57
	4×10^{19}	31.8	1.24	28.4	1.14	17.41	1.17	10.58	1.02

Note: Units for N are cm^{-3} .

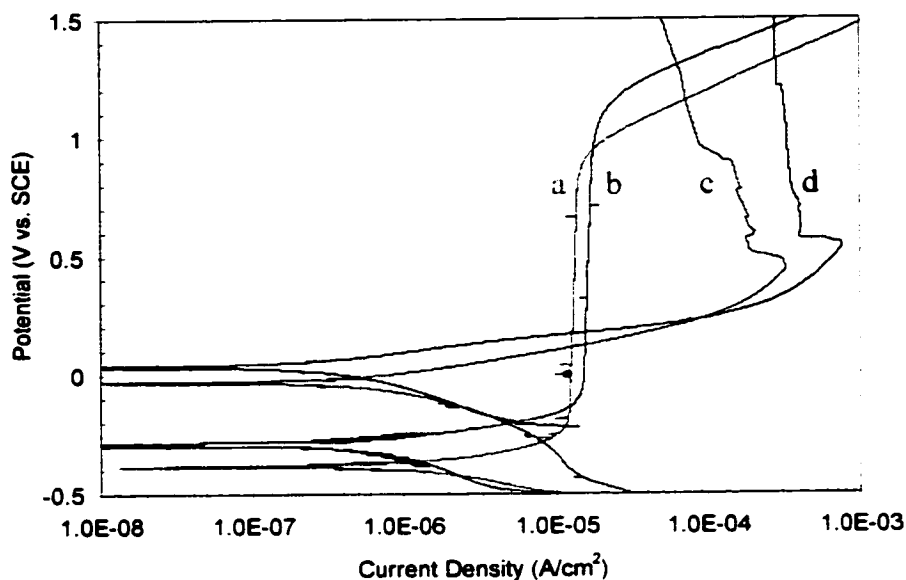


Figure 4.1. Polarization curves for GaAs in 1% HF (a and c) and 28.5% H_3PO_4 (b and d) under illumination: a) and b) n-GaAs, 10^{18}cm^{-3} ; c) and d) p-GaAs, 10^{18}cm^{-3} .

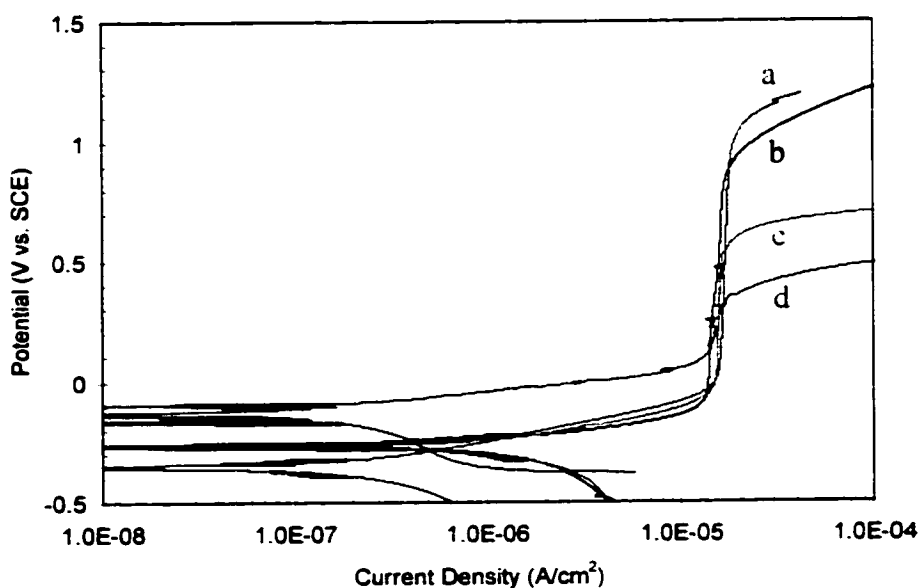


Figure 4.2. Polarization curves for n-type GaAs with various doping densities in 28.5% H_3PO_4 under illumination: a) 10^{17}cm^{-3} ; b) 10^{18}cm^{-3} ; c) $2 \times 10^{18}\text{cm}^{-3}$ and d) $5 \times 10^{18}\text{cm}^{-3}$.

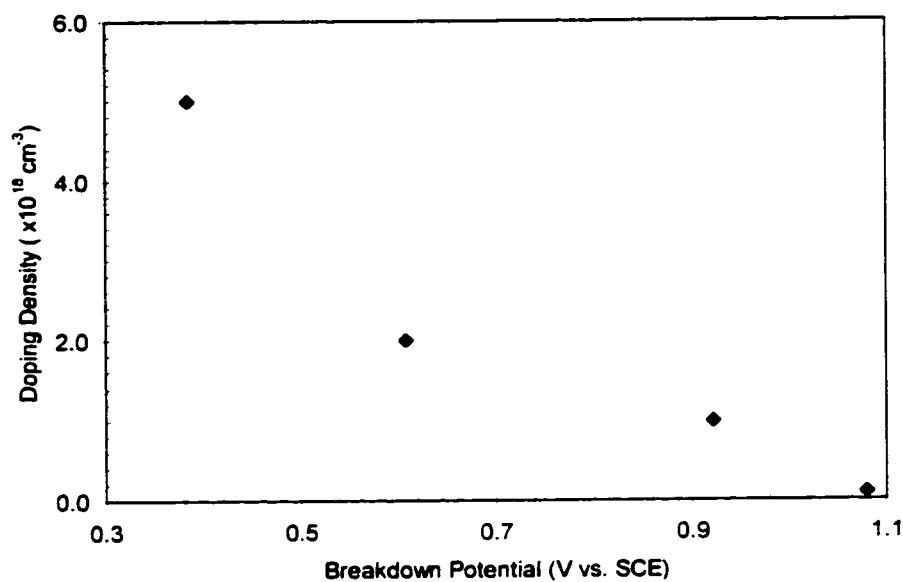


Figure 4.3. Breakdown potential for n-GaAs as a function of doping density in phosphoric acid under illumination.

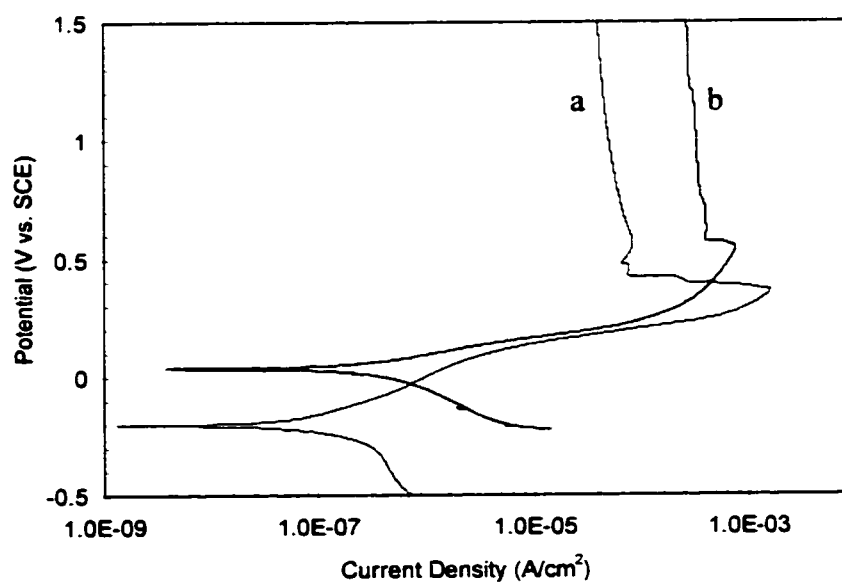


Figure 4.4. Polarization curves of p-type GaAs with various doping densities in 28.5% H_3PO_4 under illumination: a) $4 \times 10^{19} \text{ cm}^{-3}$ and b) 10^{18} cm^{-3} .

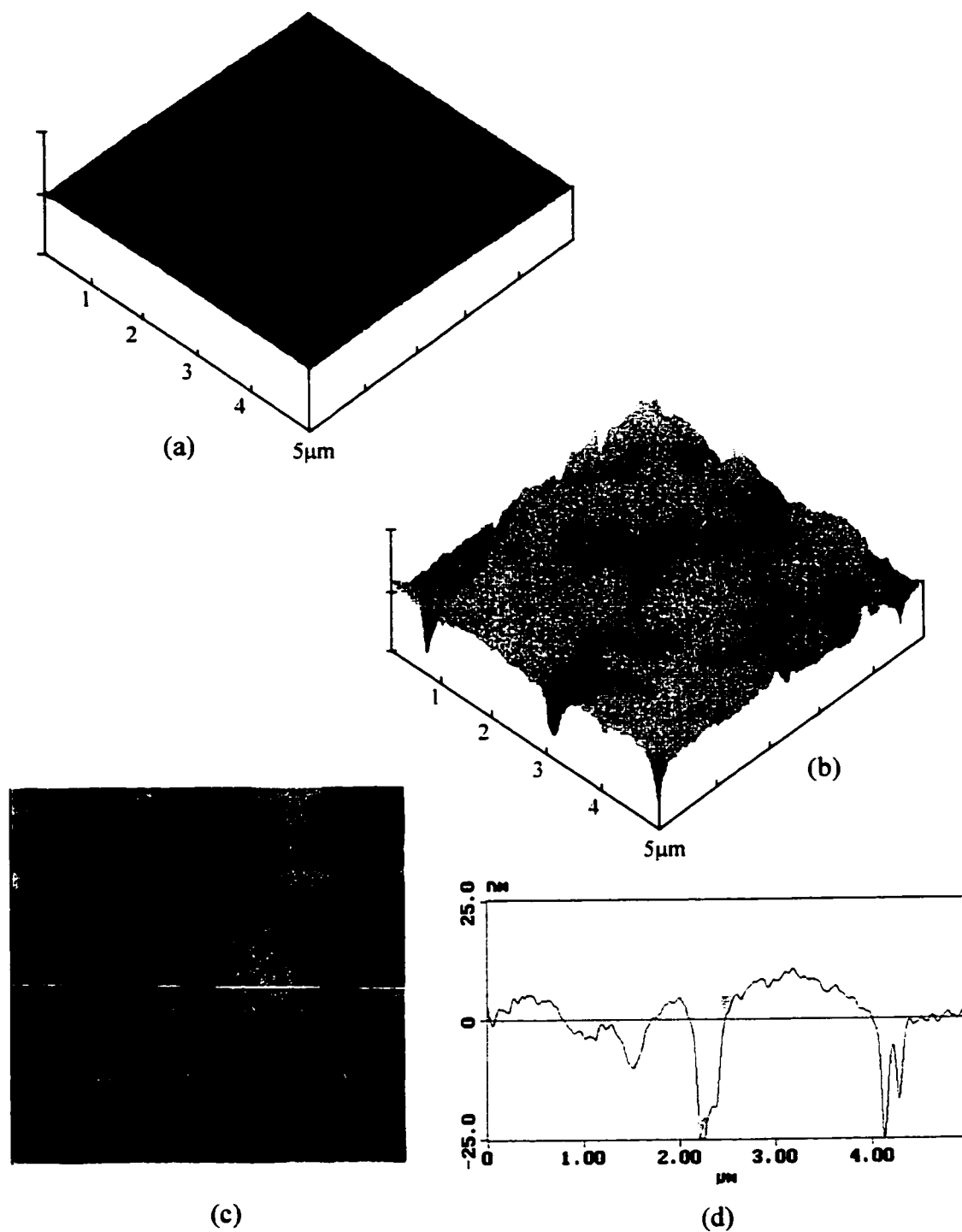


Figure 4.5. AFM image from n-GaAs ($2 \times 10^{18} \text{cm}^{-3}$) sample in phosphoric acid: a) before testing; b) polarized to 1.5 V in daylight; c) roughness analysis from (b); d) section analysis from (c).

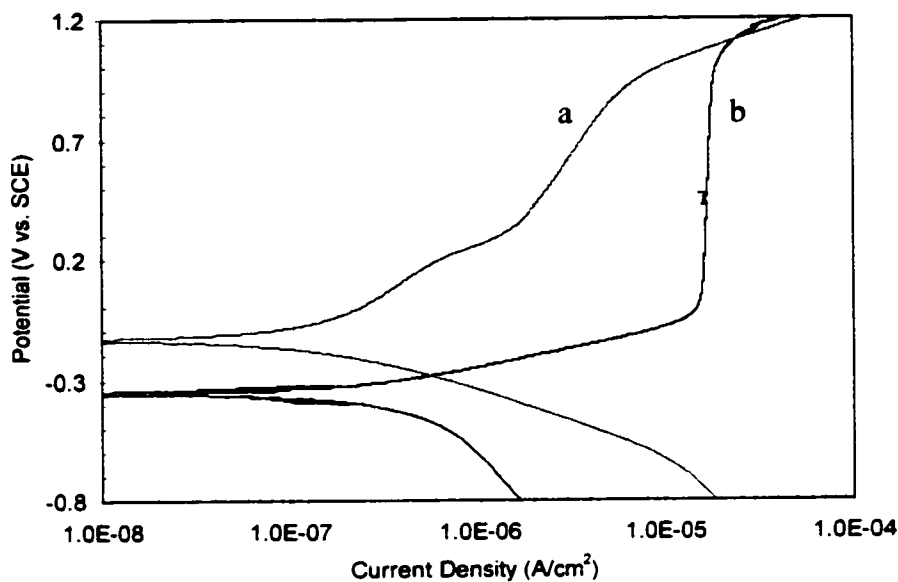


Figure 4.6. Polarization curves for n-GaAs (10^{17} cm^{-3}) in 28.5% H_3PO_4 in the dark (a) and daylight (b).

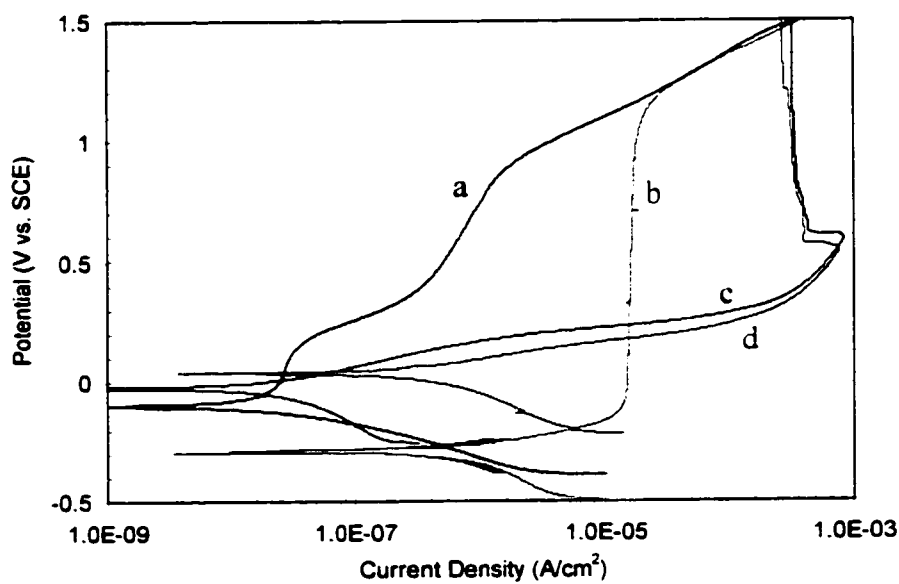


Figure 4.7. Polarization curves for n- (a and b) and p-GaAs (c and d) (10^{18} cm^{-3}) tested in 28.5% H_3PO_4 under illumination (b and d) and in the dark (a and c).

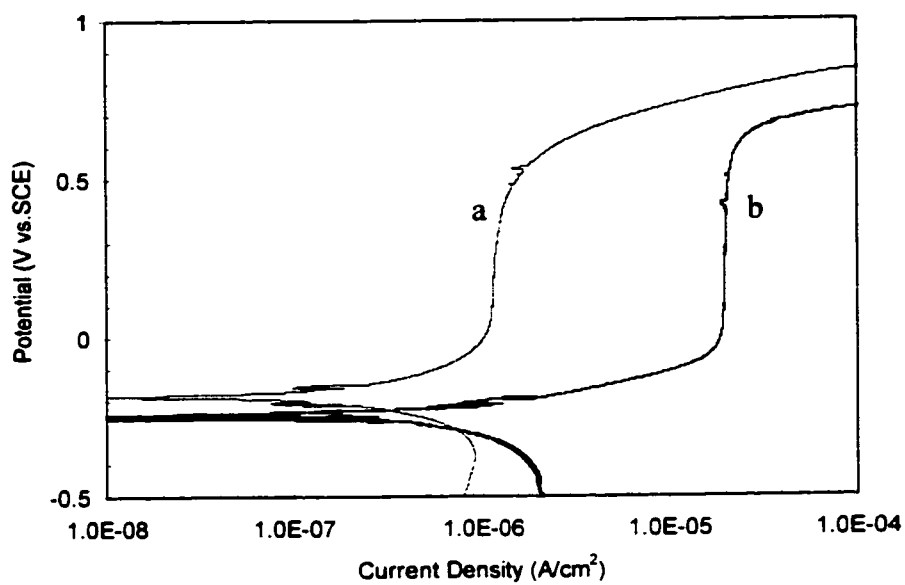


Figure 4.8. Polarization curves for n-GaAs ($2 \times 10^{18} \text{ cm}^{-3}$) in 28.5% H_3PO_4 in the dark (a) and daylight (b).

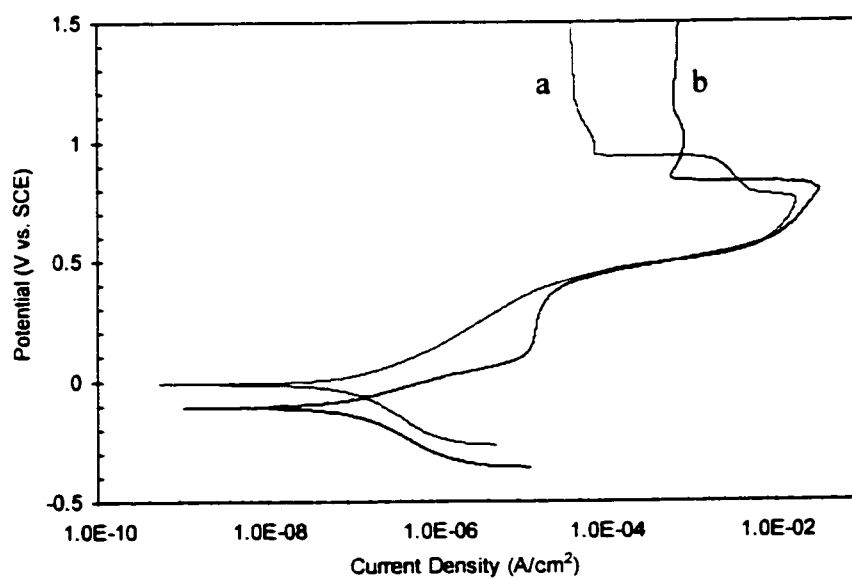


Figure 4.9. Polarization curves for n-GaAs ($5 \times 10^{18} \text{ cm}^{-3}$) in 28.5% H_3PO_4 in the dark (a) and daylight (b).

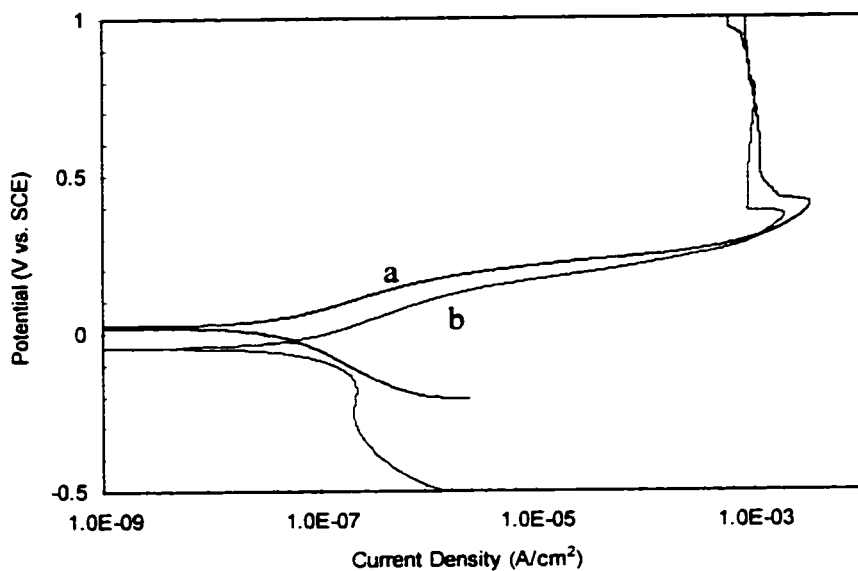


Figure 4.10. Polarization curves for p-GaAs ($4 \times 10^{19} \text{ cm}^{-3}$) in 28.5% H_3PO_4 in daylight (a) and dark (b).

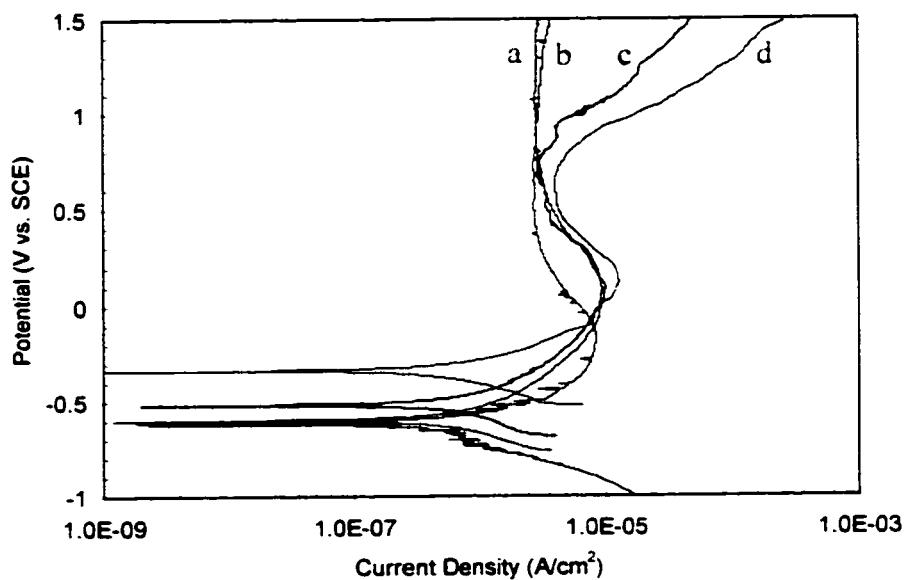


Figure 4.11. Polarization curves for n-type GaAs with various doping densities in deionized water under illumination: a) 10^{18} cm^{-3} ; b) 10^{17} cm^{-3} ; c) $2 \times 10^{18} \text{ cm}^{-3}$ and d) $5 \times 10^{18} \text{ cm}^{-3}$.

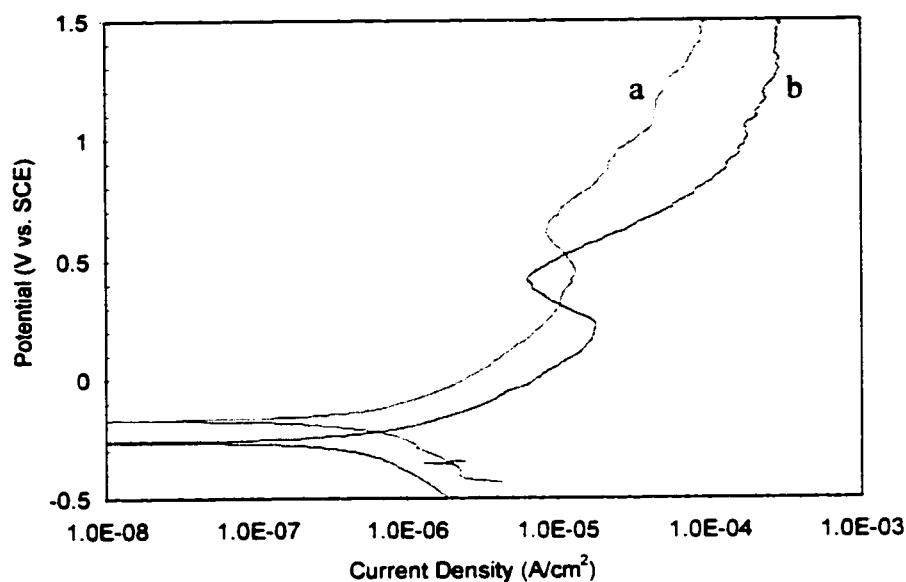


Figure 4.12. Polarization curves for p-type GaAs with various doping densities in deionized water under illumination: a) 10^{18} cm^{-3} and b) $4 \times 10^{19} \text{ cm}^{-3}$.

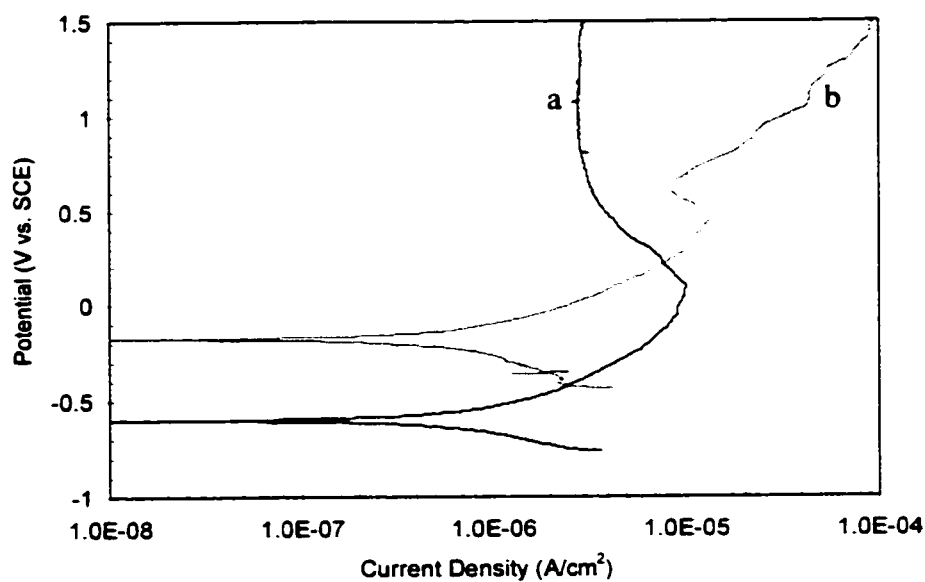


Figure 4.13. Polarization curves for GaAs (10^{18} cm^{-3}) in deionized water under illumination: a) n-type and b) p-type.

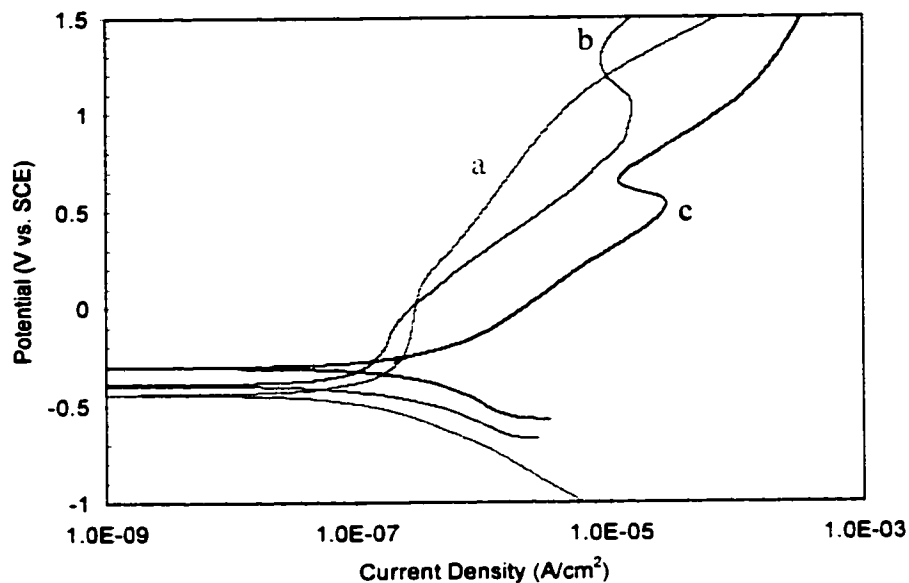


Figure 4.14. Polarization curves for n-type GaAs with various doping densities in deionized water in the dark: a) 10^{18} cm^{-3} ; b) $2 \times 10^{18} \text{ cm}^{-3}$ and c) $5 \times 10^{18} \text{ cm}^{-3}$.

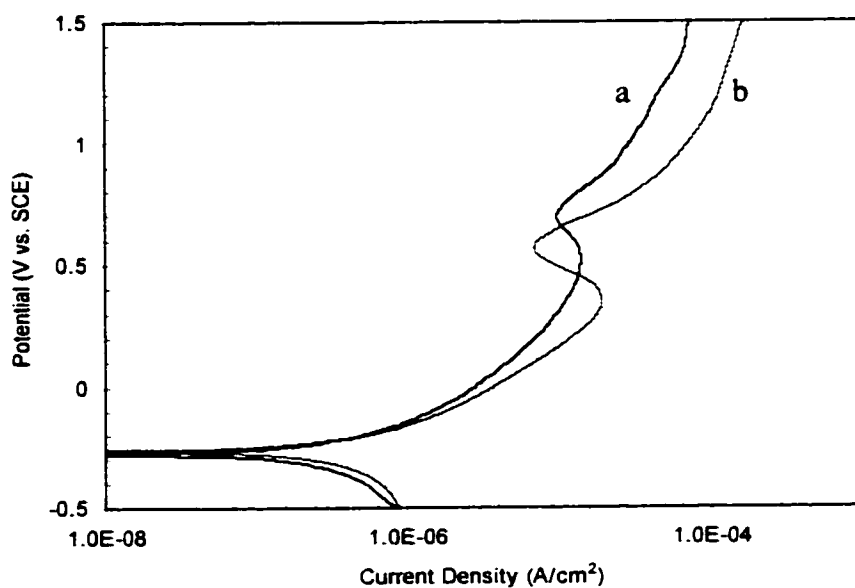


Figure 4.15. Polarization curves for p-type GaAs with various doping densities in deionized water in the dark: a) $4 \times 10^{19} \text{ cm}^{-3}$ and b) 10^{18} cm^{-3} .

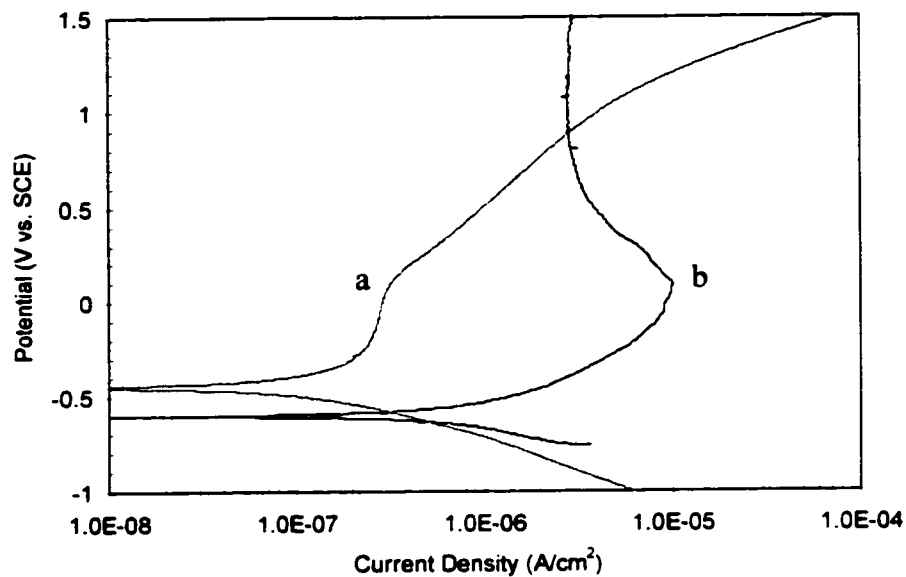


Figure 4.16. Polarization curves for n- GaAs (10^{18}cm^{-3}) in deionized water in the dark (a) and daylight (b).

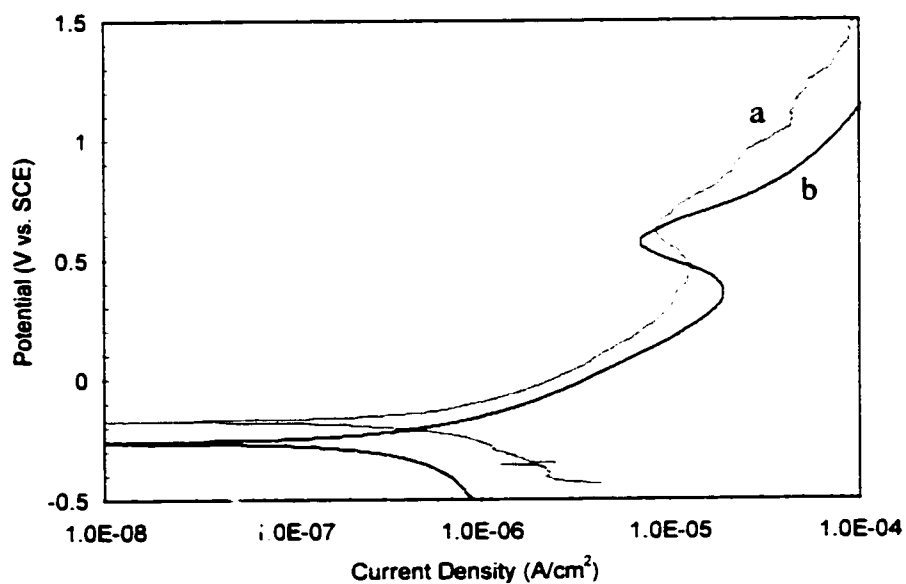


Figure 4.17. Polarization curves for p- GaAs (10^{18}cm^{-3}) in deionized water in daylight (a) and dark (b).

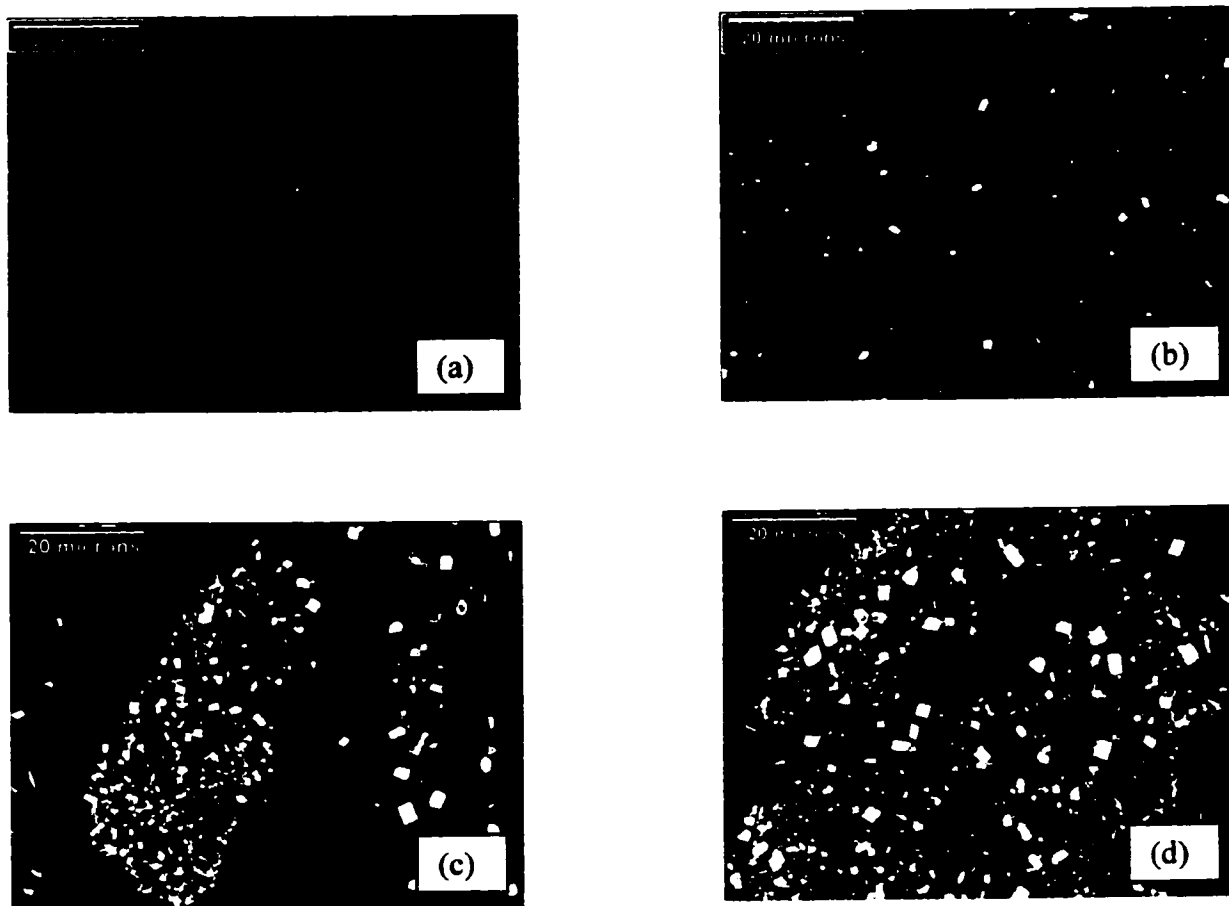
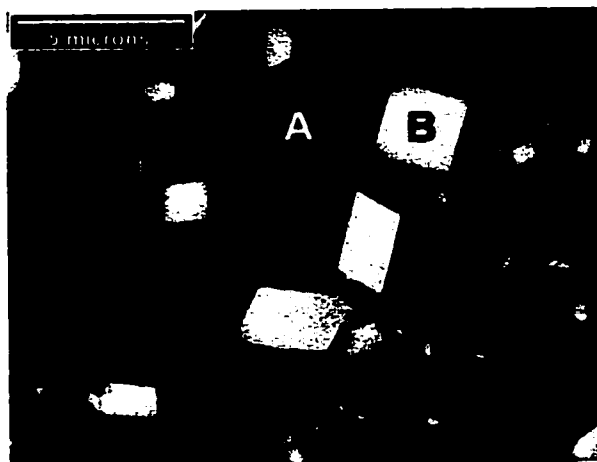
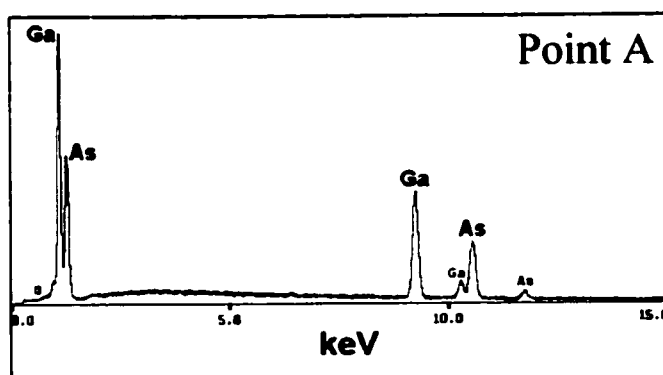


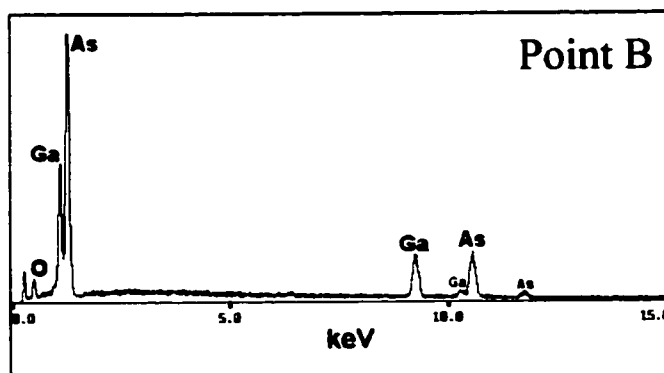
Figure 4.18. SEM micrographs of the surface morphology of n-GaAs, doping $1 \times 10^{17} \text{ cm}^{-3}$: (a) immediately, (b) 4 days, (c) 7 days and (d) 17 days after polarized at 0.75 V vs. SCE for 2 hours in 28.5% H_3PO_4 .



(a)



(b)



(c)

Figure 4.19. (a) SEM image of the same sample shown in Fig. 4.18d, along with EDX spectra of substrate (b) and one of the particles (c).

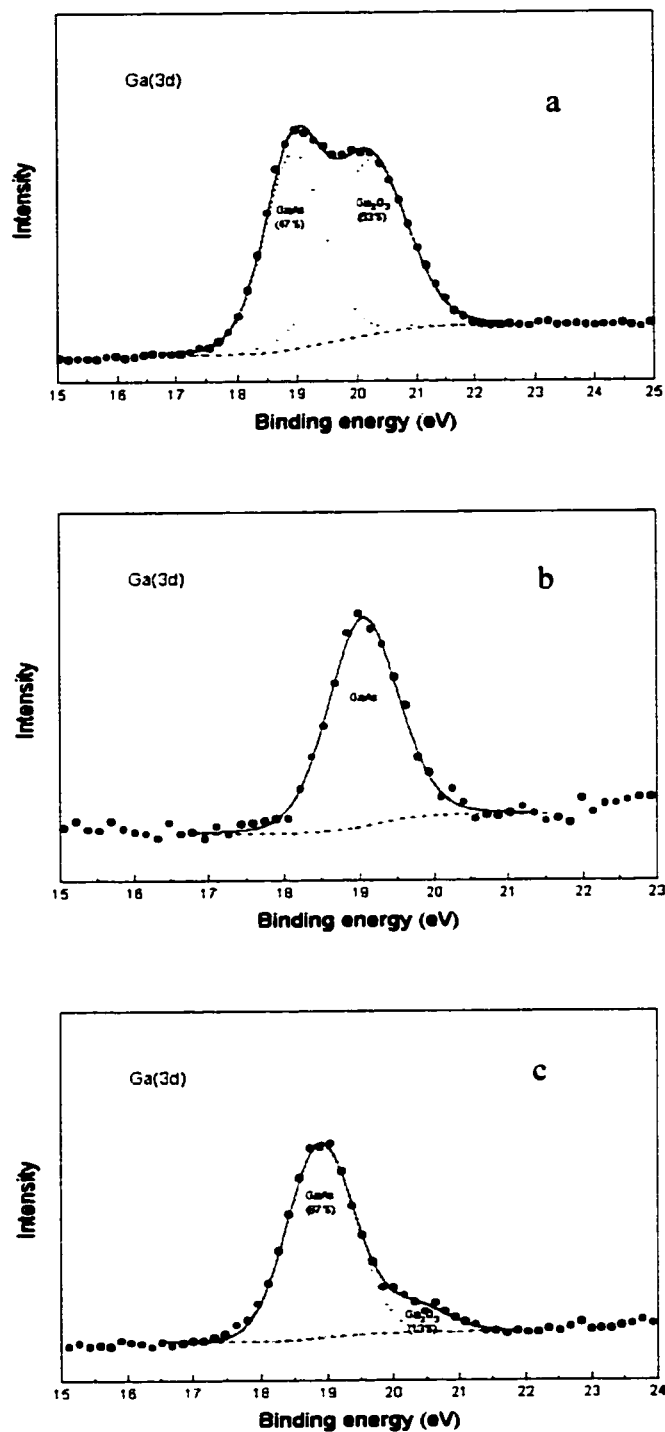


Figure 4.20. Ga 3d spectra for an as-received specimen (a), immediately after being polarized at 0.75V vs. SCE for 2 hours in 28.5% H_3PO_4 (b) and after exposure to air for one week (c).

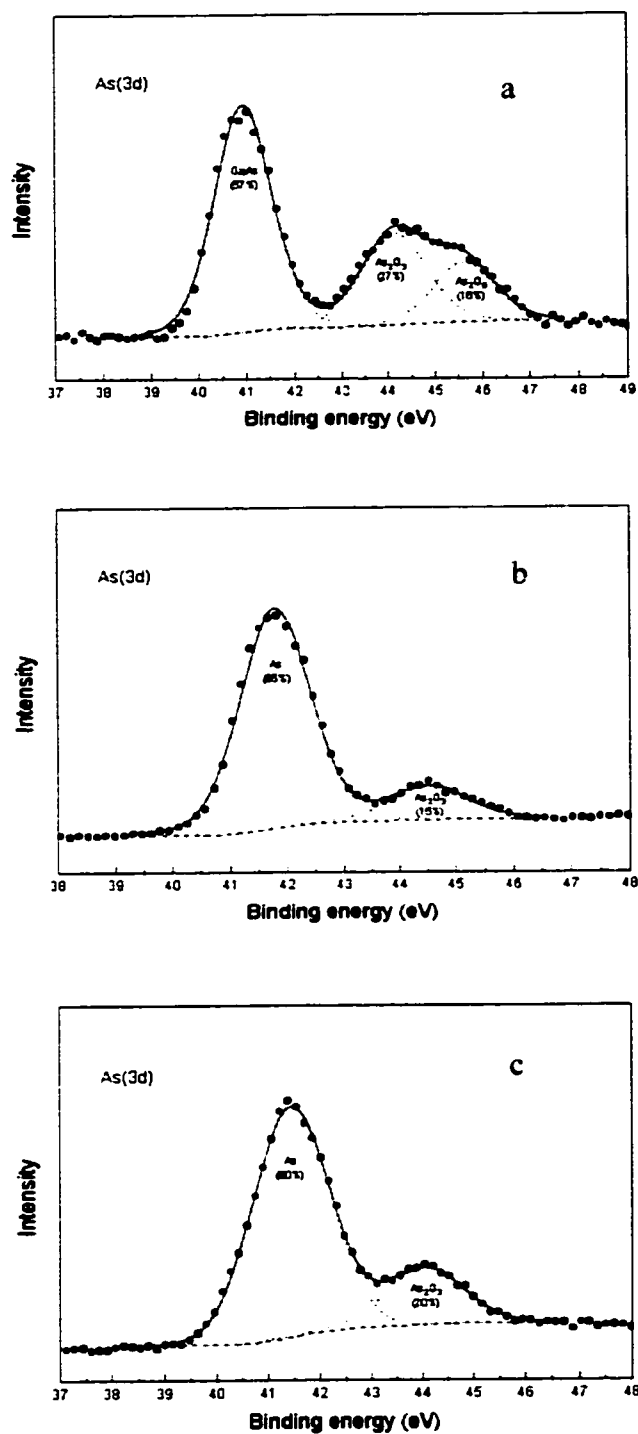


Figure 4.21. As 3d spectra for an as-received specimen (a), immediately after being polarized at 0.75V vs. SCE for 2 hours in 28.5% H₃PO₄ (b) and after exposure to air for one week (c).

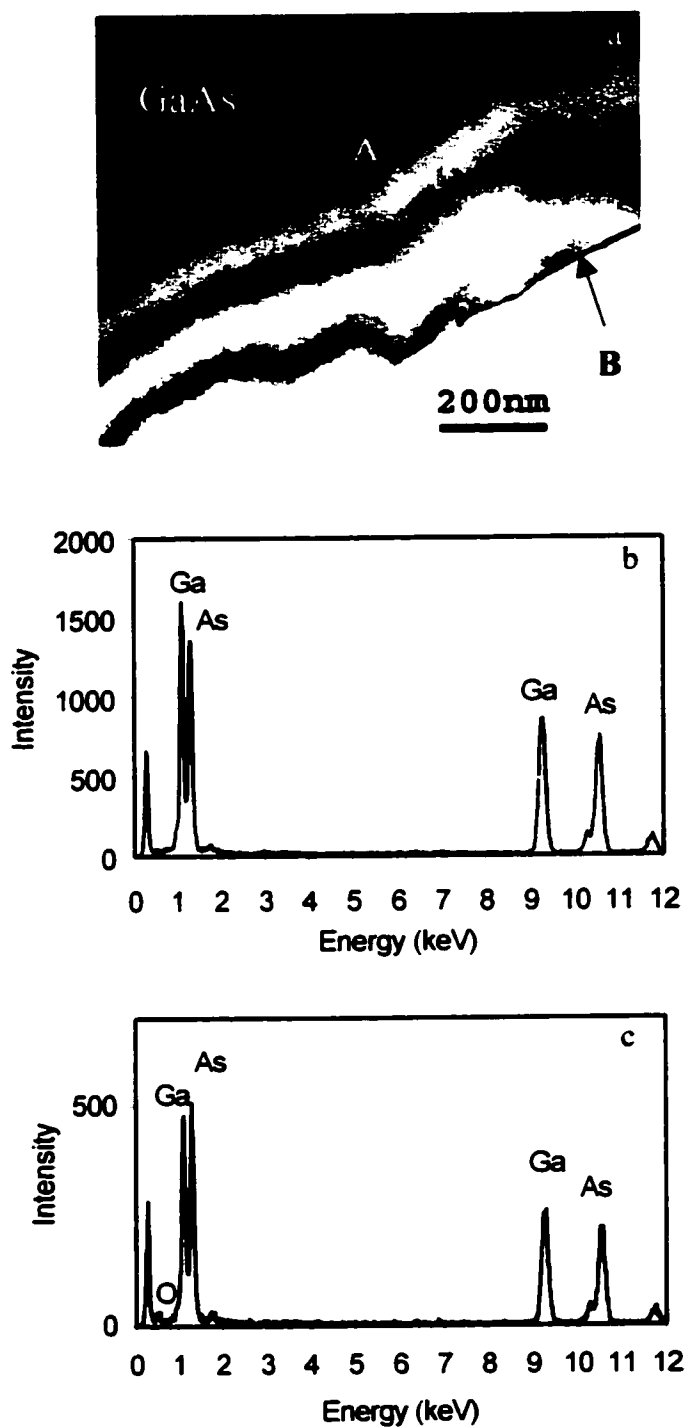


Figure 4.22. (a) TEM bright field image from n-GaAs ($2 \times 10^{18} \text{ cm}^{-3}$) sample polarized at -0.15 V in daylight; (b) EDX spectrum from bulk GaAs (point A) in (a); (c) EDX spectrum from surface region (point B) in (a).

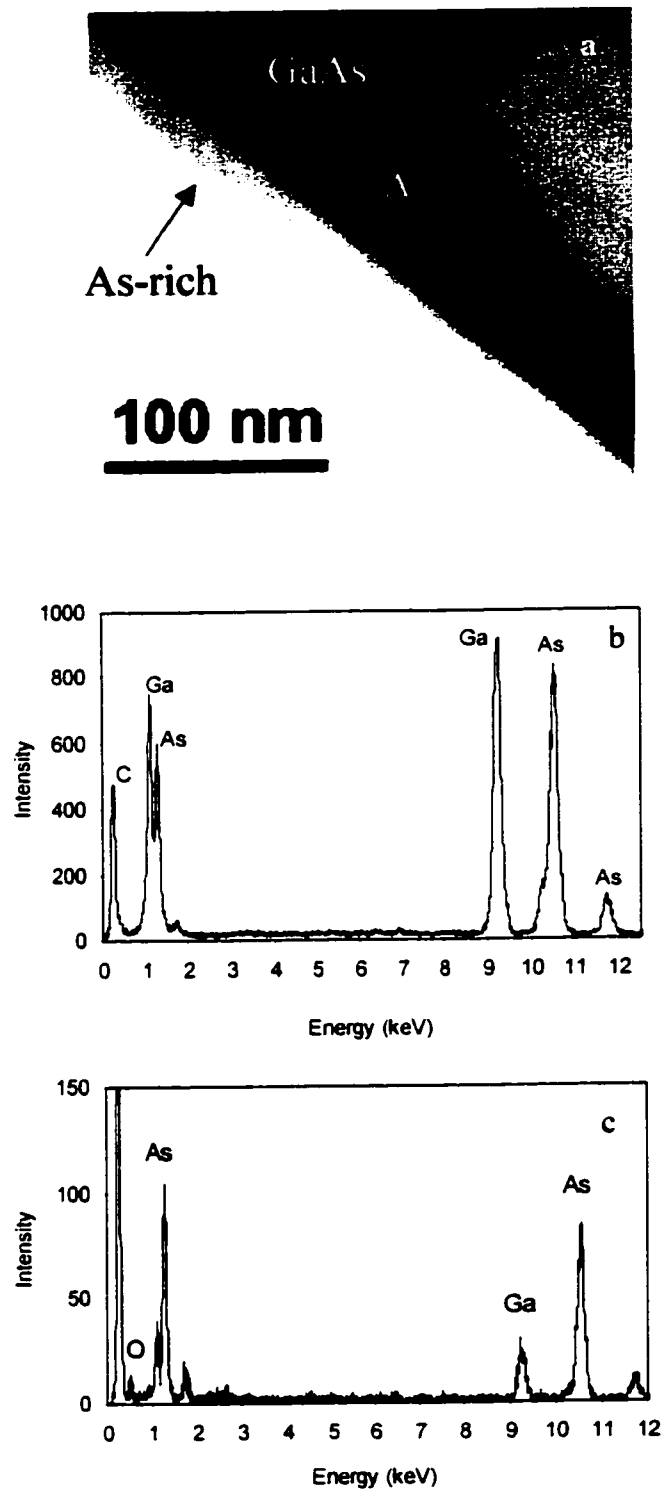


Figure 4.23. (a) TEM bright field image from an n-GaAs ($2 \times 10^{18} \text{ cm}^{-3}$) sample polarized at 0.4V in daylight; (b) EDX spectrum from bulk GaAs (point A) in (a); (c) EDX spectrum from surface region in (a).

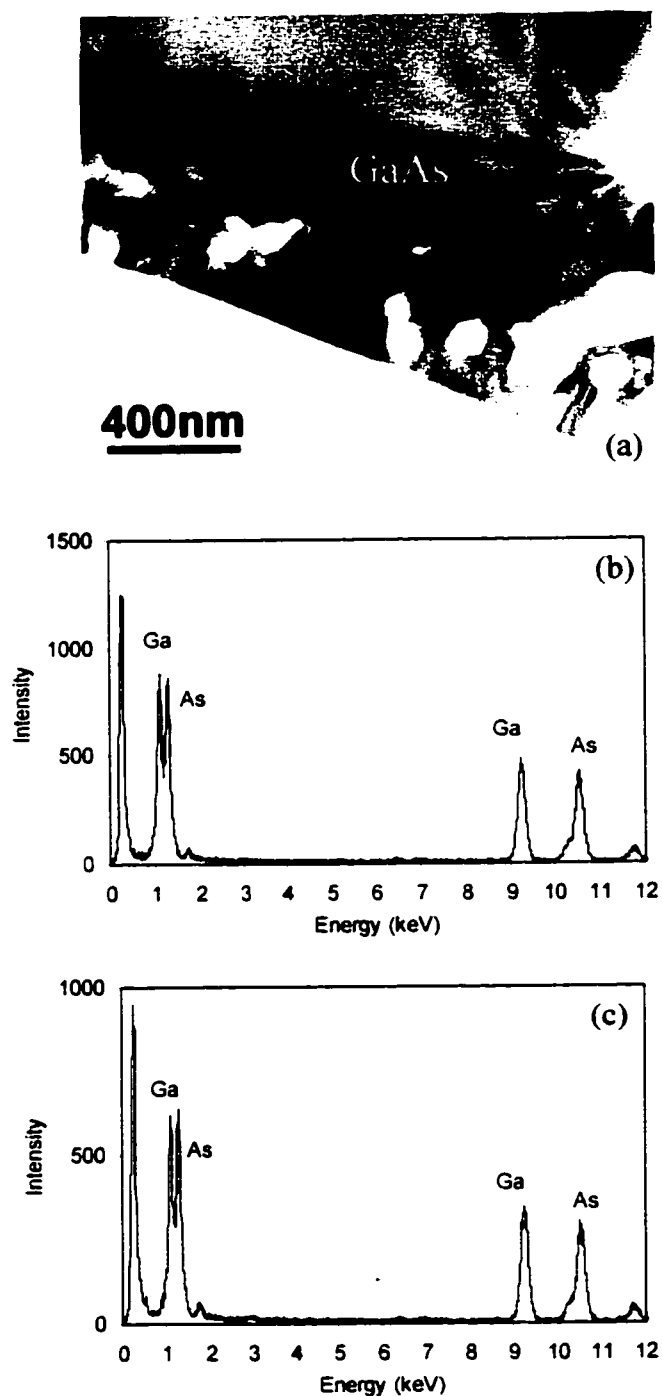


Figure 4.24. (a) TEM bright field image from an n-GaAs ($2 \times 10^{18} \text{ cm}^{-3}$) sample polarized at 0.75V in daylight; (b) EDX spectrum from bulk region in (a); (c) EDX spectrum from surface region in (a).

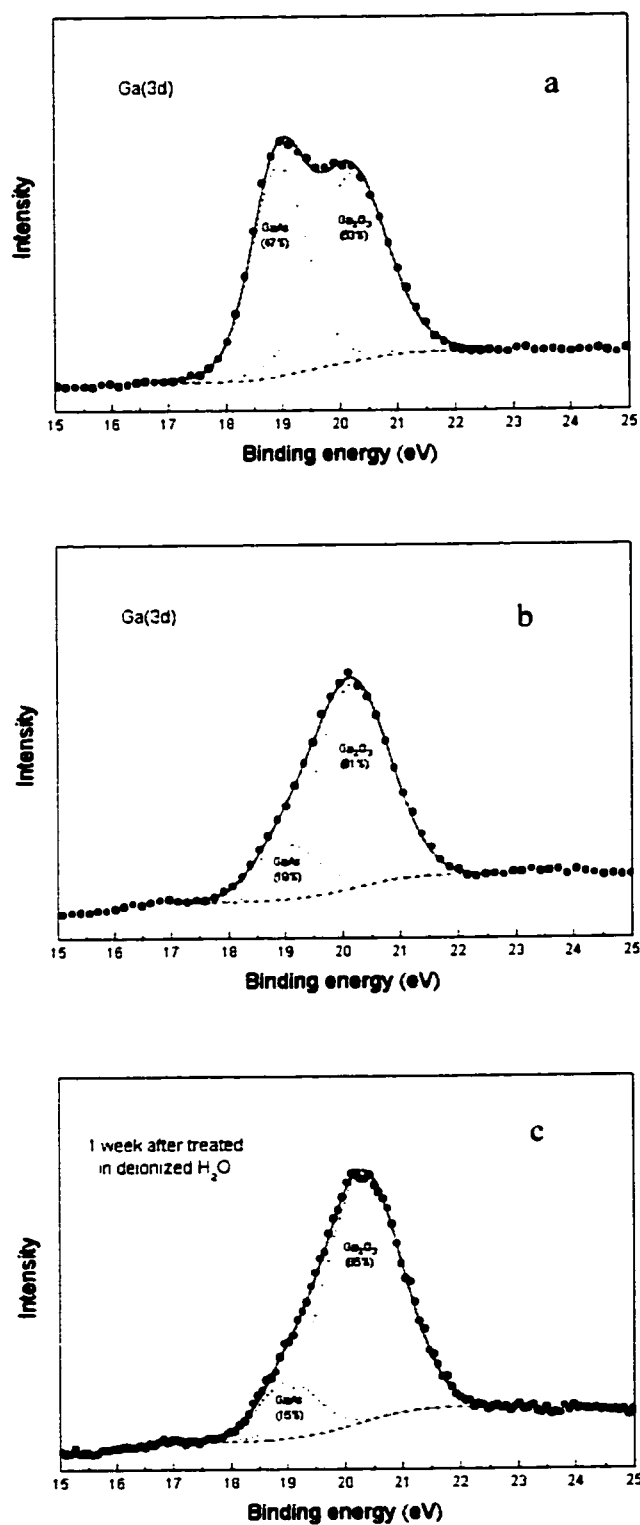


Figure 4.25. Ga 3d spectra for an as-received specimen (a), immediately after being polarized at 0.75V vs. SCE for 2 hours in deionized water (b) and after exposure to air for one week (c).

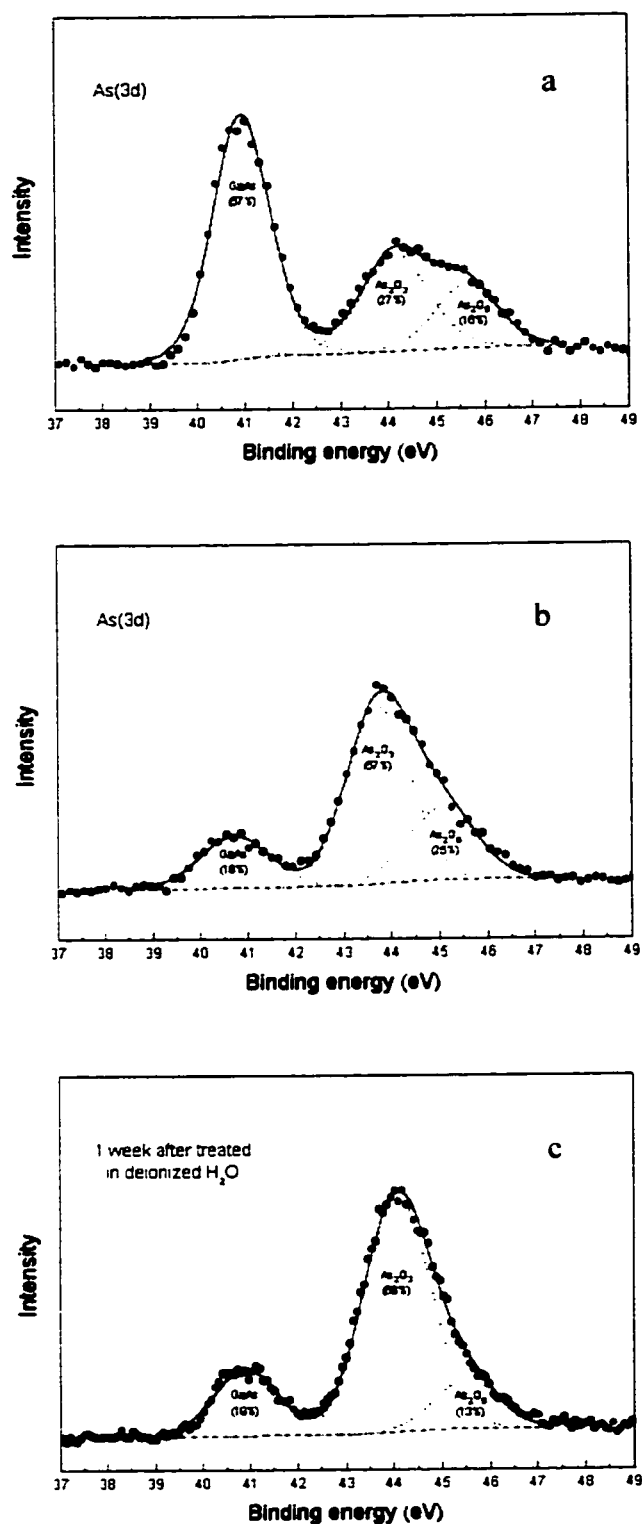


Figure 4.26. As 3d spectra for an as-received specimen (a), immediately after being polarized at 0.75V vs. SCE for 2 hours in deionized water (b) and after exposure to air for one week (c).

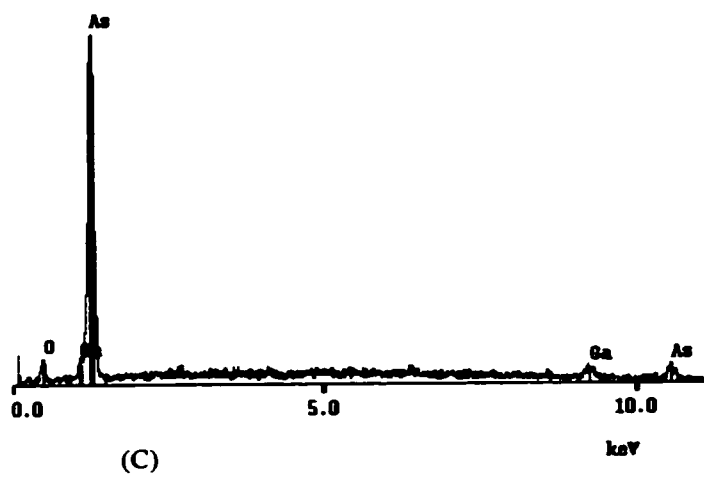
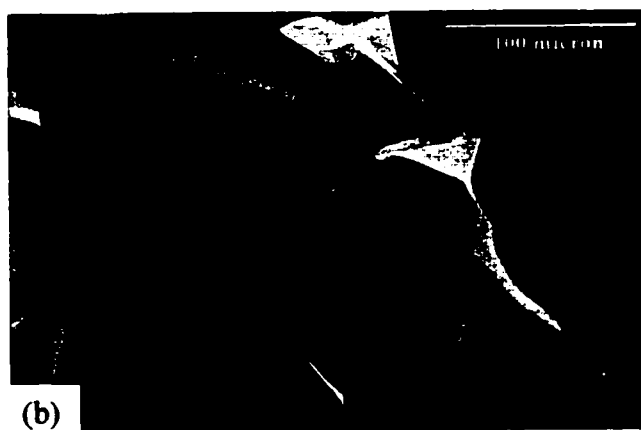


Figure 4.27. a) SEM images (a, b) from n-GaAs polarized at 7V for 2 h in phosphoric acid. Also shown is an EDX spectrum (c) from the faceted particle indicated in (b).

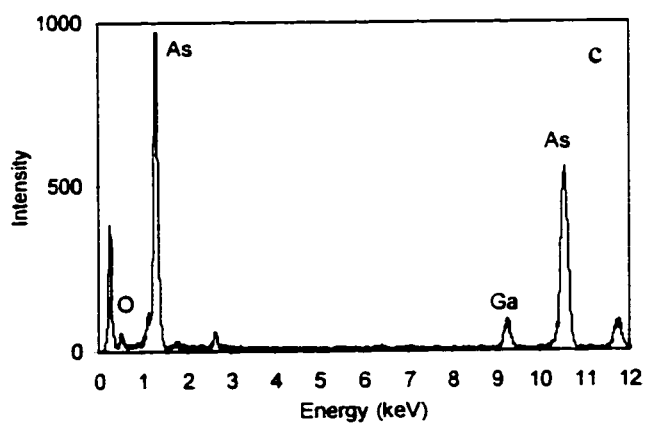
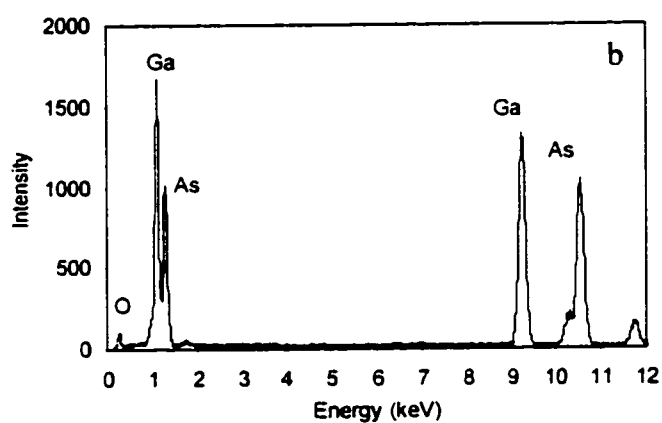
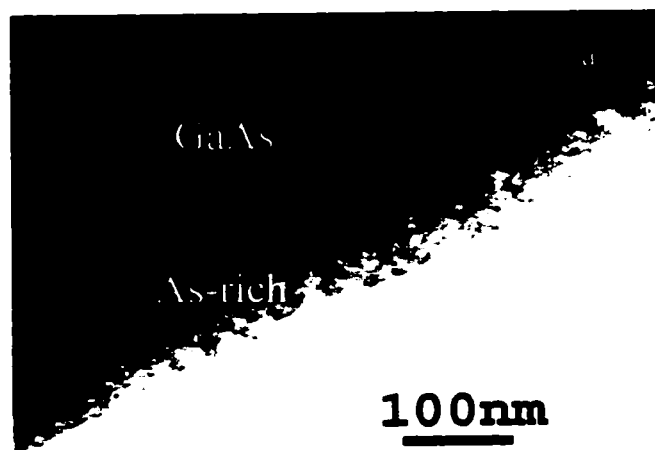


Figure 4.28. (a) TEM bright field image from a p-GaAs ($4 \times 10^{19} \text{ cm}^{-3}$) sample polarized at 0.15V in daylight; (b) EDX spectrum from bulk GaAs in (a); (c) EDX spectrum from surface layer in (a).

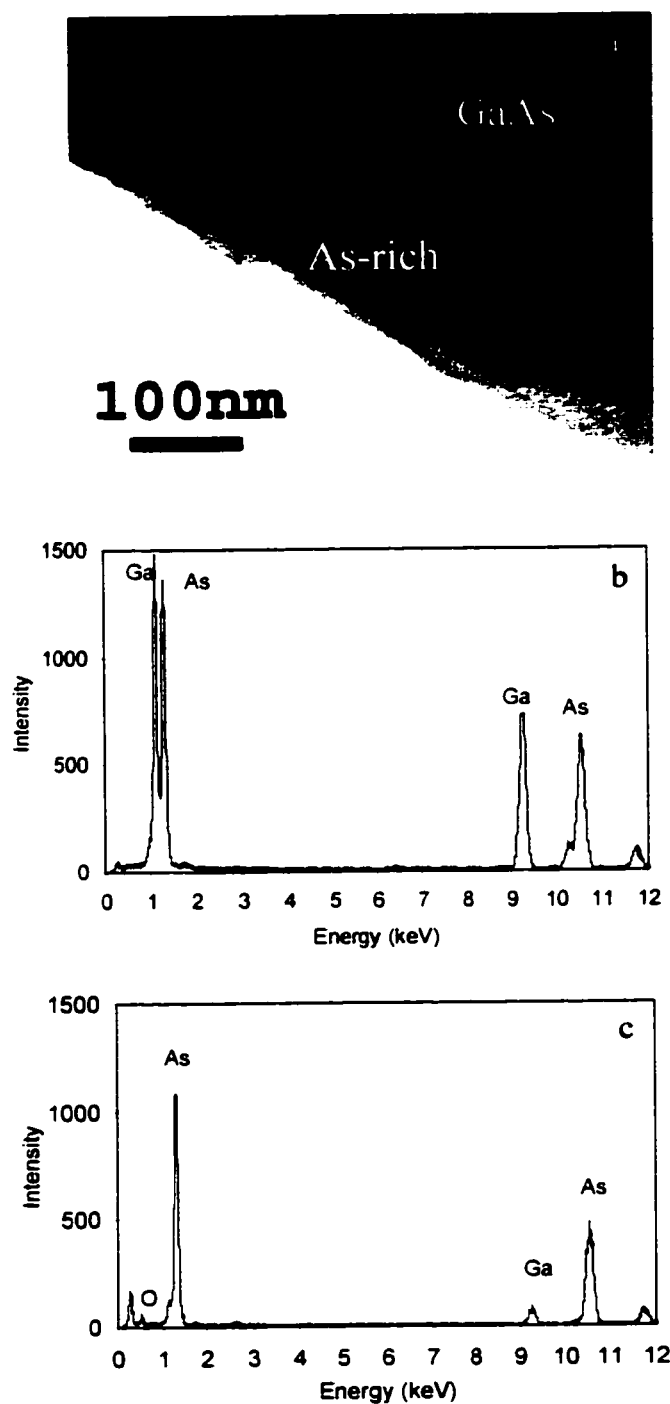


Figure 4.29. (a) TEM bright field image from a p-GaAs ($4 \times 10^{19} \text{ cm}^{-3}$) sample polarized at 0.4V in daylight; (b) EDX spectrum from bulk GaAs in (a); (c) EDX spectrum from surface layer in (a).

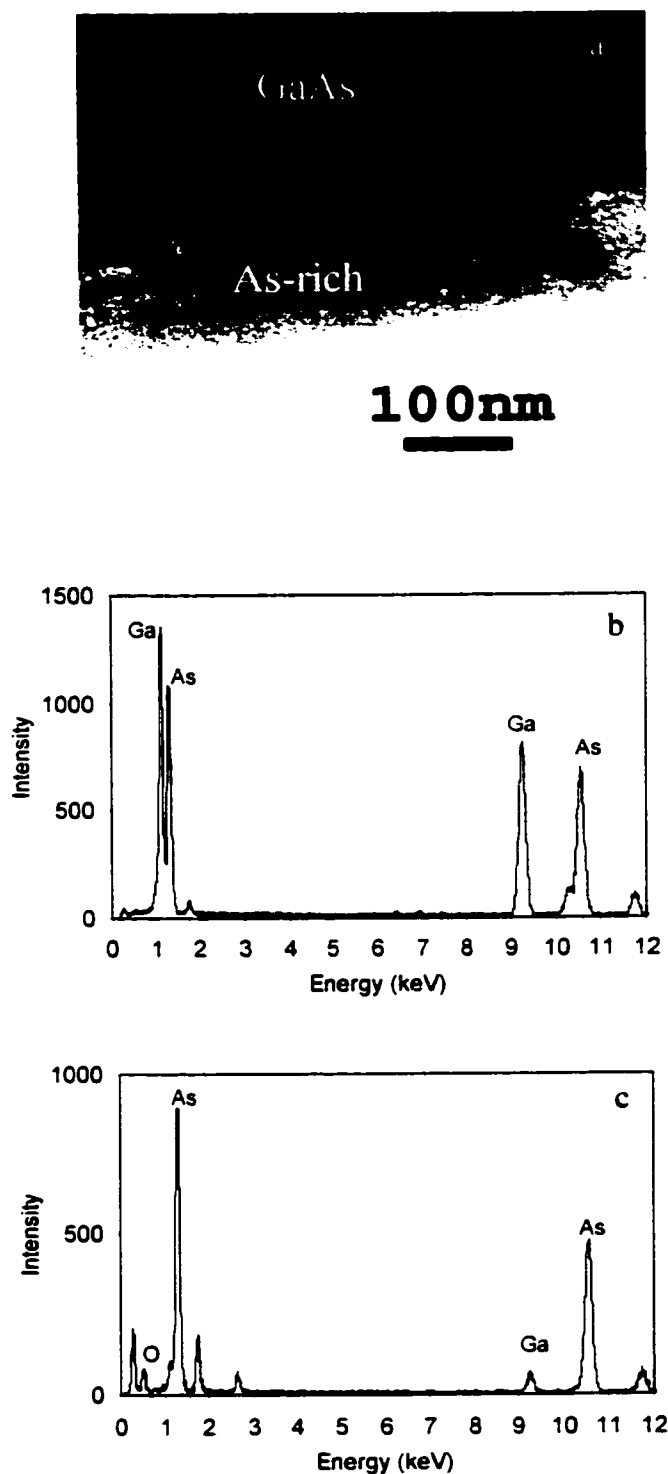


Figure 4.30. TEM bright field image from a p-GaAs ($4 \times 10^{19} \text{ cm}^{-3}$) sample polarized at 0.75V in daylight; (b) EDX spectrum from bulk GaAs in (a); (c) EDX spectrum from surface layer in (a).

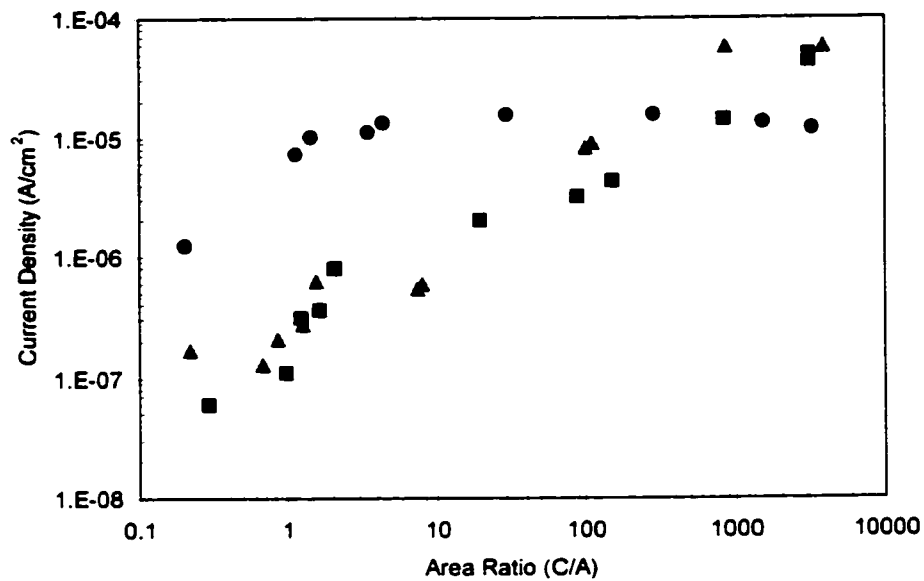


Figure 4.31. Galvanic current density vs C/A area ratio for n- and p-GaAs (● n-GaAs, 10^{18}cm^{-3} ; ■ p-GaAs, 10^{18}cm^{-3} and ▲ p-GaAs, $4 \times 10^{19}\text{cm}^{-3}$). All tests were done in daylight.

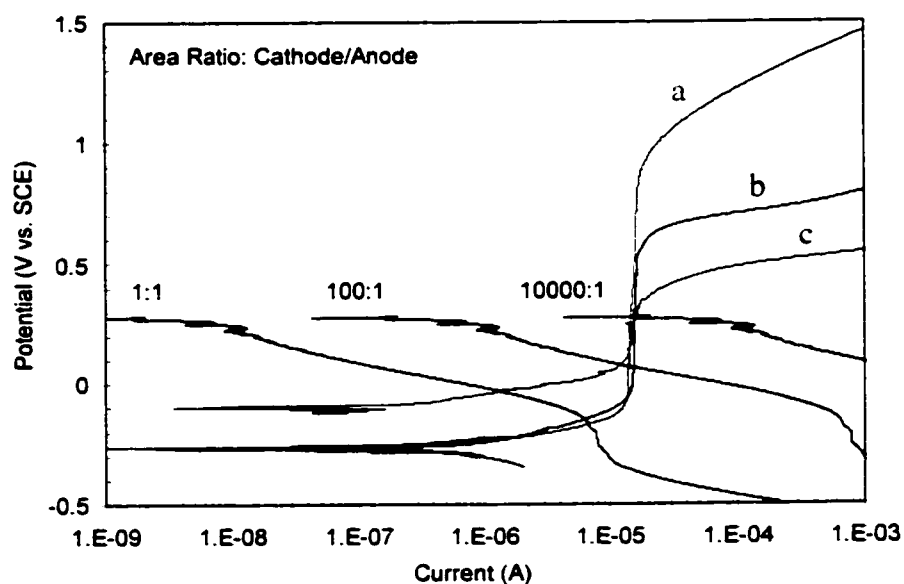


Figure 4.32. Superposition of anodic polarization curves for n-GaAs with cathodic polarization curves for Au: a) 10^{18}cm^{-3} , b) $2 \times 10^{18}\text{cm}^{-3}$ and c) $5 \times 10^{18}\text{cm}^{-3}$.

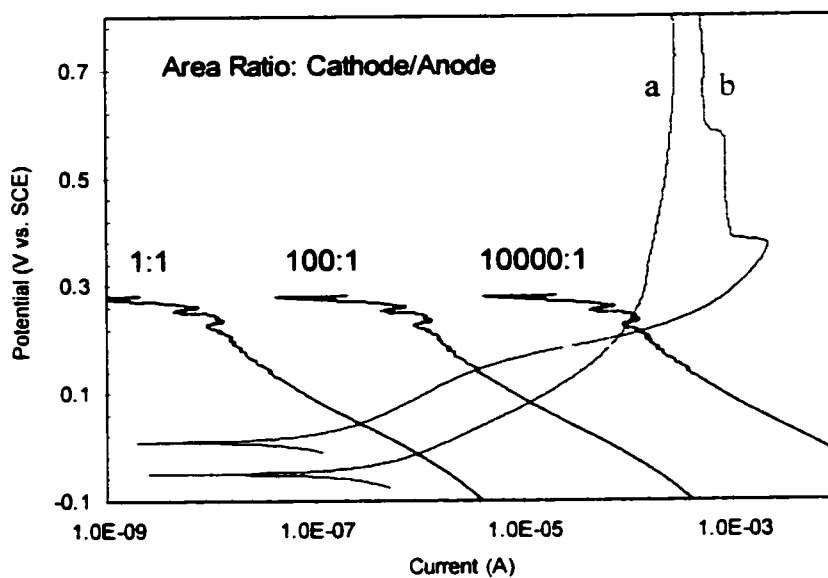


Figure 4.33. Superposition of anodic polarization curves for p-GaAs with cathodic polarization curves for Au: a) 10^{18} cm^{-3} and $4 \times 10^{19} \text{ cm}^{-3}$.

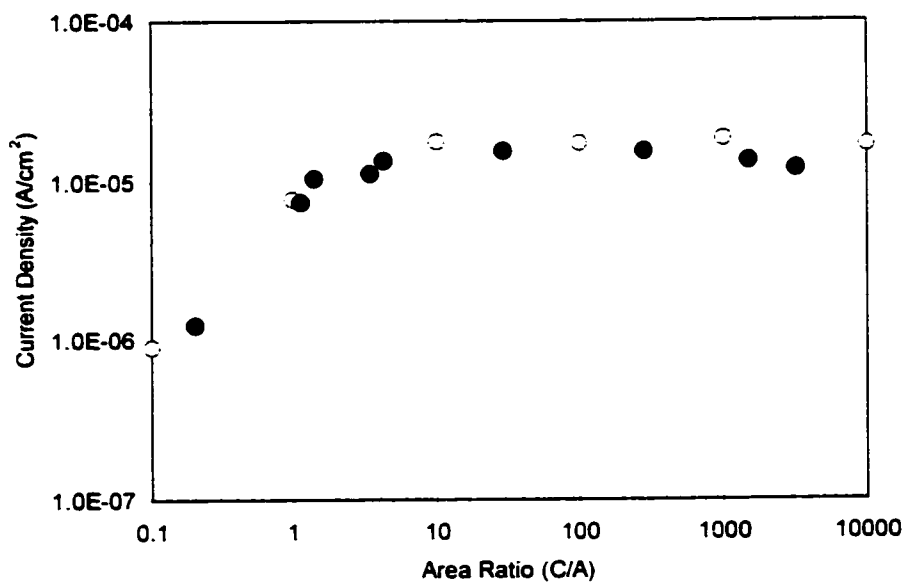


Figure 4.34. Comparison of galvanic current densities, obtained directly (●) and indirectly (○) for n-GaAs (10^{18} cm^{-3}).

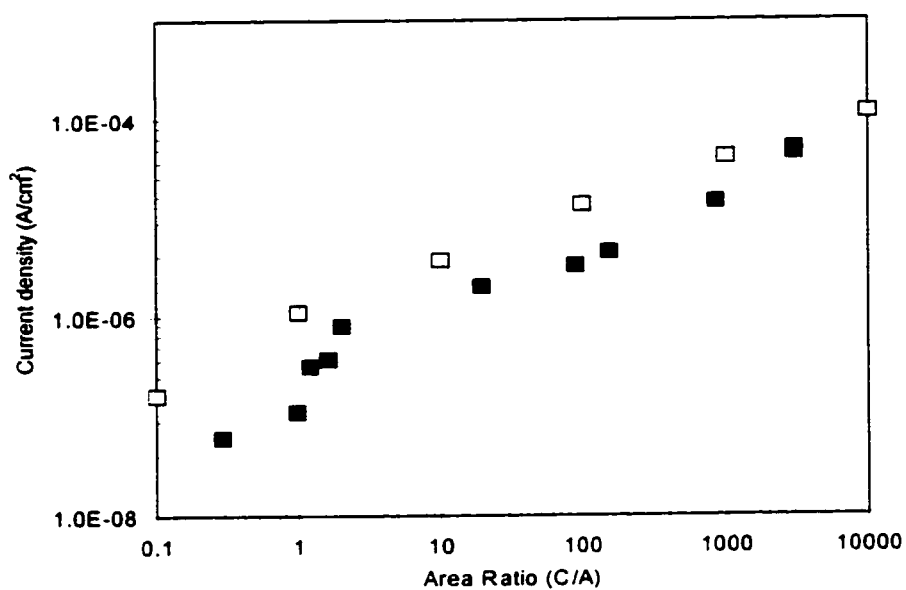


Figure 4.35. Comparison of galvanic current densities, obtained directly (■) and indirectly (□) for p-GaAs (10^{18}cm^{-3}).

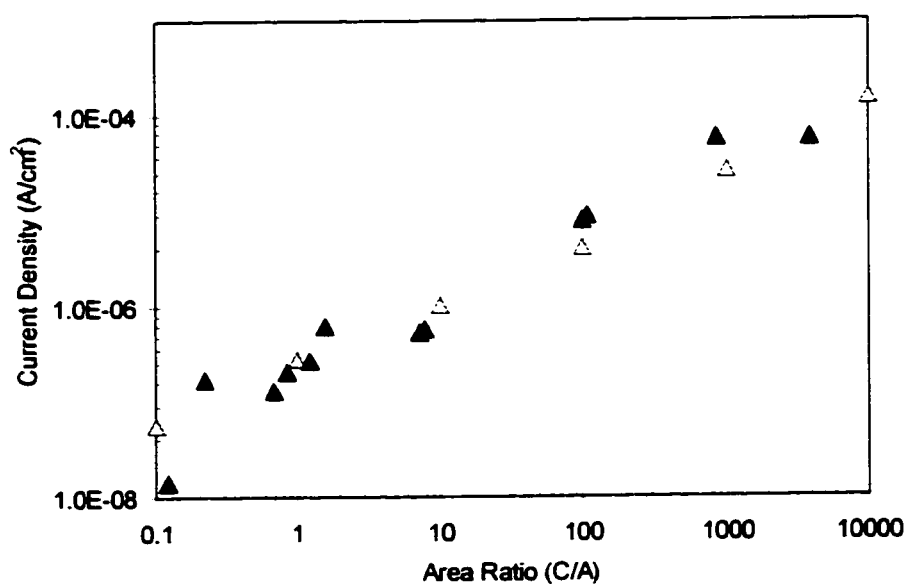


Figure 4.36. Comparison of galvanic current densities, obtained directly (▲) and indirectly (△) for p-GaAs ($4 \times 10^{19}\text{cm}^{-3}$).

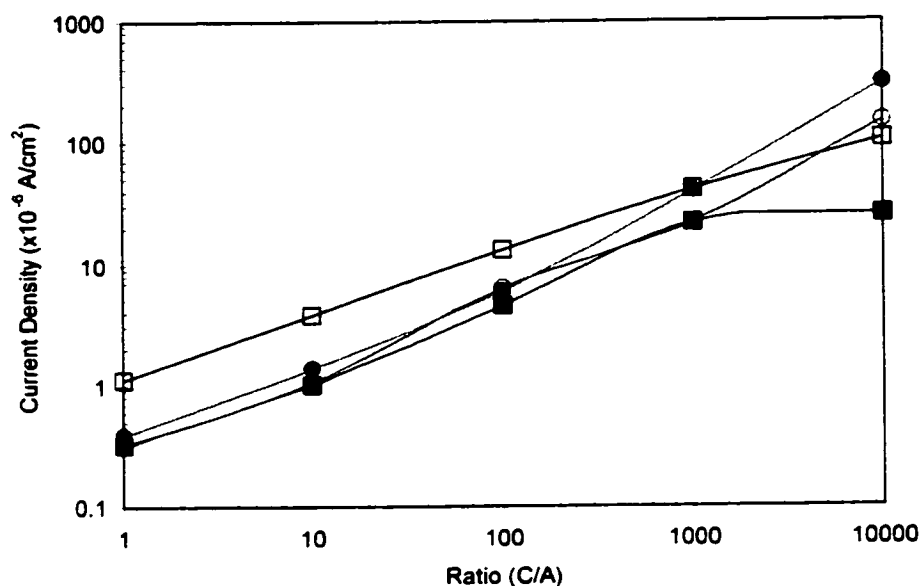


Figure 4.37. Galvanic current densities measured by superposition of cathodic (Au) and anodic (p-GaAs) polarization curves in 28.5% H_3PO_4 : \square) 10^{18}cm^{-3} , daylight; \blacksquare) 10^{18}cm^{-3} , dark; \circ) $4 \times 10^{19}\text{cm}^{-3}$, daylight and \bullet) $4 \times 10^{19}\text{cm}^{-3}$, dark.

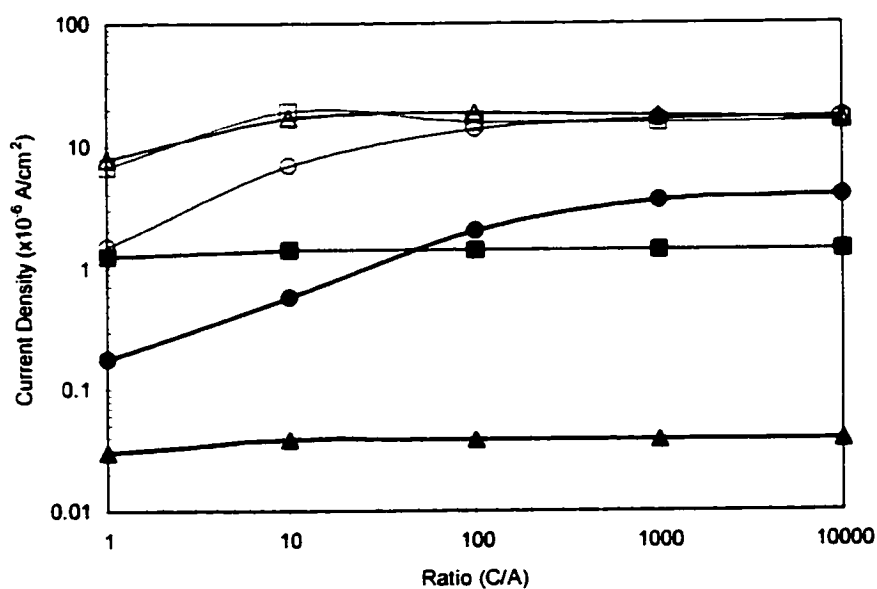


Figure 4.38. Galvanic current densities measured by superposition of cathodic (Au) and anodic (n-GaAs) polarization curves in 28.5% H_3PO_4 : Δ) 10^{18}cm^{-3} , daylight; \blacktriangle) 10^{18}cm^{-3} , dark; \square) $2 \times 10^{18}\text{cm}^{-3}$, daylight; \blacksquare) $2 \times 10^{18}\text{cm}^{-3}$, dark; \circ) $5 \times 10^{18}\text{cm}^{-3}$, daylight and \bullet) $5 \times 10^{18}\text{cm}^{-3}$, dark.

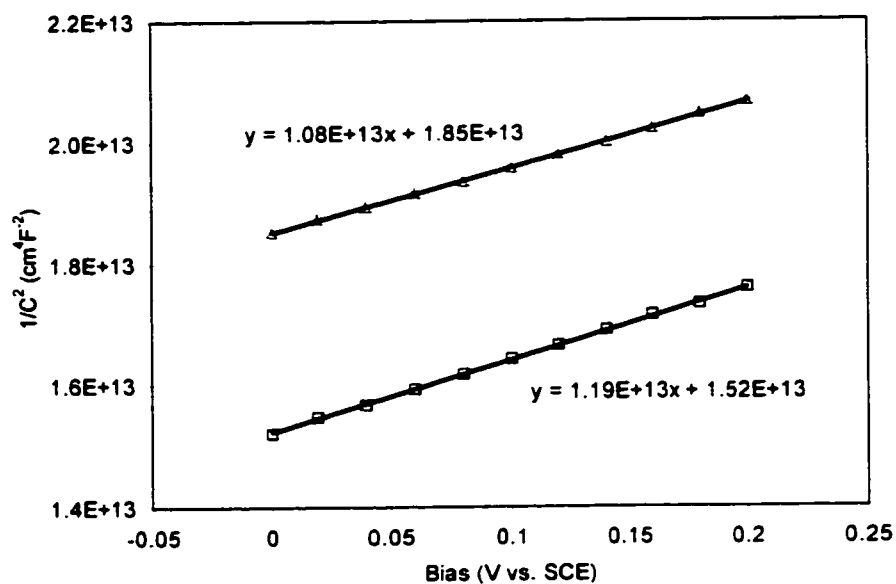


Figure 4.39. Mott-Schottky plots for n-GaAs (10^{18} cm^{-3}) in phosphoric acid in the dark (Δ) and daylight (\square).

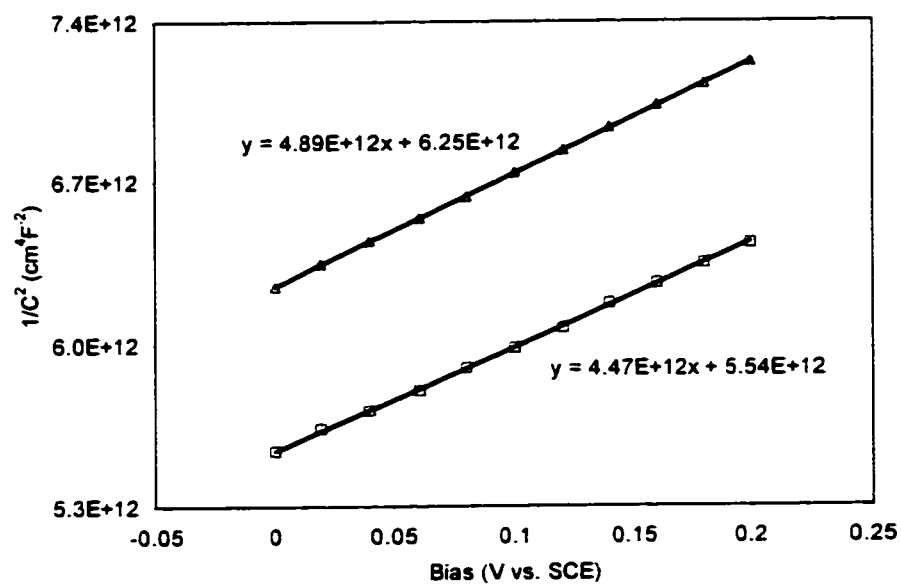


Figure 4.40. Mott-Schottky plots for n-GaAs ($2 \times 10^{18} \text{ cm}^{-3}$) in phosphoric acid in the dark (Δ) and daylight (\square).

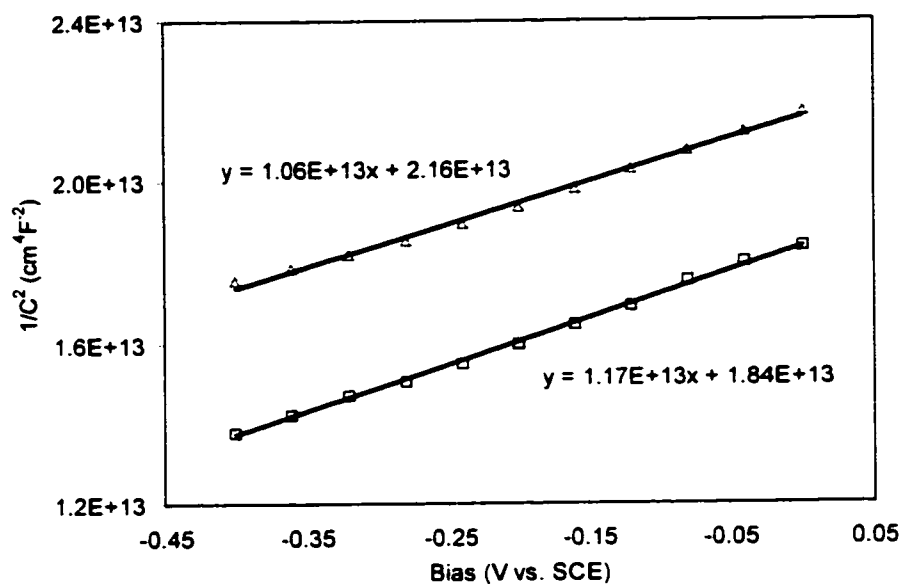


Figure 4.41. Mott-Schottky plot for n-GaAs (10^{18} cm^{-3}) in deionized water in the dark (Δ) and daylight (\square).

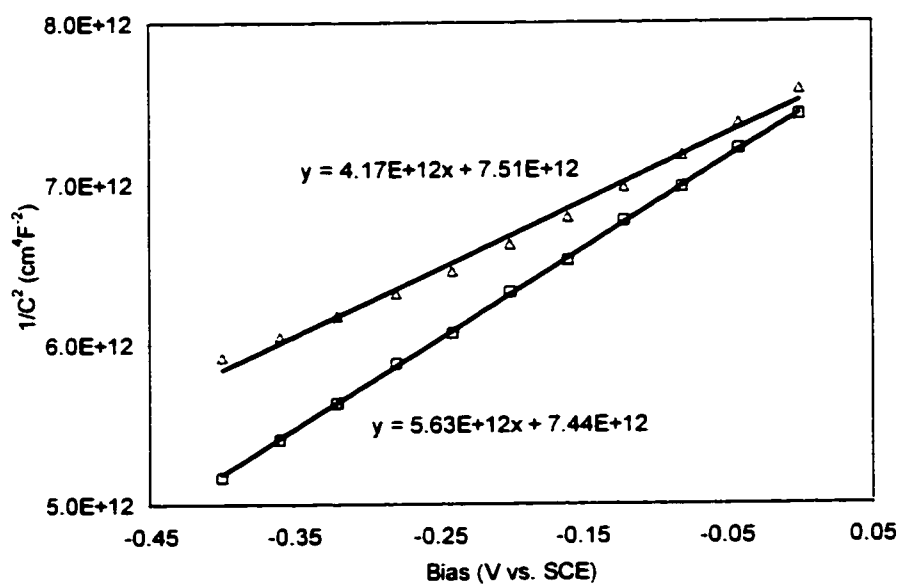


Figure 4.42. Mott-Schottky plots for n-GaAs ($2 \times 10^{18} \text{ cm}^{-3}$) in deionized water in the dark (Δ) and daylight (\square).

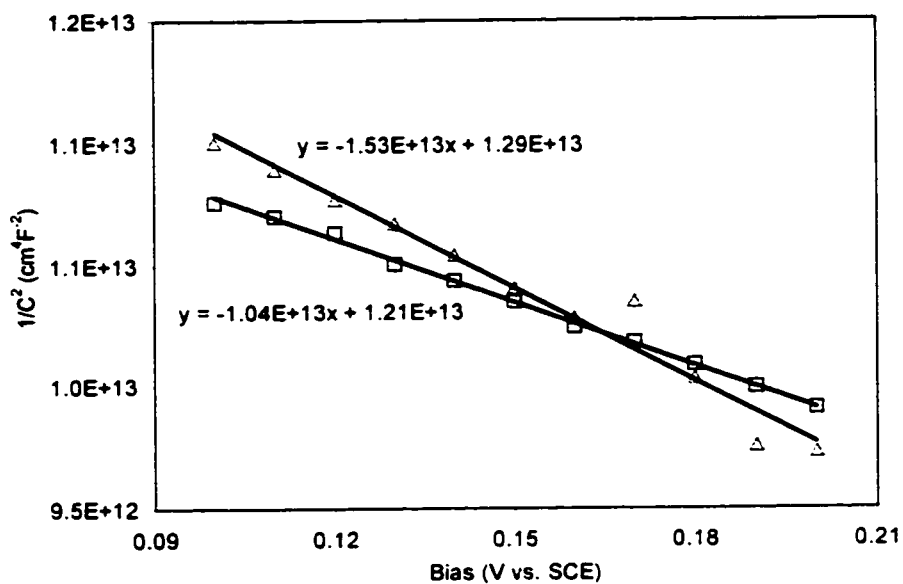


Figure 4.43. Mott-Schottky plots for p-GaAs (10^{18} cm^{-3}) in phosphoric acid in the dark (Δ) and daylight (\square).

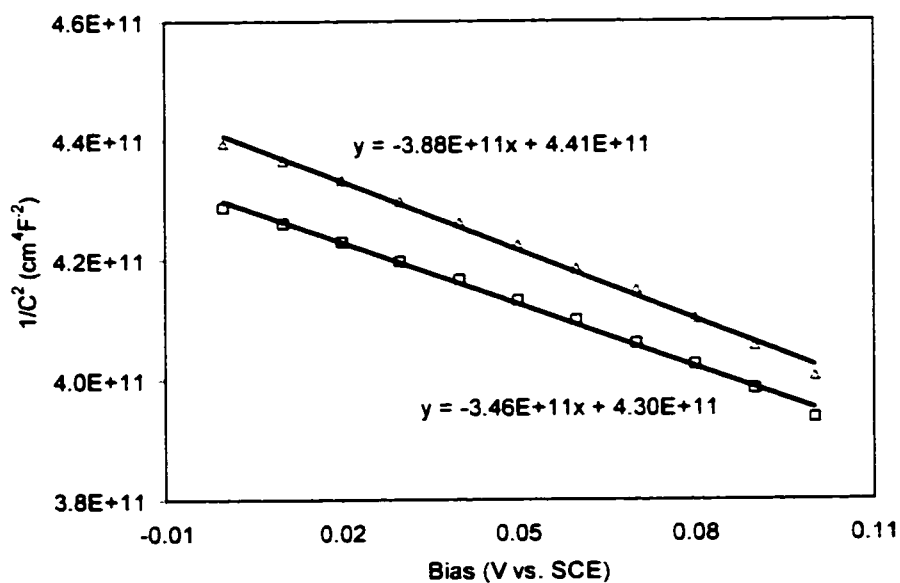


Figure 4.44. Mott-Schottky plots for P-GaAs ($4 \times 10^{19} \text{ cm}^{-3}$) in phosphoric acid in the dark (Δ) and daylight (\square).

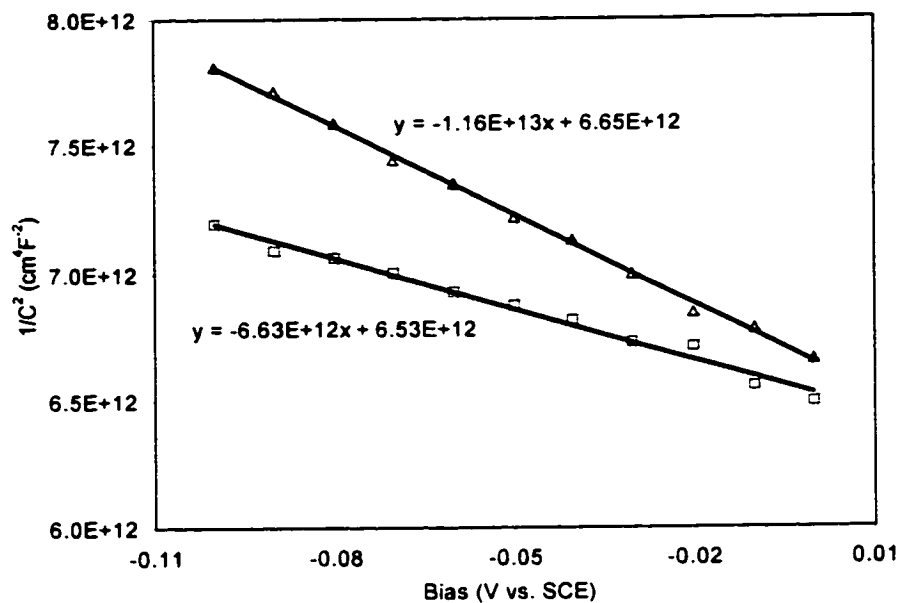


Figure 4.45. Mott-Schottky plots for p-GaAs (10^{18}cm^{-3}) in deionized water in the dark (Δ) and daylight (\square).

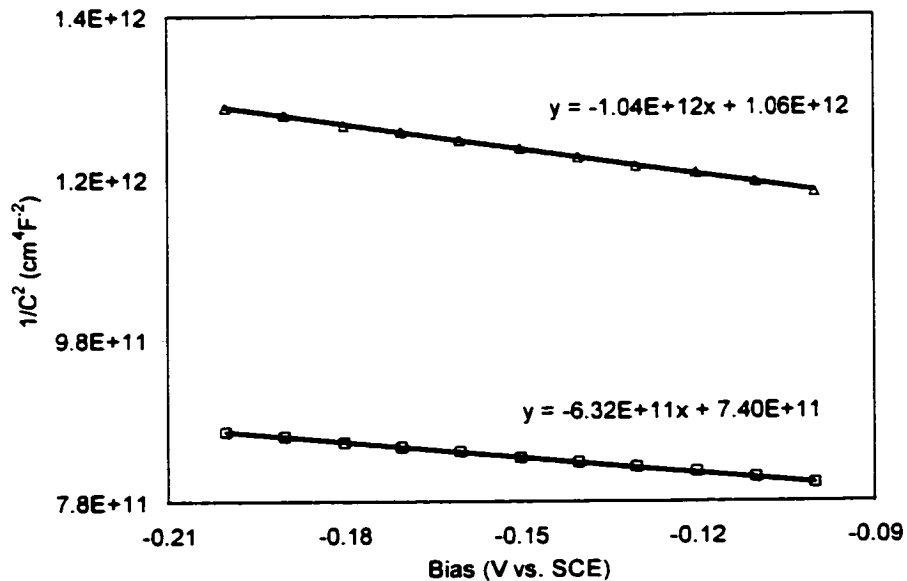


Figure 4.46. Mott-Schottky plots for p-GaAs ($4 \times 10^{19}\text{cm}^{-3}$) in deionized water in the dark (Δ) and daylight (\square).

CHAPTER 5

DISCUSSION

5.1. Formation of arsenic oxide

The XPS analysis clearly demonstrates that the as-received GaAs specimens were covered with a surface oxide comprised of Ga_2O_3 , As_2O_3 and As_2O_5 . Polarization in acid solutions dissolved the surface oxide. The small amount of As_2O_3 detected on the surface immediately after polarization was likely formed in air during rinsing and transfer to the XPS spectrometer. The compositions shown in Table 4.2 indicate that there is preferential dissolution of Ga during polarization leaving a significantly higher As/Ga ratio on the specimen surface. This was confirmed by ICP analysis. To compare the dissolution rate of arsenic and gallium during electrochemical tests, the concentrations of arsenic and gallium ions dissolved in the test solutions were determined with ICP after specimens were polarized at 0.75 V (vs. SCE) for 2 hours. Selective dissolution of Ga was evident for p-GaAs (both in dark and light) and n-GaAs (light), with the Ga concentration exceeding that of As by more than one order of magnitude. For example, the n-GaAs (10^{18} cm^{-3}) sample had 0.012 mg/L of Ga and <0.001 mg/L of As in the test solution. This indicates that Ga dissolved faster than arsenic during polarization in phosphoric acid.

Surface enrichment of As has also been reported for <111> oriented GaAs specimens (p-type, $9 \times 10^{18} \text{ cm}^{-3}$) exposed to acidic solutions (pH = 2.5) under both anodic

and open circuit conditions [Lingier and Gomes, 1991]. The proposed reactions are as follows:



The anodic reaction (5.1a) is possible for low enough potentials (<0.1 V vs. SCE), but not for the conditions experienced in this work. The following model is proposed for the dissolution of GaAs and subsequent particle formation in this work. According to the Pourbaix diagram for the GaAs-H₂O system at 25°C, the stable species at 0.75 V and pH values of $-2 \sim 3$ are Ga^{3+} and $\text{H}_3\text{AsO}_4(\text{aq})$, which are soluble (Fig. 2.10).



Note, that holes are required for the above reaction to proceed to the right. Based on Eq. (5.2), one would not expect to get As enrichment of the GaAs surface during anodic dissolution, i.e., GaAs dissolution results in both As and Ga going into solution. However, the Pourbaix diagram only provides thermodynamic information as to probable reactions and not reaction rates. It has been reported [Li and Peter, 1986] that Ga species solubility exceeds that of the As species at pH values below 2. The pH of the phosphoric acid solution utilized in the present work is 0.5, which is clearly in this range. Faster Ga dissolution would result in the anodic surface segregation of a layer of arsenic (Fig. 4.23a). This thin layer of arsenic is first distributed uniformly over the entire surface. Upon exposure to air, the arsenic oxidizes and agglomerates, forming crystalline particles (Fig. 4.23c):



The driving force for both As_2O_3 and As_2O_5 formation is quite large, i.e., ΔG_f^0 values at 298 K are -576 kJ/mol and -772 kJ/mol for As_2O_3 and As_2O_5 , respectively

[Wicks et al, 1963]. As_2O_5 formation is thermodynamically preferred; however, only As_2O_3 formed after anodic polarization. The formation of As_2O_3 particles, as shown in Figs. 4.18 and 4.19, leaves the underlying GaAs exposed to air. The sharp decrease in the surface As/Ga ratio of GaAs after 7 days of exposure to air (Table 4.2) is due to contribution from the GaAs substrate. The oxide layer formed on the specimen surface at this stage consisted of As_2O_3 particles combined with a mixture of Ga_2O_3 and As_2O_5 , due to oxidation of the GaAs substrate.

Ishikawa and Ikoma also used XPS to analyze the oxides of GaAs. They found that the oxidation of As bound in GaAs advanced as $\text{GaAs} \rightarrow \text{As} (\text{As}^0) \rightarrow \text{As}_2\text{O} (\text{As}^{1+}) \rightarrow \text{AsO} (\text{As}^{2+}) \rightarrow \text{As}_2\text{O}_3 (\text{As}^{3+}) \rightarrow \text{As}_2\text{O}_5 (\text{As}^{5+})$. Oxidation of Ga bound in GaAs proceeds as $\text{GaAs} \rightarrow \text{Ga}_2\text{O} (\text{Ga}^{1+}) \rightarrow \text{GaO} (\text{Ga}^{2+}) \rightarrow \text{Ga}_2\text{O}_3 (\text{Ga}^{3+}) \rightarrow \text{Ga}_2\text{O}_5 (\text{Ga}^{5+})$. These results indicate that elemental As is an oxidized form, while Ga is not the oxidized but a reduced form of GaAs.

The absence of As_2O_3 particle formation in all samples tested at the corrosion potential and n-type samples tested in the dark can be explained by examining potentiodynamic scans. These are shown for n- and p-GaAs (10^{18}cm^{-3}), tested in phosphoric acid in both the dark and daylight, in Fig. 4.7. At the corrosion potential, the dissolution rate of n- and p-GaAs is very low, leaving the surface intact with little or no As enrichment at the surface. For n-GaAs polarized in the dark, the anodic current density in the vicinity of 0.75 V is several orders of magnitude lower than that for p-GaAs, in either daylight or the dark, and 1 order of magnitude lower than n-GaAs tested in daylight. The low anodic current density translates into a low dissolution rate for GaAs and therefore little or no As surface enrichment. Actually, As_2O_3 and Ga_2O_3 are the main native oxides on as received GaAs, with a small amount of element arsenic present. According to Bertrand [1981], most of the oxide is removed after etching and As remains unetched. However, no arsenic oxides were found on the surface of n-GaAs tested in the dark after exposure to air for several days in this work, indicating that As enrichment on the surface is minimal.

It has been identified in this work that, after polarization within a certain potential range, an As rich layer was formed on the surface and was oxidized when exposed to air. The oxide particles grew with increasing exposure time (Fig. 4.18), indicating As oxidation takes time. This phenomenon has been continually observed for several months. One sample (n-GaAs, 10^{18}cm^{-3} tested in phosphoric at 0.75 V vs. SCE for 5 hours in daylight) was examined again after exposure to air for 100 days. It was found the particle size on the surface was much larger than for 2 weeks, growing from 2 μm to 10 μm . The particles were identified using thin film x-ray diffraction (XRD). A representative spectrum is shown in Fig. 5.1.

The Bragg angles (2θ) for the two peaks (indicated by dashed lines) were measured as 52.7° and 53.6° , respectively. The spacings (d) can be calculated with following equation:

$$2d \sin \theta = \lambda \quad (5.4)$$

where $\lambda=0.1541\text{nm}$. Only two peaks were detected with the d spacings being 0.1735 nm and 0.1709 nm, respectively. The lack of peaks can be attributed to the relatively small particle size and incomplete coverage. The d spacings were compared with standard powder diffraction files (PDF) for As oxide (Table 5.1A). Two of the peaks of standard PDF file for As_2O_3 with d spacings of 0.1736 nm and 0.1716nm are very close to the experimental XRD results, thus the particles can be tentatively assigned as As_2O_3 . This is in agreement with the result from XPS (Fig. 4.21).

In the work by Bohn et al [2000] and Lockwood et al [2000], As_2O_3 was reported to form during anodic polarization, whereas the results of this work clearly showed that As enrichment occurs during polarization but particle formation occurs after testing. There are 2 possible explanations for this discrepancy. Both Bohn and Lockwood used significantly higher potentials (up to 7 V), which produced a porous surface and possibly a different particle formation mechanism. Perhaps more significant, however, is the timing of their characterization. EDX, AES (Auger electron spectroscopy) and XPS were

used to examine the processed surfaces, but no indication was given as to when the analyses were done. Unless the characterization was done immediately after anodic processing, one can only speculate as to when particle formation occurred. To test the second hypothesis, n-GaAs (10^{18} cm^{-3}) samples were potentiostatically polarized in the dark in phosphoric acid at 7 V for 2 hours and then examined immediately after testing. SEM images from one such sample are shown in Fig. 4.27. It appears, therefore, that the particle formation process is different at higher potentials; the excess As produced during anodic polarization oxidizes in the solution. XRD was also used to examine this surface structure immediately after polarization test. The spectrum is shown in Fig. 5.2, with peaks listed in Table 5.1B. Compared with the standard powder diffraction file (Table 5.1), not only do the d spacings of main peaks (No. 1, 2 and 9) detected from the particles match very well with standard PDF file for As_2O_3 , but the d spacing of other weak peaks from particle are also very close to that of stand PDF file. Thus the particles on the surface were deemed to be As_2O_3 . It can be concluded the anodic dissolution of GaAs in acid at higher potential results in the formation of oxide.

Comparing the peaks in Sample A with those in Sample B, it is apparent that peak No. 1 and 2 for Sample A are very close to No. 9 and 10 for Sample B, respectively. Since peak No. 9 is one of the strongest peaks in Sample B, this provides confirmation that the particles on Sample A are likely the same as those on Sample B.

It has been shown that rates of oxide growth and oxide dissolution were identical and entirely controlled by the pH of the solution [Gerard et al, 1997]. Oxide can be grown locally on the n-GaAs surface at higher pH values [Gerard et al, 1999]. In their work, gallium oxide was formed on the surface at pH=9 and photodissolution of n-GaAs was entirely controlled by the oxide dissolution.

Table 5.1. XRD results for surface layers at polarized n-GaAs (10^{18}cm^{-3})

Experimental XRD Results					Standard PDF File of As_2O_3				
Sample	Peak	2-Theta	d (nm)	I%	d (nm)	I%	h	k	l
A	1	52.697	0.1735	100	0.1752	1	6	2	0
	2	53.599	0.1709	12.3	0.1689	1	5	3	3
B	1	13.752	0.6434	100	0.6399	44	1	1	1
	2	27.803	0.3206	34.5	0.3199	100	2	2	2
	3	32.163	0.2781	13.8	0.2770	26	4	0	0
	4	35.214	0.2547	27.6	0.2542	34	-1	2	0
	5	35.288	0.2541	27.6	0.2542	34	-1	2	0
	6	39.770	0.2265	13.8	0.2262	6	4	2	2
	7	42.310	0.2135	13.8	0.2133	12	5	1	1
	8	46.261	0.1961	27.6	0.1959	22	4	4	0
	9	52.607	0.1738	93.1	0.1752	1	6	2	0
	10	53.450	0.1713	13.8	0.1689	1	5	3	3
	11	54.952	0.1670	10.3	0.1670	14	6	2	2
	12	59.419	0.1554	17.2	0.1552	14	5	5	1
	13	59.675	0.1548	17.2	0.1552	14	5	5	1
	14	64.461	0.1445	13.8	0.1442	7	7	3	1
	15	69.498	0.1352	13.8	0.1353	7	7	3	3

5.2. Localized corrosion

Potentiodynamic polarization curves for n-GaAs clearly show that the current density remains low over a wide potential range. A steep increase in the current density occurs as soon as a critical potential is reached (Fig. 4.2). This phenomenon can be explained by the initiation of localized corrosion. If the localized corrosion takes the form of pitting, the critical potential is defined as the pitting potential. Fig. 4.24 provides evidence for the occurrence of localized corrosion. The sample (n-GaAs, $2 \times 10^{18} \text{ cm}^{-3}$) was polarized in phosphoric acid in daylight for 5 hours at 0.75 V, which is above the critical potential. Under these conditions, pores are formed across the surface. Comparison with the same sample polarized at -0.15 V, which is below the pitting potential, shows that the surface of the lower potential sample is relatively smooth with some As-enrichment on the surface (Fig. 4.22). Other evidence for localized corrosion occurring when the potential reaches a critical potential (pitting potential) was obtained through AFM studies (Fig. 4.5).

EDX investigation was also done to compare any differences in composition between the porous region and bulk GaAs (Fig. 4.24). Similar compositions were obtained. The EDX analysis performed on the porous area resulted in a As/Ga intensity ratio close to that for the bulk. In order to obtain information on the composition of the porous structure, particularly to determine if selective dissolution took place, Schmuki et al [1996] acquired AES sputter profiles on a heavily attacked region of a n-GaAs (10^{17} cm^{-3}) sample in 0.1 M HCl. The sample had undergone localized corrosion and the profiles were compared with an AES profile of a clean GaAs sample. They found that most areas of the porous structure showed a As/Ga ratio close to 1, except for a region at the outer surface. In this region As enrichment was observed. Tromans et al [1993] also found that the underlying porous structure (in 1M NaNO_3) consisted of stoichiometric GaAs. These results indicate no selective dissolution of one of the components occurs and therefore the remaining structure is also expected to consist mainly of GaAs.

The initiation of pitting attack can be caused by the defects on the surface. Schmuki and co-workers [1997] postulated that pore formation on anodically etched GaAs originates at extended GaAs surface defects, such as dislocations. This assertion was supported by the work done by Ross et al [1997] who formed pitted GaAs surfaces in 49% HF and concluded that pit formation begins at defect sites. However, pore formation may also be initiated at point defects. It was found that for n-GaAs, the total number of point defects increased with increasing doping density, resulting in a large number of smaller pits [Finnie et al, 1999]. This indicates that pit formation may be dependent on the number of point defects.

Pitting initiation from defects can be explained by the following factors. One is that microroughness may cause a geometric configuration where a buildup of highly concentrated solution is caused by mass transport conditions (the dissolution of Ga^{3+} and/or As^{3+}) [Schmuki et al, 1993]. Thus localized corrosion occurs. Another factor is that different crystal planes become exposed to the electrolyte solution at defect positions. Because of the different number of back bonds attaching a surface atom to the lattice, reactivity is variable for different planes, which can cause pitting [Schmuki et al, 1995]. In order to elucidate the possibility that reaction rate is variable at different lattice planes, Schmuki and co-workers cleaved a GaAs sample along the (110) direction and (011) direction, and then the sample was exposed to pitting conditions in $\text{NH}_4\text{H}_2\text{PO}_4 + 1\text{M Cl}^-$ at 4V for 5 minutes. It was observed that the susceptibility of the planes to the electrolyte solution in this experiment increased in the following order: (100) << (011) < (110).

For p-type GaAs in phosphoric acid (Fig. 4.4), the current in the anodic direction increases markedly to very high values compared with that for n-GaAs. The current then decreases to slightly lower values when the potential reaches a critical value and remains constant, indicating passivation has taken place. However, TEM investigation of a sample (p-GaAs, $4 \times 10^{19} \text{cm}^{-3}$) after the experiments, in which the sample was polarized at three potentials (0.15V, 0.4V and 0.75V, respectively) for 2 hours, clearly shows that the

sample surface is covered with a As-rich layer and the thickness increases with increasing potential (Figs. 4.28-4.30). This surface layer is amorphous and uniform.

The surface change for both n-GaAs and p-GaAs polarized at different potentials are schematically shown in Fig. 5.3. The left hand side is n-type with p-type on the right hand side. The polarization curves for the two samples are shown below. For n-GaAs, the surface As-rich layer increased in thickness with increasing potential. At low anodic potentials (Fig. 5.3a), the thickness of As-rich layer is less than 2 nm, indicating the anodic reaction rate is very small. As discussed before, holes are required for the dissolution of GaAs. For n-GaAs, holes are minority carriers, so only a limited number of holes are available to take part in the process of anodic dissolution. As the potential is increased, the band bending is also increased; more holes are able to reach the surface and increasing the dissolution rate of GaAs. At a critical potential the anodic current becomes saturated. In this case all the available holes are involved in the anodic reaction, and the surface layer reaches a thickness of ~30 nm (Fig. 5.3b). When the potential reached the breakdown potential (which depends on doping level), the semiconductor surface is inverted to p-type. Thus, sufficient holes are available to participate anodic dissolution. Pitting is initiated and the surface becomes porous (Fig. 5.3c).

Because holes in p-GaAs are the majority carriers, anodic dissolution was relative fast compared with n-GaAs and the As-rich layer is thicker even at lower potentials (Fig. 5.3d). There was not a saturated current density for p-GaAs since there are huge holes available on the surface; however, when it reached a particular potential, the current density remained constant as the potential increased (Fig. 5.3f). This behaviour appears to be similar to that for n-GaAs. Since the substrate for p-GaAs is $1 \times 10^{18} \text{ cm}^{-3}$ n-GaAs with a 500 nm epitaxial p-GaAs layers grown on the top, there was concern as to whether the top layer dissolved away during polarization, leaving an n-GaAs sample. The dissolution of GaAs in phosphoric acid can be calculated from the following equation:

$$d = \frac{V}{S} \frac{\int I dt}{nF} \quad (5.5)$$

where

d = thickness of dissolution, cm;

V = molar volume, cm^3/mol ;

S = area, cm^2 ;

I = current, A;

t = time, s;

n = ionic charge associated with the electrode process ($n=8$ for GaAs dissolution);

F = Faraday constant, 96500 C/mol.

The molecular weight of GaAs is $(67.9+74.91)$ g/mol=144.6 g/mol and the density is 5.32 g/cm³. Thus we have

$$V = \frac{144.6 \text{ g/mol}}{5.32 \text{ g/cm}^3} = 27.2 \text{ cm}^3/\text{mol} \quad (5.6)$$

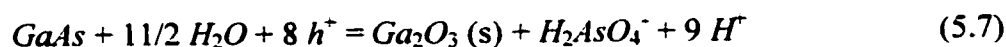
Substitution of the values in Fig. 4.4 and Eq. 5.6 into Eq. 5.5, produced a dissolution thickness for p-GaAs (10^{18} cm^{-3} and $4 \times 10^{19} \text{ cm}^{-3}$) for the potentials encountered in this work of 52.2nm and 50.4nm, respectively. Thus it is clear that the top layer is not dissolved away and the corrosion behaviour should not be the same as n-GaAs.

In fact, the constant current density for p-GaAs was attributed to the thick surface layer (~140 nm) (Fig. 5.3e), which limited diffusion of the semiconductor ions. This result is in good agreement with the work performed by Schmuki and co-workers [1995], who did similar experiments in acidic solutions and a uniformly smooth surface was observed after dissolving the surface layer. It is clear that for the p-GaAs in phosphoric acid no passivation takes place and electropolishing takes place without any local preferential attack.

5.3. Corrosion in deionized water

The dissolution processes for oxides on the GaAs surface during polarization in deionized water were different from those in acid. Polarization in deionized water did not remove the surface film, instead the oxide film thickened (Figs. 4.25 and 4.26). Selective dissolution of As oxide caused a minor decrease in the As/Ga ratio of the surface oxide (Table 4.3). XPS analyses for n-GaAs following potentiostatic testing in deionized water (Table 4.3 and Figs. 4.25 and 4.26) show that the amount of oxide on the GaAs surface did not change significantly upon exposure to air. Ga_2O_3 was much more stable than As_2O_3 in water when no external potential was applied to the specimen [Hirota and Sugii 1991]. As_2O_3 started to dissolve when the specimen was rinsed in water for 1 minute. Rinsing for 15 minutes resulted in strong dissolution of As_2O_3 ; XPS spectra indicated only a weak oxide peak for As_2O_3 , while a considerable contribution from Ga_2O_3 was still detected.

The experimental observations agree with the Pourbaix diagram for the GaAs- H_2O system (Fig. 2.10) [Tromans et al, 1993], where the stable species for potentials greater than -0.1 V SCE are expected to be Ga_2O_3 and H_2AsO_4^- . As with acidic solutions, dissolution of GaAs requires holes.



Only one of the semiconductor species is aqueous (H_2AsO_4^-), unlike polarization in acidic solutions.

The characteristic difference between polarization curves of n- and p-type GaAs in acid solutions was not detected in deionized water. Because of the presence of the stable oxide film, the anodic current densities were mainly due to the slow dissolution of the oxide and anodic dissolution was not dependent on the availability of holes. Therefore, the anodic current densities for n-GaAs were almost the same when the potential was between 0 and 0.5V, as shown in Fig. 4.11. For lower doped n-GaAs (10^{17}

and 10^{18}cm^{-3}), the current density remained constant when the potential was above 0.5 V and can be attributed to the thick oxide, which prevented contact between the semiconductor and solution. For higher doped n-GaAs ($2 \times 10^{18}\text{cm}^{-3}$ and $5 \times 10^{18}\text{cm}^{-3}$), the oxide was formed and inhibited the anodic dissolution when the potential was lower than 0.5 V. However, with increasing potential, breakdown occurred.

The anodic process for p-GaAs is very similar to higher doped n-GaAs and the current densities are very close (Fig. 4.12), indicating that breakdown also occurred.

5.4. Corrosion mechanisms

As discussed above, the dissolution of GaAs depends on the availability of holes in the valence band (Eqs. 5.2 and 5.7). Several mechanisms for generating the necessary holes will be proposed in the following paragraphs. These are shown schematically in Fig. 5.4, which shows the energy positions of the band edges vs distance from the semiconductor/solution interface.

For n-GaAs, holes are minority carriers. Figs. 5.4a and b give 2 possible ways of producing holes in the valence band. In the first mechanism (Fig. 5.4a), holes are produced by internal field emission of electrons, when the applied field is high enough, from the valence band edge at the surface into the conduction band [Pettinger et al, 1974; Gerischer, 1990]. This phenomenon occurs in acid solutions when n-GaAs (10^{17} , 10^{18} , 2×10^{18} and $5 \times 10^{18}\text{cm}^{-3}$) is polarized at potentials greater than ≈ 1.0 , 0.9, 0.6, and 0.4 V, respectively (Fig. 4.2). The breakdown potential decreased with increasing doping density. This can be explained by the relationship between Schottky barrier and doping density. The width of the Schottky barrier (w) is proportional to the reciprocal of square root of the doping density N_D . Therefore, tunneling barrier width decreases as the doping density increase allowing tunneling to occur at lower potentials. If surface states exist, the

hole generation process by internal field emission begins on the surface. Surface states can mediate charge transfer of both majority and minority carriers, control surface charge and band bending and catalyze recombination of photo-generated charge carriers.

A second mechanism for hole generation in n-GaAs is light absorption. Photons with sufficient energy (greater than the band gap energy) can excite electrons from the valence band into the conduction band, producing holes in the valence band (Fig. 5.4b). When the anodic potential produces enough band bending at the GaAs surface, holes are able to reach the surface and anodic dissolution can take place. The photon-induced phenomenon is a contributing factor in this work; the results in Fig. 4.7 clearly indicate acceleration of anodic dissolution for n-GaAs by photon absorption. The smaller difference between anodic current densities for n-GaAs and p-GaAs in daylight compared with the dark (Fig. 4.7) is also an indication that injection of holes into the GaAs surface by photo-excitation enhances the anodic dissolution of n-GaAs. The effect of light is much less pronounced for n-GaAs doped to a level of $5 \times 10^{18} \text{ cm}^{-3}$ (Fig. 4.9), which may be attributable to a high density of surface states in this material (first mechanism) and also due to the lower breakdown potential.

Light has very little effect on the polarization behaviour of p-GaAs, as there are already a significant number of holes.

5.5. Measurement of flat band potential

The flat band potential is a measure of the position of the Fermi level for both n- and p-type semiconductors. Thus the distance between the two flat band potentials corresponds to the difference in energy between the two Fermi levels. This difference approximately equals the band gap, which is 1.43 eV for GaAs. In this work, the distance between the two intersections for n- and p-type GaAs (10^{18} cm^{-3}) in the dark or daylight, phosphoric acid or deionized water, are very close (2.44 eV ~ 2.61 eV) (Table. 4.6).

However, this range of values is much higher than the band gap of GaAs. This can be explained as follows. In certain cases, an insulating layer such as an oxide layer is present between the semiconductor and electrolyte phases; the interface always includes the outer Helmholtz layer. An As-rich layer formed on the surface in this work (Fig. 4.28). If the capacitance of such an additional layer C_H is voltage-independent, the total capacitance C and the potential difference can be calculated from the following relationship [Gryse, et al, 1975]:

$$C^{-2} = C_H^{-2} + \left(\frac{2}{eN\epsilon\epsilon_0}\right)\left(V - V_{fb} - \frac{kT}{e}\right) \quad \text{for n-type semiconductors} \quad (5.8a)$$

$$C^{-2} = C_H^{-2} - \left(\frac{2}{eN\epsilon\epsilon_0}\right)\left(V - V_{fb} - \frac{kT}{e}\right) \quad \text{for p-type semiconductors} \quad (5.8b)$$

It is clear that the relationship between C^{-2} and V is still linear and has the same slope as in Eq. 4.5. However, instead of Eq. 4.6, the flat band potential is determined by the following equation:

$$V_{fb} = V_0 + \frac{\epsilon \cdot \epsilon_0 e N_D}{2C_H^2} \quad \text{for n-type semiconductors} \quad (5.9a)$$

$$V_{fb} = V_0 - \frac{\epsilon \cdot \epsilon_0 e N_D}{2C_H^2} \quad \text{for p-type semiconductors} \quad (5.9b)$$

An ionic adsorption layer established at the semiconductor/electrolyte interface also contributes to the total capacitance [Cardon and Gomes, 1978]. In this case, the surface charge is often assumed to be voltage-independent. Eq. 5.9 still holds, C_H has a significant effect due to the outer Helmholtz layer capacitance, and V_{fb} includes the

potential drop due to the surface charge and its counterpart in the outer Helmholtz layer. It seems necessary, therefore, to make a correction for the Helmholtz layer capacitance in order to obtain the true value of the space charge layer capacitance.

The shift of flat band potential in this work may be explained by the surface states. Reichman [1980] discussed the influence of surface states on the potential distribution at the semiconductor/electrolyte interface. A shift of 200 mV in the Mott-Schottky plots requires a surface state density of about 10^{13}cm^{-2} . Another possible explanation is that shift in flat band potential reflects changes in the surface dipole potential resulting from a chemical transformation of the surface. The shift in flat band potential under illumination based on that the transformation involves an oxidation process.

The difference in flat band potential between phosphoric acid and deionized water is attributed to the pH difference. The flat band potential shifts by -55 mV per unit pH increase [Finklea, 1988]. This is usually attributed to an acid-base equilibrium leading to a charge on the electrode surface, i.e., reaction involving adsorbed H^+ or OH^- ions. [Cardon and Gomes, 1978]. The results from Table 4.6 do match the above very well with some exceptions. However, the flat band potential shifts negative with increasing pH.

It has been summarized that the determination of the dopant concentration from the slope of the Mott-Schottky plot is based on a Faradaic process, the presence of surface states and a rough surface area on the electrode [Randin, 1974]. The acceptor concentration for p-GaAs ($4 \times 10^{19}\text{cm}^{-3}$) from the Mott-Schottky in this work is much lower than the original value and may be due to the factors described above; however the specific mechanism is unclear.

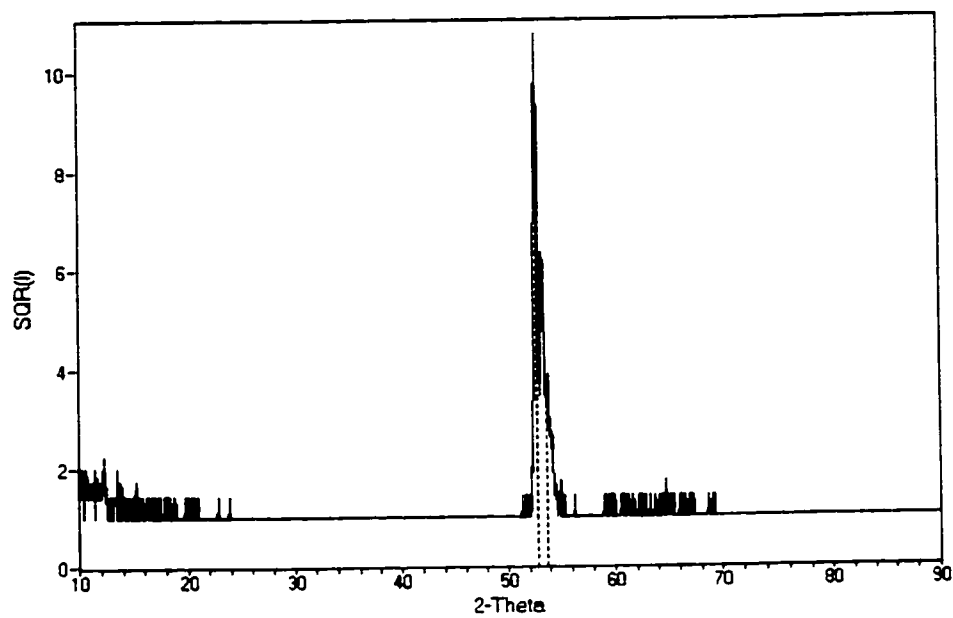


Figure 5.1. XRD spectrum for n-GaAs (10^{18}cm^{-3}) exposed to air for 100 days after testing at 0.75 V vs. SCE for 5 hours in phosphoric acid in daylight.

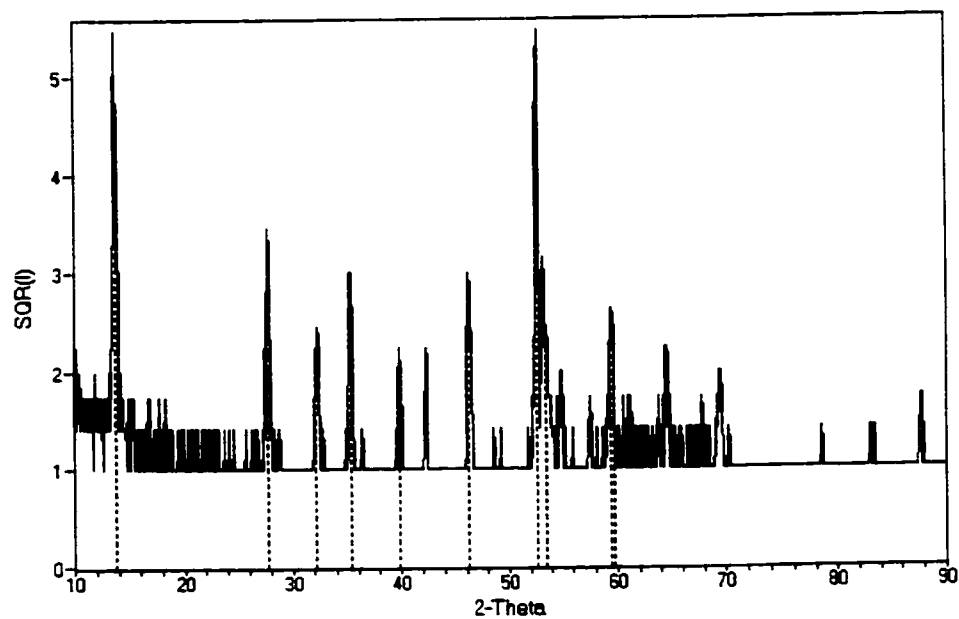


Figure 5.2. XRD spectrum for n-GaAs (10^{18}cm^{-3}) polarized at 7V vs. SCE for 2 hours in phosphoric acid in the dark.

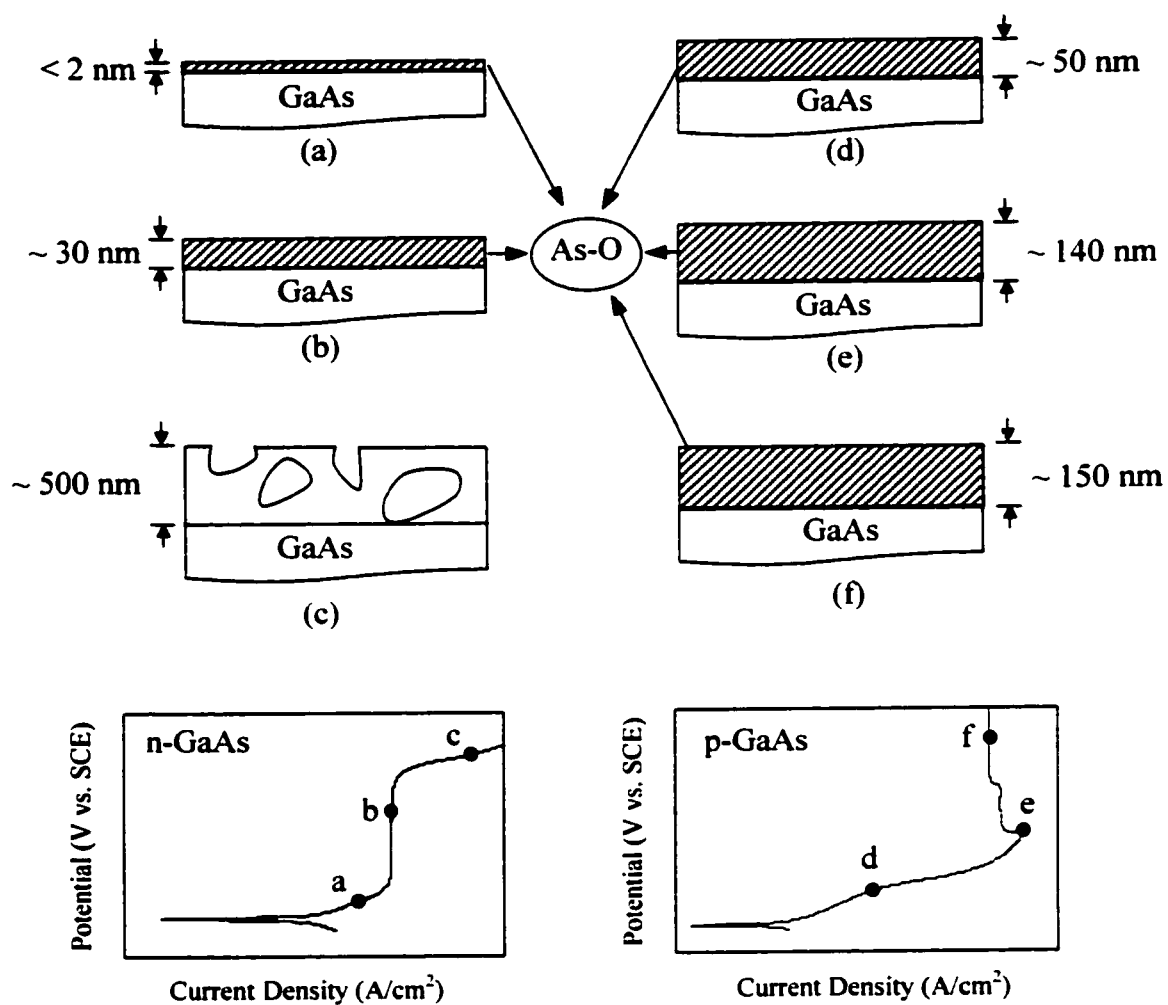
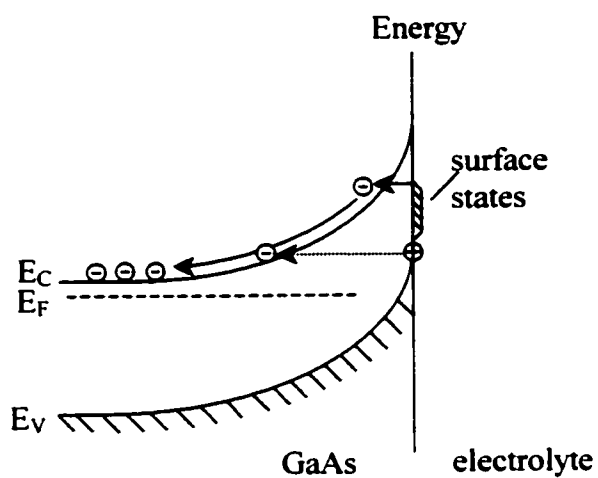
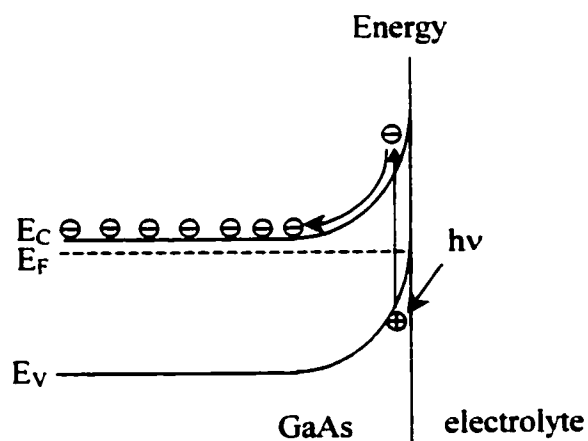


Figure 5.3. Schematic of the surface change for n-GaAs (a-c) and p-GaAs (d-f) polarized at different anodic potentials in phosphoric acid.



(a) n-type: electron tunneling



(b) n-type: photo excitation

Figure 5.4. Band diagrams for the semiconductor/electrolyte interface showing potential corrosion mechanisms of n-GaAs.

CHAPTER 6

CONCLUSIONS AND FUTURE WORK

6.1. Conclusions

Below the critical potential, anodic polarization in phosphoric acid resulted in the surface enrichment of As due to selective dissolution of Ga. Subsequent exposure to air resulted in gradual agglomeration of the As layer to As_2O_3 . For n-GaAs polarized in the dark, dissolution rates were significantly lower and As enrichment on the surface did not occur. Above the critical potential, localized corrosion occurred. The composition of porous region was the same as the bulk GaAs.

Polarization in deionized water only resulted in the thickening of the surface oxide formed on the GaAs surface and a slight decrease in the As/Ga ratio in the oxide layer. This layer prevented further oxidation of GaAs in air.

The anodic dissolution of GaAs in acids depends on the availability of holes. Illumination increases the tendency of n-GaAs towards active dissolution because of photo-generated holes. The anodic current densities for p-GaAs and highly doped n-GaAs are much higher than those for n-GaAs with low doping densities, because of the presence of holes in p-GaAs or surface states in highly doped n-GaAs. Therefore, illumination has less effect on anodic current densities for p-GaAs and highly doped n-GaAs.

Increasing the cathode/anode area ratio increases the galvanic corrosion rate for p-type and n-type GaAs. For n-GaAs, however, the galvanic corrosion rate reaches a saturation value (at a C/A ratio of about 10) due to the limited concentration of holes.

Superposition of anodic (GaAs) and cathodic (Au) polarization curves provides a good prediction of the galvanic corrosion rates.

For n-type GaAs, the galvanic current densities in phosphoric acid are higher in daylight than those in the dark, although this difference decreases as the doping level increases.

The flat band potentials determined in this work were not reasonable due to the incomplete equivalent circuit.

6.2. Future work

The corrosion behavior of GaAs and other III-V semiconductors should be studied in other electrolyte solutions with various illumination densities because the wide application of III-V semiconductors and semiconductors are etched with different acids and the density of illumination has significant effect on the reactions.

Open circuit potential and breakdown potential have been found related to the doping density and corrosion behavior of GaAs, however, the reasons are still not clear. It is necessary to determine how the open circuit potential and breakdown change with the doping density of GaAs and what effects on the corrosion.

An accurate equivalent circuit for impedance analysis of semiconductor electrode should be established for the determination of reasonable flat band potentials. The frequency should also be considered because at higher frequencies, the circuit may be reduced to a simple one.

REFERENCES

- Baboian, R. and S. W. Dean, Corrosion Testing and Evaluation: Silver Anniversary Volume (American Society for Testing and Materials, 1990)
- Baesland, M. P., Y. Rohach and J. Joseph, J. Electrochem. Soc., 140, 104 (1993)
- Bertrand, P. A., J. Vac. Sci. & Technol., 18, 28 (1981)
- Bradford, S. A., Corrosion Control (CASTI Publishing, Edmonton, Canada, 2001)
- Calister, W. D., Jr., Material Science and Engineering (John Wiley & Sons, Inc., United States, 2000)
- Carabba, M. M., N. M. Nguyen, and R. D. Rauh, J. Electrochem. Soc., 134, 1855 (1987)
- Cardon, F. and W. P. Gomes, J. Phys. D: Appl. Phys., 11, L63 (1978)
- Davis, G. O., J. Kolts and N. Sridhar, Corrosion, 42, 329 (1986)
- Dean, S. W. Jr., Electrochemical Techniques for Corrosion (Nation Association of Corrosion Engineers, Houston, 1976)
- Decker, F., B. Pettinger and H. Gerischer, J. Electrochem. Soc., 130, 1335 (1983)
- Finnie, C. M. and P. W. Bohn, Appl. Phys. Lett., 74, 1096 (1999)
- Finnie, C. M., Z. Li, and P. W. Bohn, J. Appl. Phys., 86, 4997 (1999)

Gerard, I., C. D. Chouvy, J. Vigneron, F. Bellenger, S. Kostelitz and A. Etcheberry, *Surf. Sci.*, 433, 131 (1999)

Gerard, I., J. Vigneron, L. Baudoui, C. Mathieu, C. D. Chouvy and A. Etcheberry, *Photoelectrochemistry 97-20* (The Electrochemical Society, Inc., NJ, USA, 1997)

Gerischer, H., *Electrochimica Acta*, 35, 1677 (1990)

Greenwood, N. N. and A. Earnshaw, *Chemistry of the Elements* (Butterworth-Heinemann, Boston, 1997)

Gryse, D. R., W. P. Gomes, F. Cardon and J. Vennik, *J. Electrochem. Soc.*, 122, 711 (1975)

Hechner, K. H., G. Majoros, Akraft and R. Landsberb, *Ber. Bunsenges. Phys. Chem.*, 99, 1514 (1995)

Hirota, Y. and K. Sugii, *J. Electrochem. Soc.*, 138, 799 (1991)

Hollan, L., J. C. Tranchart and R. Memming, *J. Electrochem. Soc.*, 126, 855 (1979)

Ishikawa, T. and H. Ikoma, *Jpn. J. Appl. Phys.*, 31, 12A (1992)

Ivey, D. G., J. Luo, S. Ingrey, R. Moore and I. Woods, *J. Electro. Mate.*, 27, 89 (1998)

Jones, D.A., *Corrosion*, 40, 181 (1984)

Jones, D. A., *Principles and prevention of corrosion* (Prentice Hall, New York, 1996)

Kelly, J. J., Meerakker, J. E. A. M. v. d., Notten, P. H. L. and R. P. Tijburg, *Philips. Tech. Rev.*, 44, 61 (1988)

Laflere, W. H., F. Cardon and W. P. Gomes, Surf. Sci., 44, 541 (1974)

Laflere, W. H., Meirhaeghe, R. L. V., F. Cardon and W. P. Gomes, J. Phys. D: Appl. Phys., 13, 2135 (1980)

Laflere, W. H., R. L. V. Meirhaighe and F. Cardon Surf. Sci, 59, 401 (1976)

Landgren, G., R. Ludeke, Y. Jugnet, J. F. Morar and F. J. Himpsel, J. Vac. Sci. Technol. B, 2, 351 (1984)

Lenczycki, C. T. and V. A. Burrows, Thin Solid Films, 193, 610 (1990)

Li, J. and L. M. Peter, J. Electroanal. Chem., 199, 1 (1986)

Li, X. and P. W. Bohn, J. Electroanal. Chem., 147, 1740 (2000)

Lingier, S. and W. P. Gomes, Ber. Bunsenges. Phys. Chem., 95, 170 (1991)

Lockwood, D. J., P. Schmuki, H. J. Labbe and J. W. Fraser, Physica E4, 102 (1999)

Lum, R. M., A. M. Glass, F. W. Ostermayer, P. A. Kohl, A. A. Ballman, and R. A. Logan, J. Appl. Phys., 57, 39 (1985)

Mansfeld, F. and J. V. Kenkel, Corrosion, 31, 298 (1975)

Matz, R. and J. Zirrgiebel, J. Appl. Phys., 64, 3402 (1988)

Mayer, J. W., Electronic Materials Science: For Integrated Circuits in Si and GaAs (Macmillan Publishing Company, 1990)

Memming, R., Philips Res. Repts, 19, 323 (1964)

Morrison, S. R., *Electrochemistry at Semiconductor and Oxidized Metal Electrodes* (Plenum Press, New York and London, 1980)

Navon, D. H., *Electronic Materials and Devices* (Houghton Mifflin Company, Boston, 1975)

Osgood, R. M., A. Sanchez-Rubio, D. J. Ehrlich, and V. Daneu, *Appl. Phys. Lett.*, 40, 391 (1982)

Oskam, G., A. Natarajan, P. C. Searson and F. M. Ross, *Appl. Surf. Sci.*, 119, 160 (1997)

Pettinger, B., H. R. Schoppel, T. Yokoyama and H. Gerischer. *Berichte der Bunsen Gesellschaft*, 78, 1024 (1974)

Pleskov, Yu. V. and Yu. Ya. Gurevich. *Semiconductor Photoelectrochemistry* (Consultants Bureau, New York and London, 1986)

Plieth, W. J., G. Pfuhl, A. Felske and W. Badawy, *Electrochimica Acta.*, 34, 1133 (1989)

Podlesnik, D. V., H. H. Gilgen, R. M. Osgood, and A. Sanchez, *Appl. Phys. Lett.*, 43, 1083 (1983)

Rajeshwar, K. and T. Marz, *J. Phys. Chem.*, 87, 2352 (1983)

Rebul, M. C., *Corrosion*, 35, 423 (1979)

Reichman, J., *Appl. Phys. Lett.*, 36, 575 (1980)

Schmuki, P., J. Fraser, C. M. Vitus, M. J. Graham and H. S. Isaacs. *J. Electrochem. Soc.*, 143, 3316 (1996)

Schmuki, P., J. Praser, C. M. Vitus, M. J. Graham and H. S. Isaacs, *Electrochemical Society Proceedings*, 95, 226 (1995)

Schmuki, P, G. I. Sproule, J. A. Bardwell, Z.H. Lu and M. J. Graham, *J. Appl. Phys.*, 79, 943 (1996)

Schmuki, P., L. E. Erickson, D. J. Kockwood, B. F. Mason, J. W. Fraser, G. Champion and H. J. Labbe, *J. Electrochem. Soc.*, 146, 735 (1999)

Schmuki, P., L. E. Erickson, G. Champion, B. F. Mason, J. W. Fraser, and C. Moessner, *Appl. Phys. Lett.*, 70, 1305 (1997)

Schmuki, P., R. Morach and H. Boehni. *Extended Abstracts of the 183rd Meeting of the Electrochemical Society* (The Electrochemical Society, 1993)

Scully, J.R. and H.P. Hack. *Corrosion* 84, 34 (1985)

Searson, P. C., J. M. Macaulay, and S. M. Prokes, *J. Electrochem. Soc.*, 139, 3373 (1992)

Sixt, G., K. H. Ziegler and W. R. Fahrner *Thin Solid Films*, 56, 107 (1979)

Soltz, D. and L. Cescato, *J. Electrochem. Soc.*, 143, 2815 (1996)

Spicer, W. W., I. Lindau, P. Pianetta, P. W. Chye and C. M. Garner, *Thin Solid Films*, 56, 1 (1979)

Steer, C. A., G. S. Weng, J. L. Luo and D. G. Ivey, *Electrochemistry Communications*, 2, 754 (2000)

Takahashi, K., *Jap. J. Appl. Phys.*, 18, 1741 (1979)

- Tromans, D., G. G. Liu and F. Weinberg, *Corrosion Science*, 35, 117 (1993)
- Tyagay, V. A., V. A. Sterligov, and G. Ya. Kolbasov, *Electrochim. Acta*, 22, 819 (1977)
- Uhnerfeld, F. K., *J. Electrochem. Soc.*, 119, 1063 (1972)
- Ven, J. v. d., J. J. Kelly, *J. Electrochem. Soc.*, 148, G10 (2001)
- Wang, S., *Fundamentals of Semiconductor Theory and Device Physics* (Prentice Hall, Englewood Cliffs, New Jersey, 1989)
- Weimann, G., *Thin Solid Films*, 56, 173 (1979)
- Wicks, C. E. and F. E. Block, *Bulletin 605, Bureau of Mines. U.S. Government Printing Office, D. C. Washington*, 15 (1963)
- Wilmsen, C. W., *Thin Solid Films*, 39, 105 (1976)
- Wilmsen, C. W. and R. Kee, *Thin Solid Films*, 51, 93 (1978)
- Wilmsen, C. W., R. Kee and K. M. Geib, *J. Vac. Sci. Technol.*, 16, 1434 (1979)
- Yu, P. Y., Manuel Cardona, *Fundamentals of Semiconductors* (Springer, Germany, 1999)